7-1-2014

Thermal histories of CB meteorites: Constraints from compositions and microstructures of sulfides

Poorna Srinivasan

Poorna Srinivasan
Candidate

Earth and Planetary Sciences
Department

This thesis is approved, and it is acceptable in quality and form for publication:

Approved by the Thesis Committee:

Dr. Rhian Jones, Chairperson

Dr. Adrian Brearley

Dr. Francis McCubbin

Dr. Charles Shearer

THERMAL HISTORIES OF CB METEORITES: CONSTRAINTS FROM COMPOSITIONS AND MICROSTRUCTURES OF SULFIDES

BY

POORNA SRINIVASAN

BACHELOR OF SCIENCE, GEOLOGICAL SCIENCES,
RUTGERS UNIVERSITY, 2012

THESIS

Submitted in Partial Fulfillment of the
Requirements for the Degree of

Master of Science
Earth and Planetary Sciences

The University of New Mexico
Albuquerque, New Mexico

July 2014

ACKNOWLEDGEMENTS

I would first and foremost like to thank my advisor, Dr. Rhian Jones, for all the support, motivation, and funding given during the duration of my study. I am extremely grateful for the countless hours she spent preparing me and guiding me to succeed in this field. I would also like to thank Dr. Adrian Brearley for not only his help with lab work, but for his guidance and assistance with this project and in graduate school. I am greatly appreciative to all the support and direction my committee members, Dr. Francis McCubbin and Dr. Charles Shearer, gave me during my master's. Lastly, I would like to thank Mike Spilde and Elena Dobrica for all their time and patience during EPMA and SEM training.

THERMAL HISTORIES OF CB METEORITES: CONSTRAINTS FROM COMPOSITIONS AND MICROSTRUCTURES OF SULFIDES

by

POORNA SRINIVASAN

B.S., Geological Sciences, Rutgers University, 2012

M.S., Earth and Planetary Sciences, University of New Mexico, 2014

ABSTRACT

CBs are metal-rich carbonaceous chondrites, and are subdivided into type CBa and CBb, which are primarily distinguished by the size of particles. Although CBs are classified as chondrites, the high abundance of metal (>40%) make them a distinct group of meteorites. The origin of CBs is highly debated, but these meteorites are thought to have formed in an impact-generated vapor plume 4.563 Ga ago [Amelin et al., 2005; Krot et al., 2005], rather than in the solar nebula.

This study focuses on textures and compositions of homogeneous and exsolved sulfides in metal grains in CB meteorites to constrain secondary thermal histories. We use SEM, EPMA, FIB, and TEM techniques to examine metal and sulfides, and quantify modal abundances of metal particles and sulfide inclusions using high-resolution BSE images with ImageJ software. CB metal (Fe,Ni) particles contain different types of sulfide inclusions, which we categorize as: homogeneous low-Cr sulfide inclusions composed of MSS_1, exsolved sulfide inclusions of MSS_1 with high-Cr daubreelite, sulfide inclusions with Fe,Ni metal blebs, and arcuate sulfides. Some particles also contain Fe-

Ni-S eutectic textures composed of a mixture of MSS_1 and Fe,Ni metal. The four CB meteorites analyzed (CBa Gujba, CBa Weatherford, CBb HH 237, and CBb QUE 94411) all contain these sulfides within metal grains. Sulfide inclusions possibly formed as a result of precipitation of excess S from solid metal at low temperatures. The CB parent body was likely affected by late impacts, causing heterogeneous heating of surface material. This work provides evidence of heterogeneous reheating by impacts. Examination of exsolved sulfides shows that they record maximum reheating temperatures of <<600°C, and Fe-Ni-S eutectic textures show reheating temperatures of >950°C. Observations of fine-grained textures and small size of particles indicates reheating must have been followed by very rapid cooling. Plastic deformation is also observed in some metal grains and lamellae of exsolved sulfide inclusions, indicating deformation post-dates formation of inclusions. Our study shows that CBa and CBb meteorites not only formed in a similar environment, but they also experienced similar secondary processing.

Table of Contents

List of Figures

List of Tables

1. Introduction

1.1 Early Solar System Material: An Introduction to Chondrite Formation

The Solar System formed about 4.6 billion years ago in a turbulent molecular cloud, later leading to the origin of meteorite parent bodies. One leading hypothesis for solar system formation is that interstellar dust and gas in a molecular cloud was affected by a shockwave from a nearby supernova, causing the cloud to collapse [Boss, 2008]. The collapse of the molecular cloud either caused the development of a protoplanetary disk with a protosun materializing in the center [Lada and Lada, 2003; Adams, 2010], or conversely, the development of a protosun with a disk forming around it [Grossman and Larimer, 1974]. Dust particles and gas were then able to condense within the disk, accrete into large bodies, and later become asteroids and planets [Dauphas and Chaussidon, 2011].

Chondrites are undifferentiated meteorites composed of a mixture of the oldest solids in the Solar System. They are comprised of sub-millimeter chondrules (once-molten olivine and pyroxene-rich particles), refractory inclusions (nebular condensates that are primarily crystalline silicates and oxides high in Ca, Al, and Ti), metal and sulfide grains (mainly Fe,Ni and FeS), and fine-grained matrix (sub-micrometer silicate, metal, and sulfide material filling in the interstices between chondrules and refractory inclusions). These components carry thermal, chemical, and isotopic records of conditions in the early solar system [Scott and Krot, 2003; MacPherson, 2003; Campbell et al., 2005]. Chondrites are subdivided into “ordinary”, “enstatite”, and “carbonaceous” classes; with a few chondrites being ungrouped (Table 1). These divisions can be distinguished by their oxygen isotope ratios ($\delta^{17}O/\delta^{18}O$) (Figure 1a).

Group	Type	Refractory inclusions (vol. %)	Chond. (vol.%)[a]	Chond. ave. diam. (mm)	Fe,Ni metal (vol. %)	Matrix (vol.%)[b]	Fall freq.[c] (%)	Refract. lith./Mg rel. CI[d]	Examples
Carbonaceous									
CI	1	<0.01	<5	–	<0.01	95	0.5	1.00	Ivuna, Orgueil
CM	1–2	5	20	0.3	0.1	70	1.6	1.15	Murchison
CO	3	13	40	0.15	1–5	30	0.5	1.13	Ornans
CV	2–3	10	45	1.0	0–5	40	0.6	1.35	Vigarano, Allende
CK	3–6	4	15	0.8	<0.01	75	0.2	1.21	Karoonda
CR	1–2	0.5	50–60	0.7	5–8	30–50	0.3	1.03	Renazzo
CH	3	0.1	~70	0.05	20	5	0	1.00	ALH 85085
CB_a	3	<0.1	40	~5	60	<5	0	1.0	Bencubbin
CB_b	3	<0.1	30	~0.5	70	<5	0	1.4	QUE 94411
Ordinary									
H	3–6	0.01–0.2	60–80	0.3	8	10–15	34.4	0.93	Dhajala
L	3–6	<0.1	60–80	0.5	3	10–15	38.1	0.94	Khohar
LL	3–6	<0.1	60–80	0.6	1.5	10–15	7.8	0.90	Semarkona
Enstatite									
EH	3–6	<0.1	60–80	0.2	8	<0.1–10	0.9	0.87	Qingzhen, Abee
EL	3–6	<0.1	60–80	0.6	15	<0.1–10	0.8	0.83	Hvittis
Other									
K	3	<0.1	20–30	0.6	6–9	70	0.1	0.9	Kakangari
R	3–6	<0.1	>40	0.4	<0.1	35	0.1	0.95	Rumuruti

Table 1. The 15 chondrite groups and their properties. The CR clan consists of CR, CH, and CB chondrites. CB chondrites are subdivided into CBa and CBb groups. CB meteorites have a greater abundance of metal than any other chondrite group. Diagram obtained from Scott (2007).

Ordinary chondrites plot above the terrestrial fractionation line (TFL). Enstatite chondrites plot on the TFL. With the exception of the CI chondrites, carbonaceous chondrites lie below the TFL, and the majority of them lie on or close to the carbonaceous chondrite anhydrous mineral (CCAM) line [Clayton, 2003].

Different components in chondrites formed under diverse conditions. Refractory inclusions, specifically calcium-aluminum-rich inclusions (CAIs), have the oldest Pb-Pb ages of 4567.2 ± 0.6 Ma [Amelin et al., 2002], and likely formed close to the inner edge of the protoplanetary disk, <0.1 AU from the protosun [Shu et al., 1996]. Chondrules, which formed 1-3 Myr after CAI formation [Kita et al., 2005; Amelin et al., 2004], and matrix material, formed further from the protosun, <10 AU. These chondritic components mixed and accreted together close to the nebula midplane to form asteroids [Desch, 2006;

Scott, 2007]. Chondrites hold the key to understanding conditions in the early solar system, and it is important to understand how these early solids formed.

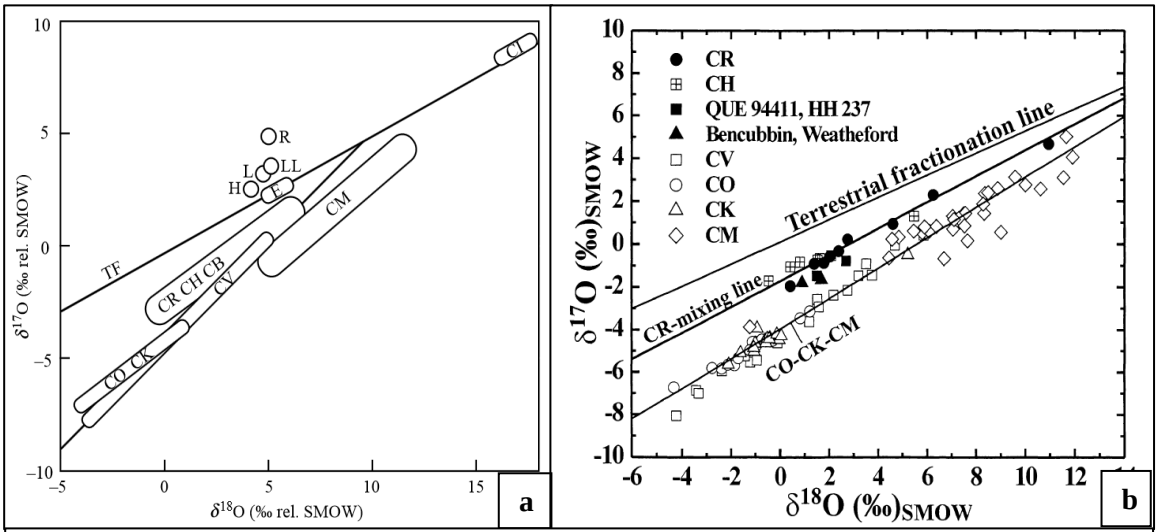

Figure 1. Oxygen isotope plots ($\delta^{17}O/\delta^{18}O$). [a] Bulk oxygen isotope compositions of chondritic meteorite groups. TF is the terrestrial fractionation line. CV material forms the carbonaceous chondrite anhydrous minerals (CCAM) line, and the CR-CH-CB grouping forms the CR mixing line. Diagram obtained from Clayton (2003). [b] Bulk oxygen isotope compositions, specifically showing data for the CR, CH, CBa (Bencubbin and Weatherford) and CBb meteorites (QUE 94411, HH 237). Diagram obtained from Krot et al. (2002).

1.2 The CR Clan

The CR clan consists of CR, CH, and CB chondrites. Meteorites in this clan are related by similarities in oxygen isotope ratios, and unlike the other carbonaceous chondrites that lie along the CCAM line, these three groups lie along the "CR mixing line" (Figure 1b). Members of the CR clan lie below the TFL and above the CCAM line. The CR clan is further differentiated from the other carbonaceous chondrites by high volumes of metal. Carbonaceous chondrites typically have between 0.01-5 vol.% Fe,Ni metal, whereas meteorites in the CR clan have between 5-70 vol.% metal (Table 1) [Weisberg et al., 2001; Krot et al., 2002; Scott, 2007]. The CR clan also has an enrichment of the heavy nitrogen isotope, ^{15}N. Most chondritic groups have $\delta^{15}N$ ((^{15}Nsample - ^{15}Nstandard) / ^{15}Nstandard * 1000) values of ≤90‰ [Grady and Pillinger,

1990], whereas the CR clan have $\delta^{15}N$ values between 200‰ to 1500‰. This ^{15}N enrichment appears to be located in the rims around sulfide blebs, within some of the sulfides, within a carbon phase in the metal, in impact-melt regions, and in rare lithic clasts [Prombo and Clayton, 1978; Franchi et al., 1986; Keeling and Marti, 1987; Sugiura et al., 1999, 2000; Weisberg, 2001; Bonal et al., 2010].

CH and CB chondrites are closely related, and possibly share similar parent bodies and thermal histories. These two groups are the most metal-rich carbonaceous chondrites, with CH containing ~20 vol.% metal, and CB containing 60-70 vol.% metal. Some metal particles in CH and CB meteorites contain zoned and unzoned metal grains [Weisberg et al., 1995; Krot et al., 2002; Goldstein et al., 2007]. Isheyevo, which is classified as a CB/CH meteorite, shows how closely related these two groups are chemically and isotopically. Isheyevo contains several lithologies (metal-poor and metal-rich) with 7-70 vol.% metal particles and 90-30 vol.% chondrules. It also contains CAIs that are mineralogically similar to those in CHs, and oxygen isotope compositions lies along the CR-CH-CB trend [Ivanova et al., 2008; Krot et al., 2010; Bonal et al., 2010]. The most prominent idea for formation of metal in CH and CB chondrites is condensation from a vapor in heating events produced from impacts on the parent body [Wasson and Kallemeyn, 1990; Rubin et al., 2003; Goldstein et al., 2011]. Goldstein et al. (2007) provide evidence that zoned and unzoned particles in CHs formed in a condensation process on a timescale of a couple of days, and some were later heated to 800-1000°C, likely by impacts on the parent body. CHs were possibly heated to a higher temperature or to longer durations than the CBs; however, the processes that affected some of the particles likely the same [Goldstein et al., 2007].

1.3 Classification of CB Meteorites

Meteorites in the CB chondrite group are classified as carbonaceous (C) and similar to the main chondrite for this group, Bencubbin (B). These meteorites are considered carbonaceous chondrites because their mean refractory-lithophile/Mg abundance ratios ≥ 1 relative to CI chondrites, and their oxygen-isotopic compositions fall below the terrestrial fractionation line [Krot et al., 2002]. Ordinary and enstatite chondrites have mean refractory-lithophile/Mg abundance ratios of < 1 relative to CI, and oxygen-isotope compositions that lie above or on the terrestrial fractionation line (Table 1) [Clayton, 1993; Clayton and Mayeda, 1999; Weisberg et al., 1993; 1995; 2001; Scott, 2007]. CBs are classified as "petrologic type 3", meaning that these chondrites are near-pristine samples and have not been greatly changed by metamorphic or hydrous alteration processes since they accreted. Petrologic types 1-2 have undergone aqueous alteration, and types 4-6 represent increasing degrees of thermal metamorphism on the parent body after accretion. Petrologic type 3 actually represents a wide range of alteration conditions. For ordinary and some groups of carbonaceous chondrites, type 3 is further divided into subtypes 3.0 to 3.9. Subtypes closer to type 4 have experienced thermal metamorphism up to ~600 °C [Huss et al., 2006; Van Schmus and Wood, 1967; Brearley and Jones, 1998; Scott and Krot, 2003]. Classification of CB chondrites as type 3 is based on the presence of clear, isotropic glass within chondrules [Weisberg et al., 2001].

Although CBs are similar to carbonaceous chondrites in whole-rock chemistry and isotopic compositions, there are several characteristics that make these meteorites a distinct member of the carbonaceous chondrite class. CBs have a high abundance of Fe,Ni metal, low abundance of matrix, low carbon content, and a high depletion in

moderately volatile lithophile elements [Weisberg et al., 1990; Krot et al., 2002; Scott, 2007]. Table 1 shows a comparison of characteristics in all the chondrite groups. Matrix in CBs, which is mainly composed of silicate glass and immiscible blebs of Fe,Ni metal, is impact melt. These meteorites are also reduced, with average olivine compositions between ~2.3-4.1 mol.% [Weisberg et al., 2001]. Enstatite chondrites provide evidence of the most reduced environment of all chondritic groups; comparatively, CBs show conditions less reduced than E chondrite values [Scott and Krot, 2005].

There are two types of CB chondrites: CBa and CBb. The main discriminator between the two types is the size of individual components. CBa meteorites have about 60 vol.% Fe,Ni metal, with nickel content ranging from 5-8 wt.%, and large, mm-cm-sized chondrules and metal particles (Figures 2a,b). CBb meteorites have a slightly greater amount of Fe,Ni metal, ~70 vol.%, with nickel content ranging from 4-15 wt.%, chemically zoned metal particles, and smaller, μm-mm-sized chondrules and metal particles [Weisberg et al., 1990; 2001; Krot et al., 2002] (Figures 2c,d).

1.4 Formation of CB Meteorites

The origin of CB meteorites is highly debated. Although these meteorites are classified as chondrites, the abundance and composition of metal and silicate components is unusual compared to other carbonaceous chondrites. CBs were previously thought to have condensed in the solar nebula, similar to the other chondrite groups [Newsom and Drake, 1979; Meibom et al., 2000; Petaev et al., 2001; Weisberg et al., 2001; Krot et al., 2002; Campbell et al., 2005b]. However, many studies dispute a nebular formation for these meteorites; a more prominent idea is post-nebula condensation in an impact-

generated vapor plume [Wasson and Kallemeyn, 1990; Campbell et al., 2002; Rubin et al., 2003; Goldstein et al., 2011].

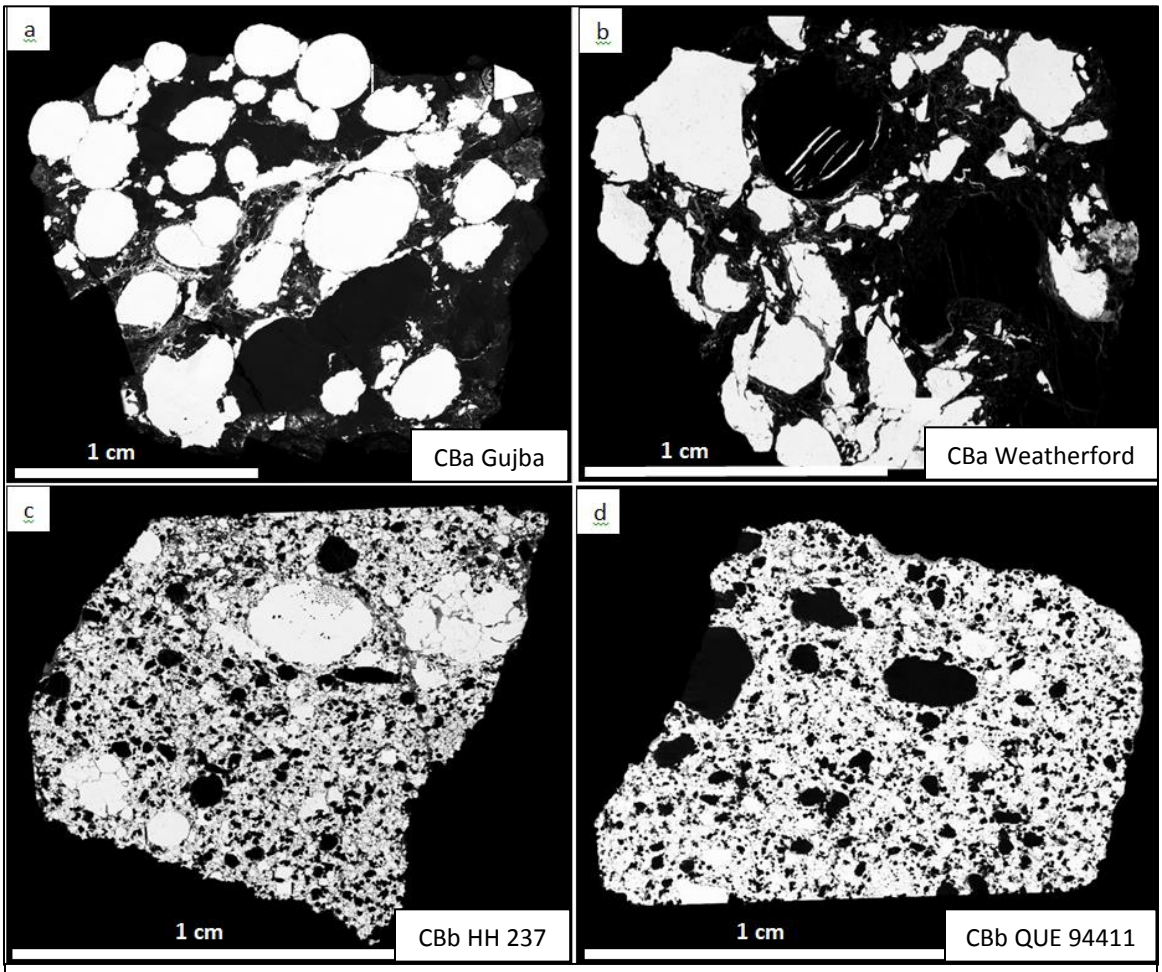

Figure 2. Backscattered electron images of four CB meteorite samples. Metal grains and particles are white, chondrules are black, and matrix (impact melt) is dark grey/black interstitial to the metal and silicate material. [a] CBa Gujba contains mostly large mm-to-cm-sized metal particles that are circular to ellipsoidal in shape. [b] CBa Weatherford contains mostly mm-to-cm-sized metal particles that are highly deformed; metal is elongated and irregular in shape. [c] CBb HH 237 contains mostly µm-to-mm-sized metal particles, with a few metal particles that are comparable in size to Gujba and Weatherford. [d] CBb QUE 94411 contains mostly µm-to-mm-sized metal particles, and unlike the other CBs, it does not contain any large metal particles.

The solar nebular model suggests that CBs are very primitive meteorites, forming when the protoplanetary disk was still present in the early Solar System. The strongest evidence for nebular formation comes from metal grains. Unzoned metal in CBa and CBb shows approximately solar Co/Ni ratios, which indicates a primitive nebular signature

[Weisberg et al., 2001; Krot et al., 2002]. CBb meteorites have zoned metal grains, indicating formation at high temperatures in a rapidly cooling nebular gas [Meibom et al., 2000; Petaev et al., 2001; Weisberg et al., 2001; Campbell et al., 2005b]. There are quite a few problems with CB formation in the solar nebula, and these have led to development of the vapor plume model.

The vapor plume model argues for formation after the solar nebula dissipated, and suggests that CBs formed from a collision between two bodies that created a dense vapor plume. This model requires one body to be silicate-rich and the other body to be metal-rich, for the plume to be dense enough to condense both silicate and metal particles. (Evidence for early metal-rich bodies comes from magmatic iron meteorites, which shows core formation could have occurred <1 Myr after the formation of CAIs [Klein et al., 2009]). Metal and chondrules could possibly form as condensates in the vapor plume or as melt droplets from the collision [Kallemeyn et al., 2001]. CBs contain 60-70 vol.% metal, and this high volume is hard to explain in terms of condensation from the canonical solar nebula pressure ($P_{H2} \sim 10^{-3}$ to 10^{-6} bar) and composition. Equilibrium condensation models show that the high abundance of metal can only be explained if condensation occurred from a highly metal-enriched gas, and siderophile elements were enriched by a factor of $\sim 10^{7}$ relative to solar nebular gas. The cores of zoned metal grains in CBb meteorites show an enrichment in refractory platinum group elements (PGE), which indicates a volatility-controlled process, however; the abundance is not consistent with condensation directly from the solar nebula. The Pd/Ni ratio in metal grains is significantly higher than expected from calculated nebular condensation trends, which

indicates a non-nebular origin for metal [Wasson and Kallemeyn, 1990; Campbell et al., 2000; 2002; 2005; Krot et al., 2002; Petaev, 2006].

Formation ages of this impact plume event are obtained from chondrules in CBs. U-Pb ages for chondrules in CBa Gujba are 4562.7 ± 0.5 Ma [Amelin et al., 2002; Krot et al., 2004]. This CB chondrule formation age is about 5 million years after formation of CAIs in CV chondrites, which have the oldest Pb-Pb ages of any planetary material at 4567.2 ± 0.6 Ma [Amelin et al., 2002]. Chondrules in CV and CR chondrites, which are thought to have formed in the solar nebula, show older ages than CBs and have Pb-Pb ages of 4566.7 ± 1.0 Ma and 4564.7 ± 0.6 Ma, respectively [Amelin et al., 2002]. Given the relatively young ages of CB chondrules, formation possibly postdates the lifetime of the solar nebula [Amelin and Krot, 2005; Krot et al., 2005], supporting the impact plume model. However, it is possible that the solar nebula might have still existed during the time CBs were forming. Calculations of the lifetimes of protoplanetary disks of low-mass stars give lifetimes above 3 Myr, with the oldest being about 6 Myr [Haisch et al., 2001].

1.5 Later Impacts on the CB Parent Body

CB meteorites contain some chondrules and impact-melt glass with even younger ages. Some chondrules in CBa Gujba have U-Pb ages of 4545.4 ± 3.9 Ma [Krot et al., 2004], which is ~17 Myr younger than other chondrules found in this meteorite. This difference provides evidence of a resetting event after the first formation of chondrule components. CB matrix consists of impact melt, which occurs interstitial to the large metal particles and chondrules. Impact-melt glasses from CBa meteorites show even younger ages than coexisting chondrules. Impact melt from CBa Weatherford gives Ar-Ar ages of 3.6 Ga [Kelly and Turner, 1987]. Glass from CBa Bencubbin gives Ar-Ar ages

of 4.20 ± 0.05 Ga [Marty et al., 2010].

Late impact events would cause chemical and textural changes in material on the surface of the CB parent body. Impact events may have caused a change in abundance of volatile elements brought in from the impactor. CBs show enrichment in ^{15}N, which could be explained if the impactor had a primitive, isotopically unequilibrated, nitrogen component [Marty et al., 2010]. Impacts on the parent body would also cause heterogeneous heating on the surface, disturbing existing mineral assemblages. Plastic deformation of chondrules, high-pressure minerals, multiphase metal particles, and Fe-Ni-S eutectic textures provide evidence of these later impacts [Goldstein et al., 2011; Weisberg, et al., 2001; 2004 2010; Chappell et al., 2011]. Impact melt regions are most likely not showing ages of original formation of the parent body, but of later heating episodes after parent body accretion.

1.6 Compositions of Metal Particles in CBs

Metal is the most abundant component of CB meteorites, differing between type CBa and CBb in particle size, abundance, and composition. CBa meteorites mainly consist of mm-cm-sized homogeneous (unzoned) metal particles (Figures 2a,b), and CBb meteorites consist of μm-mm-sized unzoned and zoned metal particles (Figures 2c,d). Previous studies on CBs show that compositions of Fe,Ni metal vary from grain to grain. Metal in CBs is kamacite (Fe,Ni). Nickel contents of metal in CBa meteorites are between 4.8-8.2%, compared with 4.1-14.8% in CBb meteorites, with higher Ni contents in zoned grains [Weisberg et al., 1990; 2001]. Cobalt, phosphorus, and chromium are also present in low abundances in the metal, <1 wt.%. The Co/Ni ratio for unzoned metal grains follows the solar ratio, but at high Ni values in the zoned metal grains, the ratio

diverges from solar values [Weisberg et al., 2001]. Platinum group elements (PGEs) in CBa meteorites are present at ~1 x CI levels, and approximately chondritic relative abundances. PGEs are also positively correlated with Ni [Campbell et al., 2002]. Moderately volatile siderophile elements, such as Cu, Ga, Ge, As, and Sn, are depleted by factors of 10-1000, relative to CI chondrites [Campbell et al., 2002; Krot et al., 2002]. Zoned metal grains in CBb meteorites show compositional zonation from core to rim. Ni and Co decrease towards the rim, and Fe and Cr increase towards the rim [Weisberg et al., 2001]. PGEs in zoned metal of CBb meteorites have higher concentrations in the center of grains, ~2.5-4 x CI, and taper off to ~1 x CI towards the edges. Moderately volatile siderophile elements, such as Cu, Ge, As, and Sn are depleted in the cores compared to the edges of grains [Krot et al., 2002].

1.7 Sulfides in CBs

Some unzoned metal grains in CBs contain sulfides, and the composition and textures of these sulfides are important in understanding the origin of metal in CBs. Sulfides in CBs have been identified as troilite (FeS), which is a common sulfide mineral in all classes of meteorites [Lodders & Fegley, 1998; Weisberg et al., 2006]. Sulfides in CBs occur either as arcuate textures along metal grain boundaries, or as inclusions throughout the metal grains [Newsom and Drake, 1979; Weisberg et al., 2001; Krot et al., 2002; Rubin et al., 2003; Campbell et al., 2005b].

Sulfides found in metal particles are hard to explain through either the nebular condensation model or the vapor plume model. One explanation for formation of sulfide inclusions is that sulfur was incorporated into metal at high temperatures when metal was molten, later precipitating at lower temperatures [Rubin et al., 2003; Campbell et al.,

2005b]. CB metal contains a significant amount of sulfide inclusions, which means there must have been a significant abundance of sulfur dissolved in the metal. Troilite is not stable at high temperatures under nebular conditions, so all that sulfur would have to remain dissolved in the metal phase until the system cooled enough. Calculated condensation of sulfides from a gas of solar composition begins at ~700 K [Grossman, 1972; Lauretta et al., 1996]. However, Campbell et al. (2005b) estimated much higher condensation temperatures of ~1100 K for metal, by examining volatile siderophile elements in metal particles in CBs. As we discuss below, sulfide-bearing metal particles are likely to have formed from a melt. However, the eutectic temperature in the Fe-FeS system is 1261 K, far above the ~710 K condensation temperature for sulfur in the solar nebula [Lauretta et al., 2001]. Therefore, if metal-sulfide particles were once partially molten in the nebula, all the sulfur that was present would have rapidly devolatilized to the surrounding gas [Campbell et al., 2005b]. Another possibility for sulfide formation is that metal particles were porous initially and reacted with surrounding H_2S gas at lower temperatures to form troilite [Weisberg et al., 2001; 2009]. However, studies on primitive ordinary chondrites show that this process would have resulted in an outer shell of sulfide around an inner shell of slightly different composition [Lauretta et al., 1996]. Neither of these compositions are seen in CB meteorites [Campbell et al., 2005b]. A third explanation is that if metal grains formed in an impact-generated vapor plume, condensates could have been liquid that was S-rich in composition [Rubin et al., 2003]. As kamacite began crystallizing from the melt, the residual melt became enriched in sulfur. At low temperatures, sulfides could crystallize around metal grain boundaries, and sulfide inclusions could later precipitate from excess sulfur dissolved in the metal.

Some sulfide inclusions in the metal of CBs are chromium-rich, and these can be an important tracer for thermal histories. The mineral daubreelite ($FeCr_2S_4$) is a Cr-rich sulfide that has been described a handful of times in the meteorite literature, mostly in enstatite chondrites and iron meteorites [Keil, 1968; El Goresy and Kullerud, 1969; Bevan et al., 1981; Chikami et al., 1998; Lin and El Goresy, 2002]. Daubreelite has also been described in CB meteorites, but due to its small size and low abundance, it has not been well characterized or explained thoroughly [Petaev et al., 2001; Weisberg et al., 2001]. At high temperatures (>1060°C) daubreelite is hexagonal, and below 1060°C, it inverts to a cubic crystallographic structure [Lundqvist, 1943; El Goresy and Kullerud, 1969]. This mineral can be used to constrain thermal episodes on the CB parent body since it can only coexist with troilite (low Cr sulfide) at certain temperature ranges.

1.8 The Fe-Cr-S System

Experiments with Cr, Fe, and S have been conducted previously to constrain the stability fields and equilibrium relationships of various minerals in this three-component system [El Goresy and Kullerud, 1969]. At 700°C, daubreelite is stable with four sulfides: low Cr monosulfide solid solution 1 (MSS_1: $(Fe,Cr)_{1-x}S$), high Cr monosulfide solid solution II (MSS_2: $(Cr,Fe)_{1-x}S$), $(Fe,Cr)S_2$, and $Cr_{2.1}S_3$ (Figure 3a). At 700°C, tie lines exist between MSS_1 and MSS_2, and daubreelite cannot coexist with Fe metal. Lowering the temperature to 600°C changes the stable assemblages, and MSS_1 and MSS_2 can no longer coexist (Figure 3b). The maximum Cr content of the MSS_1 solid solution field decreases. Daubreelite is stable in a three-phase assemblage with MSS_1 and Fe,Cr metal, as well as with MSS_2 and Fe,Cr metal. In Figure 3, stoichiometric troilite is indicated on each diagram on the FeS join. It is possible that at temperatures much lower

than 600°C daubreelite can coexist with troilite, since most studies on chromium-rich sulfides in meteorites show that daubreelite occurs with troilite, FeS [Bevan et al., 1981; Chikami et al., 1998; Weisberg et al., 2001; Lin and El Goresy, 2002]. Therefore, the three-phase assemblage of troilite-daubreelite-Fe metal could be stable at very low temperatures. Assemblages of coexisting sulfide phases in CB meteorites can be used to interpret temperatures of thermal episodes on the CB parent body.

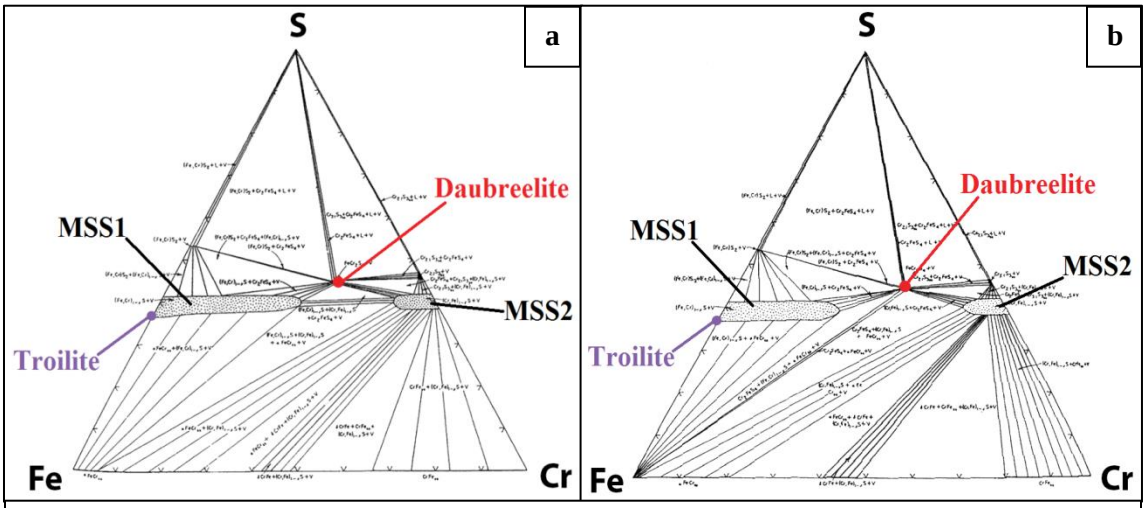

Figure 3. Equilibrium phase diagrams for the Fe-Cr-S system from El Goresy and Kullerud (1969), given in weight percent. [a] At 700°C. [b] At 600°C.

1.9 Exsolution in Sulfides

Some sulfide inclusions in CBa and CBb metal contain fine lamellae of the chromium-rich phase, daubreelite. This texture has been interpreted as being the result of exsolution [Weisberg et al., 2000; 2001; Rubin et al., 2003]. Exsolution in sulfides can result from cooling as well as from reheating episodes. This texture occurs when unmixing of a solid solution produces intergrowths of two stable phases. Exsolution lamellae are typically parallel to each other. The orientation of the lamellae is controlled by the host phase; lamellae crystallographically align with the structure of the host phase to reduce stress and minimize the interfacial energy between the two phases. On the

600°C Fe-Cr-S diagram (Figure 3b), the tie lines existing between daubreelite and MSS_1 show daubreelite can exsolve from low Cr MSS_1.

Shock reheating can disturb mineral assemblages after the original formation of a parent body. Previous studies of chromium-rich sulfides have made the interpretation that grains with homogeneous chromium content point to a nebular process for formation of metal grains, while the exsolution features must have occurred because of diffusion from mild impact heating on the parent body after accretion [Weisberg et al., 2001; Lin & El Goresy, 2002]. Textural changes from reheating events can be attributed to the fast kinetics of metal-sulfide reactions [Tomkins, 2009].

In this study, we have obtained both quantitative and qualitative data from four different CB meteorites. We have carried out a detailed study of textures and compositions of homogeneous and exsolved sulfides in metal grains of CBa and CBb meteorites, which have been poorly discussed in the literature. Using Fe-Cr-S ternary diagrams, we have obtained quantitative constraints on the temperatures experienced during impact heating on the CB parent body. We discuss the formation of sulfides and the implications of the presence of these sulfides for the origin of CB meteorites.

2. Methods

2.1 Samples

Six polished sections of CB meteorites were used for this study: four CBa sections and 2 CBb sections. We analyzed three sections of CBa Gujba: 1) a polished 1.8 x 2.1 cm thick slice of UNM-Cr34.2, 2) a 2.5 x 1.5 cm thin section in a 5 cm epoxide mount loaned from Bruker-Nano, courtesy J. Berlin, and 3) a 2.5 x 4 cm thin section

labeled Gujba 7-0, set in a 5 cm epoxide mount, loaned from J. Goldstein (University of Massachusetts). For CBa Weatherford we analyzed a 1.5 x 2 cm thin section, UNM-259. We analyzed two sections of CBb meteorites. CBb QUE 94411.8 is a 1 x 1.5 cm section in a 1 inch epoxide mount loaned from the Smithsonian Institution, and CBb HH 237 is a 1 x 1.2 cm section in a 1 inch epoxide mount loaned from J. Goldstein (University of Massachusetts). Samples were carbon coated prior to micro-analysis. Sections were documented using scanning electron microscope (SEM) techniques, and analyzed using electron microprobe (EPMA) and transmission electron microscope (TEM) techniques at the University of New Mexico.

2.2 Quantitative Techniques

The scanning electron microscope (SEM) was used to examine textures and identify sulfide inclusions in the metal grains. We used a JEOL 5800LV SEM to acquire backscattered electron (BSE) images with a 20 kV accelerating voltage and 1 nA beam current. We also used a FEI Quanta 3D FEG SEM, equipped with an EDAX silicon drift (SD) energy dispersive X-ray spectrometer (EDS) and a focused ion beam (FIB). The accelerating voltage was set at 30 kV and the beam current was 32 nA. We obtained high-resolution BSE images, and from these created BSE mosaics for Gujba (section UNM Cr34.2), Weatherford, QUE 94411, and HH 237. We then used ImageJ [Schneider et al., 2012] to determine abundances of metal grains and sulfide inclusions from the four mosaics.

The JEOL 8200 electron microprobe (EPMA), equipped with five wavelength-dispersive X-ray spectrometers (WDS) and an energy-dispersive X-ray spectrometer

(EDS), was used for quantitative mineral analyses. Silicon, P, S, V, Cr, Mn, Fe, Co, Ni, Cu, and Zn were measured by WDS in sulfide inclusions and metal grains. Standards used were Si metal, apatite (Wilberforce), pyrite, V metal, Cr metal, spessartine, Fe metal, Co metal, Ni metal, chalcopyrite, and sphalerite, respectively. Wavelength scans conducted in the UNM EPMA laboratory show that there is a slight peak shift for P Kα between phosphide and phosphate (M. Spilde, personal communication). The P peak on our apatite standard is shifted to a lower value than one obtained with a gallium phosphide standard (difference of 0.089 mm). So we have a small error on P from measuring slightly fewer counts. Detection limits for Si, P, S, N, Co, Fe, Cr, Mn, and V were <0.02 wt.%, and for Cu and Zn were <0.09 wt.% for all metal and sulfides. Peak overlap corrections were implemented using Probe for Windows software, for Ni-Co, Co-Fe, Mn-Cr, and V-Cr, to account for peak interferences between the transition metal elements. Mineral compositions were determined using a 20 kV accelerating voltage, 20 nA beam current, and 1 μm spot size. Count times were 20 sec for Fe and Ni, 30 sec for Si, P, S, Co, Cr, and Mn, and 40 sec for Cu, Zn, and V. Line-array analyses were measured on selected exsolved sulfide inclusions. Combined WDS/EDS X-ray maps were obtained on sulfide inclusions and surrounding metal grains to identify elemental distributions in exsolved sulfides.

Sulfide 5 from CBa Gujba was selected as a representative sample of an exsolved sulfide inclusion and prepared for TEM analysis with focused ion beam (FIB) techniques with the FEI Quanta 3D FEG SEM/FIB instrument. A platinum protective layer (2 μm thickness) was deposited in a strip across the area of interest prior to FIB sample preparation to minimize ion beam damage. We cut a section of the inclusion ~20 μm in

length through FIB gallium ion milling, which was performed with an ion beam voltage of 30 kV and beam currents from 3 nA down to 10 pA. The sample was removed from the thin section by the *in situ* lift out technique using an Omniprobe 200 micromanipulator and was transferred to a Cu TEM half grid. Final ion milling to electron transparency was carried out with the samples attached to the TEM grid.

Transmission electron microscope (TEM) studies were performed using a JEOL JEM-2010 high-resolution TEM, equipped with an Oxford INCA EDS system and a Gatan Orius CCD imaging system, and a JEOL 2010F FASTEM TEM/STEM, equipped with a GATAN GIF 2000 imaging filtering system and Oxford INCA/ISIS EDS system, both operating at 200 kV. We obtained bright field and dark field STEM images to document the microstructures of the lamellae in the sulfide inclusion. Selected area electron diffraction (SAED) patterns (DP) were acquired to identify crystallographic orientations of the sulfide phases. Compositional data was obtained using the Oxford INCA X-ray analysis system using theoretical k-factors.

3. Results

3.1 Metal and Sulfide Textural Observations

CB meteorites are metal-rich and contain ~60-80 vol.% kamacite (Fe,Ni) grains. Individual kamacite grains are commonly grouped together to form larger metal particles [Weisberg et al., 2001; Krot et al., 2002]. The terminology for metal particles in CBs is unclear in the literature; common terms used for the same objects are: clasts [Newsom & Drake, 1979; Campbell et al., 2002], aggregates [Weisberg et al., 1990; Krot et al., 2002], fragments [Weisberg et al., 2001], metal chondrules [Weisberg et al., 2002], and globules [Rubin et al., 2003]. These terms imply processes such as accretion, breakup, or a

size/shape parameter that do not necessarily apply to all the CBs. For this study, we use the term “particles” to describe the groupings of individual kamacite grains because it does not imply any specific formation process. CBa meteorites mostly contain mm-to-cm-sized metal particles, with a low abundance of μm-to-mm-sized particles. In our ~2 cm-sized sample of Gujba (UNM-Cr34.2), there are 30+ clearly defined metal particles that are mainly ellipsoidal and circular in shape, and, with a few elongated exceptions, their edges are round and smooth (Figure 2a). In contrast, the ~2 cm sample of Weatherford contains ~30 metal particles that are mainly elongated and irregular in shape, and appear to be highly deformed; edges of the particles are irregular and the boundaries of individual particles are less well defined than those in Gujba (Figure 2b). CBb meteorites mostly contain μm-to-mm-sized metal particles. In addition, our ~1 cm sample of HH 237 contains ~5 large metal particles that are ellipsoidal in shape; however, unlike in Gujba, they appear cracked and have irregular outlines (Figure 2c). Our ~1.5 cm sample of QUE 94411 does not contain any cm-sized metal particles. All of the metal particles in QUE 94411 are μm-to-mm-sized and irregular in shape (Figure 2d). Metal particles in all four CB meteorites can be composed of homogeneous (unzoned) kamacite grains, homogeneous (unzoned) kamacite grains containing sulfide inclusions and/or silicate inclusions, or zoned kamacite grains, which are only present in CBb meteorites [Weisberg et al., 2001; Campbell et al., 2005b].

Some metal particles contain arcuate (‘bow-shaped’) sulfide textures [Rubin et al., 2003] along kamacite grain boundaries (Figure 4a). When present, these textures help define the borders of each grain. Arcuate sulfide textures are commonly found in CBa meteorites and are rare in CBb meteorites. Figure 4b shows possible arcuate textures in

CBb HH 237, however, these could also be sulfides situated along cracks in the metal particle. Closer inspection at higher resolution is needed to differentiate between these two possibilities.

Sulfide inclusions, microns to hundreds of microns in size, are seen in some unzoned metal particles in CBs. Based on our observations, our qualitative estimate is that >80% of all metal particles in CBa's contain sulfide inclusions. In CBb HH 237, the abundance is lower, but we estimate >50%, and in CBb QUE 94411, we estimate <50%. Sulfide inclusions are heterogeneously dispersed throughout the individual kamacite grains and within the larger metal particles (Figure 4c). Not all kamacite grains with sulfide inclusions have arcuate textures along grain boundaries; however, sulfide inclusions can coexist in the same metal particle as the arcuate sulfides (Figure 4d). Small inclusions, ≤5 μm in size, are mostly circular in shape, and tend to occur in densely concentrated clusters within a grain. These clusters are often found around kamacite grain boundaries. Larger inclusions, ≥15 μm in size, are mostly irregular in shape (Figure 4e), and there tend to be greater distances between neighboring large sulfide inclusions, compared to the smaller inclusions (Figures 4f, 5a). Inclusions between 5-15 μm in size are both circular and elongated in shape in all four meteorites. Weisberg et al. (2001) showed that a thin, sub-micrometer rim of high Ni is found around most sulfide inclusions. We observe a similar feature as a higher Z rim at the sulfide-metal interface in some grains in BSE images (Figures 5b, 6a-6g).

Most sulfide inclusions in the four CB meteorites are homogeneous and composed of a Cr-rich monosulfide solid solution, MSS_1, $(Fe,Ni,Cr)_{1-x}S$. These

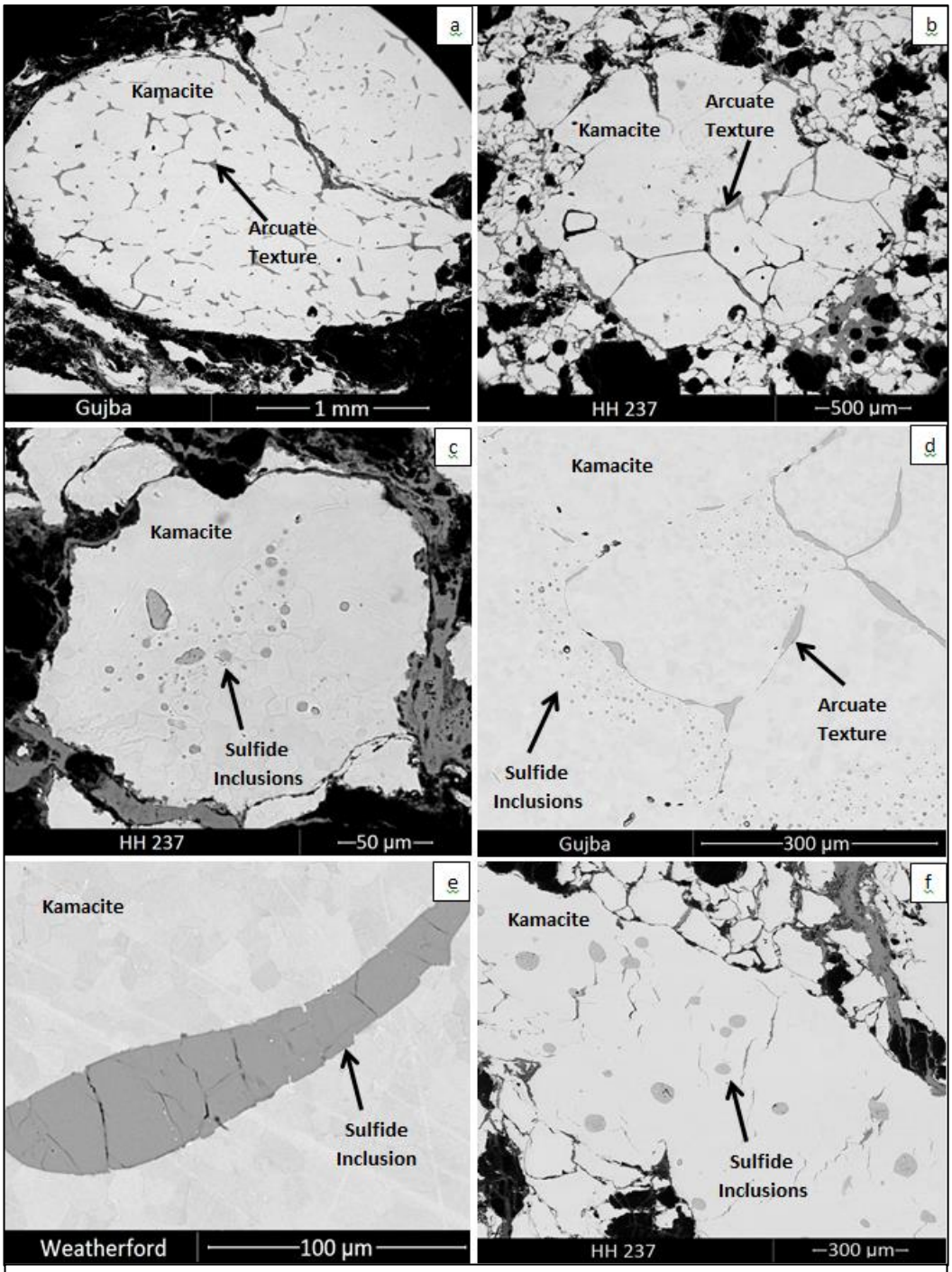

Figure 4. Backscattered electron images of metal particles and sulfides in CB meteorites. [a] Metal particle with arcuate sulfide textures along kamacite grain boundaries in CBa Gujba; [b] Metal particle in CBb HH 237. Sulfides occur along grain boundaries in what are possibly arcuate textures; [c] Sulfide inclusions heterogeneously dispersed throughout a metal particle in HH 237. Sizes of sulfide inclusions are also variable; [d] Arcuate sulfide textures and small, circular sulfide inclusions. Sulfide inclusions in a metal particles in CBa Gujba occur in densely concentrated clusters that located near grain boundaries; [e] Large, elongated homogeneous sulfide inclusion in CBa Weatherford; [f] Large sulfide inclusions in CBb HH 237 that are spread hundreds of microns apart.

inclusions range from small, circular, micrometer-sized inclusions to larger, elongated inclusions hundreds of microns in size (Figure 4e). Some metal particles contain a few homogeneous sulfide inclusions, while others contain hundreds (Figure 5a). Metal blebs are observed in some homogeneous inclusions [Weisberg et al., 2001]. These blebs tend

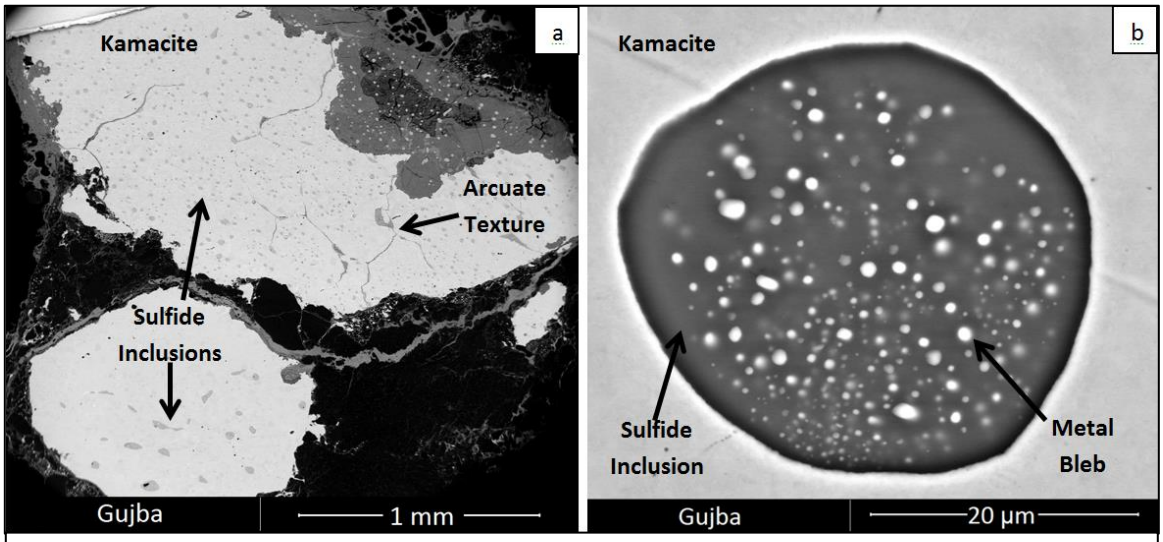

Figure 5. Backscattered electron images of metal particles with homogeneous sulfide inclusions in Gujba. [a] Two adjacent metal particles with different textures. Top particle contains hundreds of small, circular sulfide inclusions, as well as arcuate sulfides on grain boundaries. Bottom particle contains a few tens of larger, elongated sulfide inclusions. [b] Metal blebs in a homogeneous MSS_1 host. Blebs are mainly concentrated away from the edges of the inclusion.

to be nanometer-sized, but some can be on the sub-micrometer-scale. Metal blebs are typically clustered towards the centers of the sulfide inclusions (Figure 5b).

Exsolved sulfides are also found in CB metal particles. Based on our detailed observations, exsolved sulfides are found in <20% of metal particles in Gujba. As a qualitative estimate, Weatherford and HH 237 show similar abundances at <20%. QUE 94411 shows the lowest abundance, where sulfides were only observed in two metal particles (<2%). Inclusions that show exsolution are typically 3-50 µm in diameter. Larger inclusions are irregular in shape, and smaller inclusions tend to be circular or elliptical. Most exsolved sulfides consist of linear, parallel lamellae; typically lamellae of

daubreelite ($FeCr_2S_4$) in a MSS_1 host (Figure 6a). We observed some inclusions that appear to consist of three phases based on differences in greyscale in BSE images (Figure 6b); however, due to the small size of the lamellae, it was not possible to resolve the compositions of individual phases using EPMA techniques alone. The size of the lamellae, as well as the distance between lamellae, is variable among exsolved sulfide inclusions. Some inclusions have tens of thin, parallel daubreelite lamellae (Figure 6c), while others only have 1-2 relatively thick bands (Figure 6d). In some BSE images, it appears as though the daubreelite lamellae extend further into the surrounding metal than the MSS_1 lamellae (Figures 6c and 6g). A few exsolved sulfides in Gujba and Weatherford contain blocky daubreelite, in contrast to the typical linear lamellae (Figure 6e; A-3). The blocky texture has the same composition as the linear texture. A very fine-grained sulfide texture is also seen in Figure 6e. Small inclusions, which typically form in dense clusters within a kamacite grain (Figure 6f), tend to only contain the same type of sulfide in individual kamacite grains (i.e. homogeneous only or exsolved only). However, homogeneous and exsolved sulfides can coexist in the same metal particle. Metal blebs are also observed in exsolved sulfides (Figure 6g), and while most tend to be located within the centers of inclusions, we observed examples where blebs are located in the outer regions as well (Appendix A-1). Metal blebs in exsolved sulfides are always at the nanometer-scale, and we did not observe any larger ones like those found in some homogeneous inclusions. Arcuate sulfides are mostly homogeneous, but a few contain areas that might possibly be a blocky exsolution texture (Figure 6h). However, none of the arcuate textures contain linear lamellae of daubreelite.

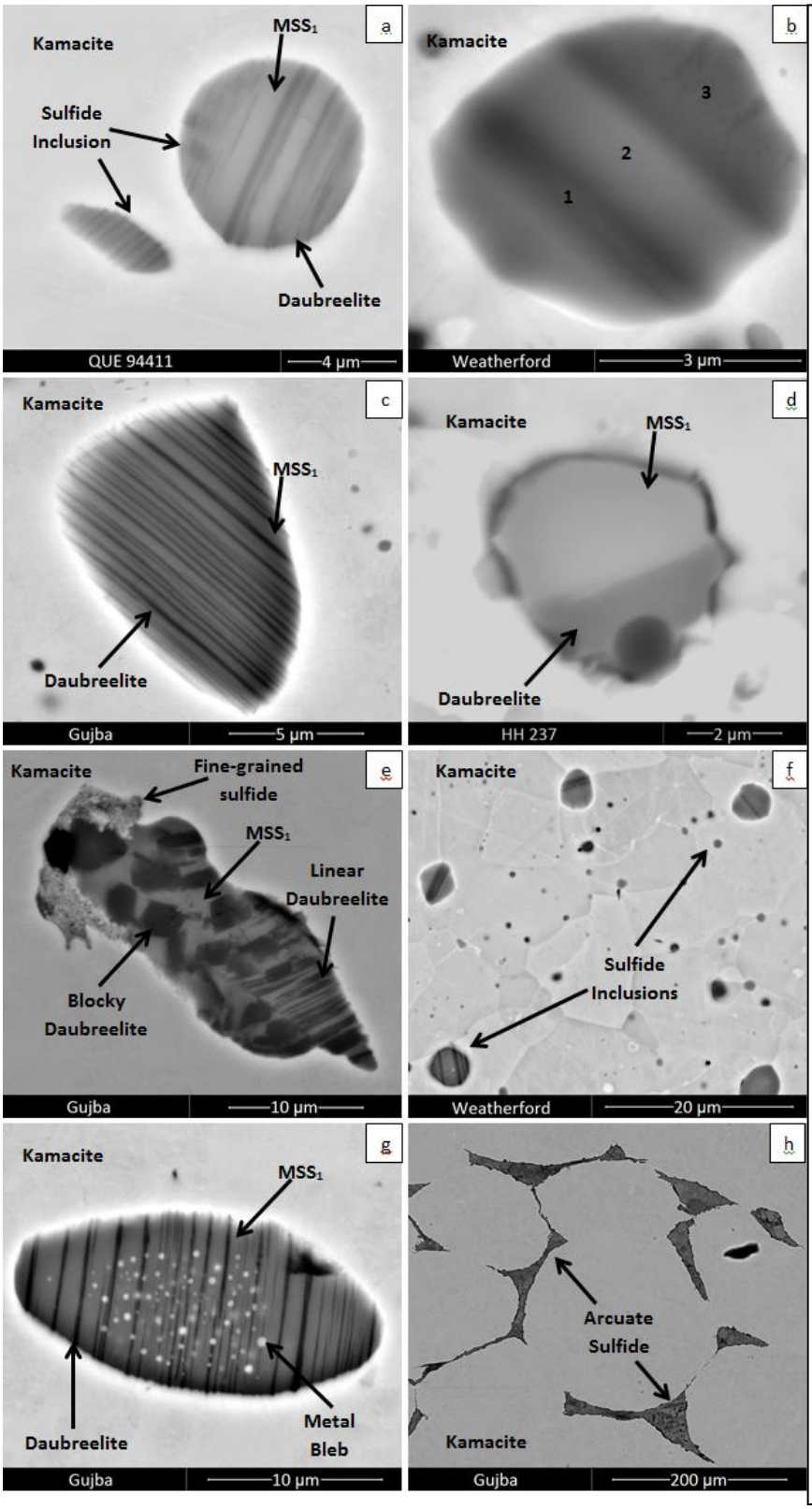

Figure 6.
Backscattered electron images of exsolved sulfide inclusions from CBa Gujba and Weatherford, and CBb HaH 237 and QUE 94411. [a] Typical sulfide exsolution texture showing linear, parallel lamellae of daubreelite in a MSS_1 host; [b] Three-phase grain showing three different grey levels (1, 2, 3). Compositions of each phase were not determined due to the small size of the lamellae; [c] Exsolved sulfide with tens of thin, linear daubreelite lamellae; [d] Exsolved sulfide with only one region of each phase surrounded by a dark rim; [e] Exsolved sulfide with regions of blocky daubreelite, and linear daubreelite lamellae in a MSS_1 host. A very fine-grained sulfide is seen at the top left of the inclusion. See Appendix 1 for X-ray maps; [f] Cluster of small, circular exsolved inclusions in Weatherford; [g] Metal blebs in an exsolved sulfide inclusion; [h] Arcuate sulfide showing possible daubreelite exsolution.

A few metal particles show deformation features, and these features are also seen in the sulfide inclusions. Some metal particles are elongated and show signs of plastic deformation [Weisberg et al., 2002]. Deformed metal particles can be sulfide-free, but others have sulfide inclusions that bend in the same manner, indicating deformation occurred after the sulfides crystallized (Figure 7a). Deformation of metal particles is seen in all four meteorites, but is rare in Gujba, which is consistent with the rounded shape of

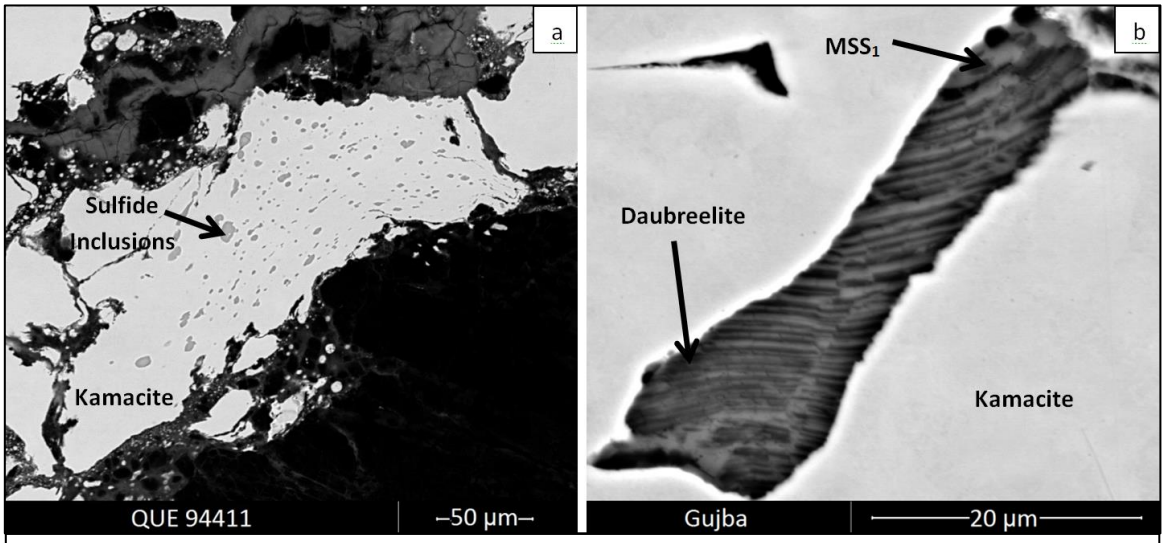

Figure 7. Backscattered electron images of deformed metal particles and sulfide inclusions in CB meteorites. [a] Deformed metal particle in QUE 94411. Deformation in the metal is highlighted by sulfide inclusions, which curve in the same trend; [b] Deformed daubreelite lamellae in an exsolved sulfide in CBa Gujba.

most of its metal particles. Deformation can also be seen in lamellae of some exsolved sulfides, which are slightly curved and irregular in shape (Figure 7b). Most of the deformed sulfides are large in size (~20-50 µm) and elongated.

Sulfide-metal eutectic textures are observed close to the edges of some metal particles (Figure 8). Eutectic "fizzed" or dendritic textures form when sulfide inclusions and surrounding metal were heated to the point of melting, >950°C, and then rapidly cooled [Scott, 1982; Chappell et al., 2011]. Eutectic textures are more common in the

CBa meteorites, especially in Weatherford. A few metal particles in the CBb meteorites exhibit these textures as well.

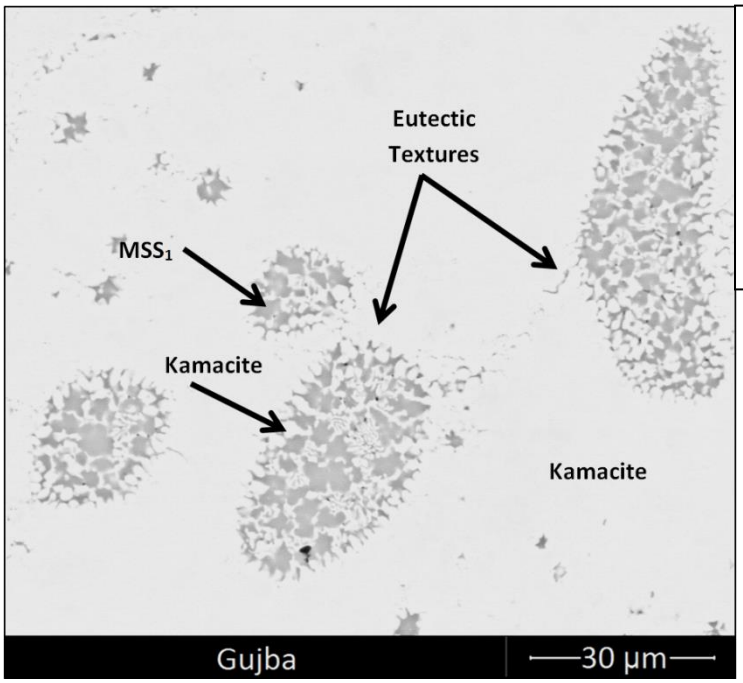

Figure 8. Backscattered electron image of eutectic textures in CBa Gujba. The "fizzed" sulfide-metal texture indicates heating to 950°C, followed by rapid cooling.

Using mosaics of high-resolution BSE images for each meteorite (Figure 2) and the data processing program, ImageJ, we determined abundances of metal particles (Table 2) and abundances of sulfides in different types of sulfide inclusions (Table 3). Metal comprises ~50 vol.% in Gujba, QUE 94411, and HH 237. Weatherford is slightly lower at ~40 vol.%. Previous studies have reported metal volume to be between 60-80 vol.% [Weisberg et al., 2001; Krot et al., 2002; Campbell et al., 2005b], which is much higher than our samples. Our values are more similar to Rubin et al. (2003), who found metal volume to be ~41% in Gujba. Nearly all large metal particles in CBa Gujba and

Table 2. Metal abundances obtained from BSE mosaics and processed with ImageJ.

	Gujba	Weatherford	QUE 94411	HH 237
Area (mm^2)	347.4	217.4	136.5	102.1
Metal Area (mm^2)	170.3	88.0	67.6	51.5
Metal %	49.0	40.5	49.5	50.4

Weatherford contain sulfide inclusions, >80%. Quantitative measurements on CBb meteorites are difficult, due to the small size of the metal particles; however, we estimate <50% of metal particles contain sulfides. Rubin et al. (2003) observed that metal particles in CBa Gujba contain 0-20% sulfide inclusions. Our observations show that sulfides in CBa meteorites comprise ~0.5-5% of the area of individual metal particles. Metal particles in CBb meteorites, which are mainly smaller in size compared to those in CBa,

Table 3. Textural analysis of individual metal particles and sulfide contents obtained from BSE mosaics and processed with ImageJ.

		Metal Particles				Sulfide Inclusions				Description of Sulfides
	Particle #	Width (µm)	Length (µm)	Aspect Ratio	Area (mm^2)	Area (mm^2)	Av. Area ($µm^2$)	Av. Dia. (µm)	% Area	
Gujba	12	1805	2988	1.66	4.24	0.03	9	3	0.71	Homogeneous, Small sulfides
	13	1733	2103	1.21	2.86	0.11	104	9	3.87	Homogeneous, Large sulfides
	14	2891	3281	1.13	7.45	0.30	98	9	3.98	Homogeneous, Small & large sulfides
	15	693	1326	1.91	0.72	0.04	31	5	5.19	Eutectic textures only
	16	1822	2553	1.40	3.65	0.05	19	4	1.26	Homogeneous, Large sulfides
	5	2235	2747	1.23	4.82	0.05	26	5	1.14	Exsolved
	7	1050	2254	2.15	1.86	0.01	10	3	0.39	Exsolved
	3	3622	4640	1.28	13.20	0.25	46	7	1.90	Exsolved
	17	3718	5110	1.37	14.92	0.67	58	7	4.49	Exsolved
Weatherford	19	2695	3254	1.21	5.50	0.18	31	6	3.33	Homogeneous, Small & large sulfides
	2	1270	3152	2.48	3.14	0.07	35	4	2.14	Homogeneous, Small & large sulfides
	18	637	1976	3.10	0.99	0.03	6	3	2.78	Homogeneous, Small sulfides
	17	1170	1246	1.06	1.14	0.03	43	8	2.31	Homogeneous, Large sulfides
	7	4132	5066	1.23	16.44	0.17	44	6	1.05	Homogeneous, Large sulfides
	20	327	424	1.29	0.11	0.00	22	6	3.65	Eutectic textures only
	8	1594	2246	1.41	2.81	0.06	9	3	2.30	Exsolved
	16	819	1242	1.52	0.80	0.02	4	2	1.99	Exsolved, Small & large
	6	729	2688	3.69	1.54	0.02	11	3	1.52	Exsolved
QUE 94411	12	535	1258	2.35	0.53	0.02	13	4	4.13	Homogeneous, small, high sulfide abundance
	13	530	766	1.45	0.32	0.01	8	3	2.26	Homogeneous, small, high sulfide abundance
	16	537	899	1.67	0.38	0.02	9	3	5.03	Homogeneous, large
	22	686	973	1.42	0.52	0.04	22	4	7.70	Homogeneous, large & small
	23	382	547	1.43	0.16	0.01	8	3	3.46	Homogeneous, large & small
	24	392	566	1.45	0.17	0.01	9	3	5.31	Homogeneous, small
	25	186	215	1.15	0.03	0.00	30	5	4.33	Homogeneous, large
	21	130	244	1.87	0.02	0.00	17	4	3.71	Exsolved, large
	15	260	464	1.78	0.09	0.00	10	3	4.79	Exsolved, large & small
HH 237	6	343	428	1.25	0.12	0.00	31	6	3.95	Homogeneous, large
	7	393	838	2.13	0.26	0.02	17	5	6.68	Homogeneous, small, high sulfide abundance
	16	1975	2864	1.45	4.44	0.02	5	2	0.51	Homogeneous, large, not many sulfides
	17	397	1298	3.27	0.41	0.02	22	4	4.85	Homogeneous, large, high sulfide abundance
	23	1344	1658	1.23	1.75	0.04	9	3	2.22	Homogeneous, small and large
	24	836	998	1.19	0.66	0.02	9	3	2.69	Homogeneous, small and large
	29	496	579	1.17	0.23	0.01	7	3	4.18	Homogeneous, small, high sulfide abundance
	8	180	287	1.59	0.04	0.00	10	3	2.07	Exsolved, large
	19	574	754	1.31	0.34	0.01	22	6	2.15	Exsolved, large

- Length, width, and area measured by pixel count
- Aspect ratio = length / width
- Average diameter calculated from averaging the longest length (in pixels) of individual sulfides
- % area = Percent of sulfides in metal particle (total area of sulfide / total area of metal)

contain sulfide inclusions ranging from ~0.5 to 7% of the area of individual metal particles (Figure 9c). Regardless of the dimensions of the metal particles in CBa's and CBb's, the modal abundance of sulfides for both groups is very similar. Although they are generally similar, closer examination of CBa versus CBb shows that there is a weak trend of higher sulfide abundance in CBb grains. The similarities in modal abundance also show that the size of the sulfides does not dictate the modal abundance of sulfides. Large sulfides separated by great distances constitute roughly the same area as do small

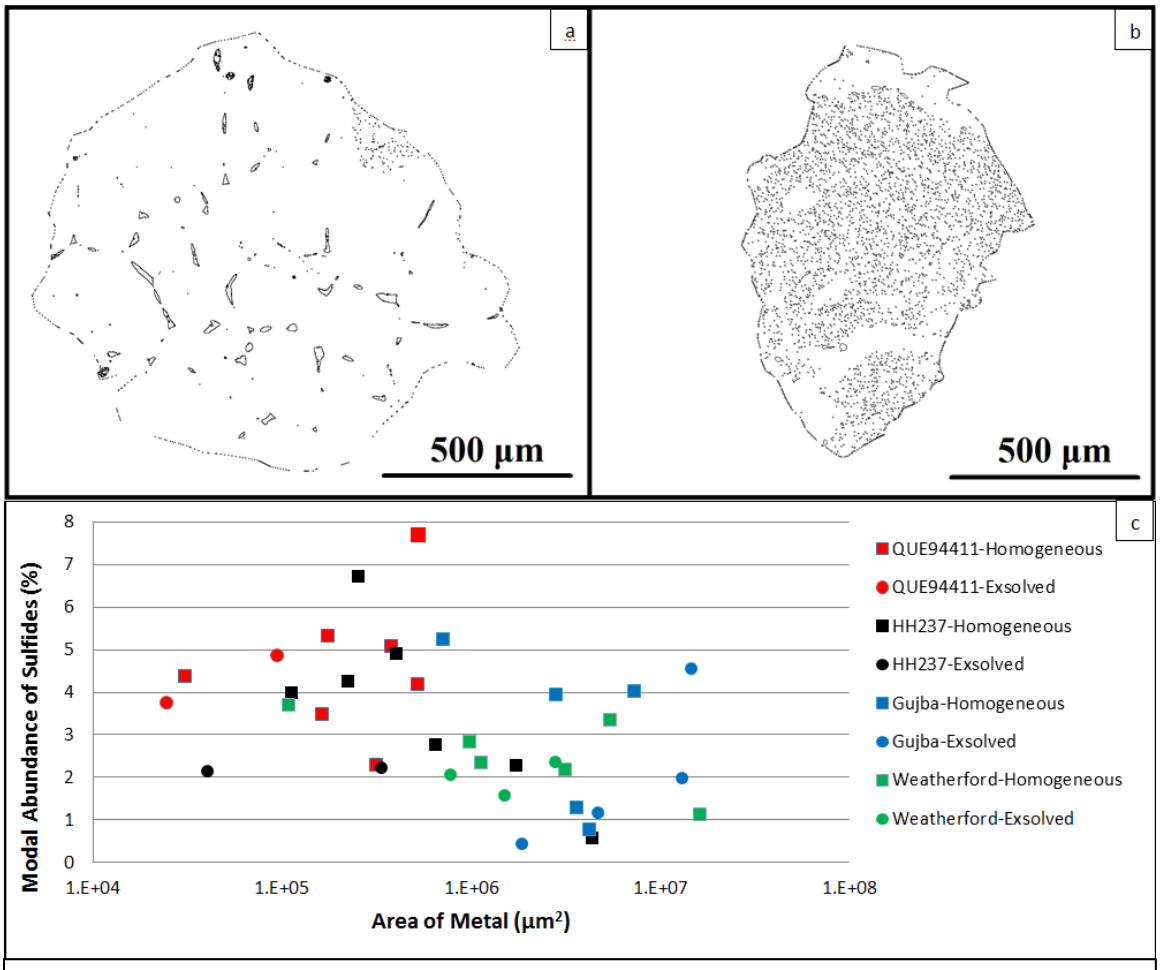

Figure 9. Sulfide modal abundances obtained from high-resolution BSE mosaics and processed with ImageJ software. [a] Metal particle 17 from CBa Weatherford containing large, homogeneous sulfide inclusions spread out within the particle. Modal abundance of sulfides is ~2%; [b] Metal particle 16 from CBa Weatherford containing small, homogeneous and exsolved sulfide inclusions in dense clusters. Modal abundance of sulfides is ~2%; [c] Modal abundance of sulfides (%) vs. size of metal particle for metal particles with homogeneous and exsolved sulfide inclusions in CB meteorites.

sulfides found in densely populated clusters (Figure 9a,b). The average diameter of sulfide inclusions in CBa meteorites is slightly larger (~5 μm) than those in CBb meteorites (~3.5 μm). We observe that Gujba contains the greatest number of metal particles containing exsolved sulfide inclusions, ~16%, whereas QUE 94411 contains the smallest number, with only two metal particles (<2%). In all four meteorites, nanometer-to-micrometer-sized metal blebs are present in less than 5% of sulfide inclusions.

X-ray maps were obtained from the electron microprobe to analyze elemental distributions in sulfides and metal grains. Figure 10 shows Cr, Fe, Ni, and S maps from an exsolved sulfide inclusion within a metal grain in Gujba. The Cr map shows differences between the Cr-rich phase (daubreelite) and the Cr-poor phase (MSS_1). Differences in Fe content between MSS_1 and daubreelite are not so obvious because of

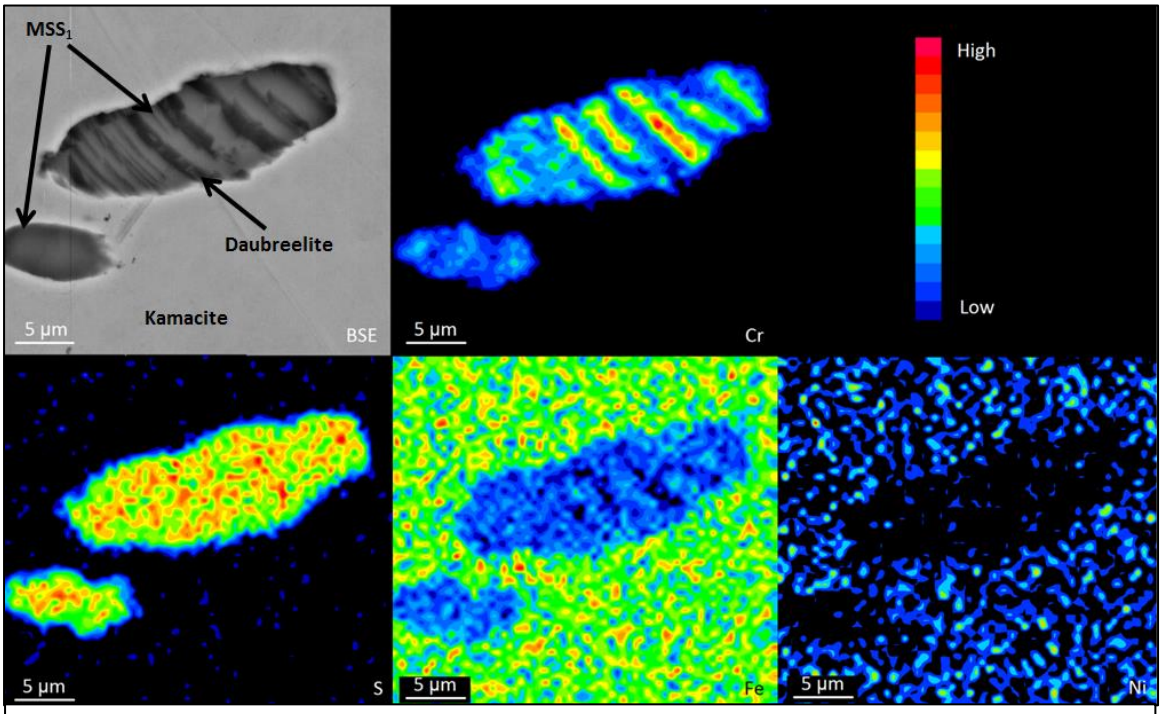

Figure 10. EPMA X-ray maps of two sulfides in CBa Gujba: one exsolved and one homogeneous. The sulfide inclusions are located in a kamacite (Fe,Ni) grain. For the exsolved grain, the Cr map shows individual lamellae of daubreelite (red/yellow) and MSS_1 (green/blue). The sulfur distribution is relatively constant throughout the inclusion. The X-ray maps have been smoothed to remove pixelation.

the high contrast with the surrounding Fe,Ni metal, but MSS_1 shows slightly higher levels of Fe than daubreelite. Ni is located entirely within the surrounding metal. The sulfur content is relatively constant throughout the exsolved sulfide. X-ray mapping of sulfide inclusions showed the common presence of sub-micrometer inclusions of phosphides at the interface between the sulfide and the surrounding metal (Figure 11). These phosphide inclusions could not be observed in BSE images. See Appendix A for more X-ray maps of sulfide inclusions.

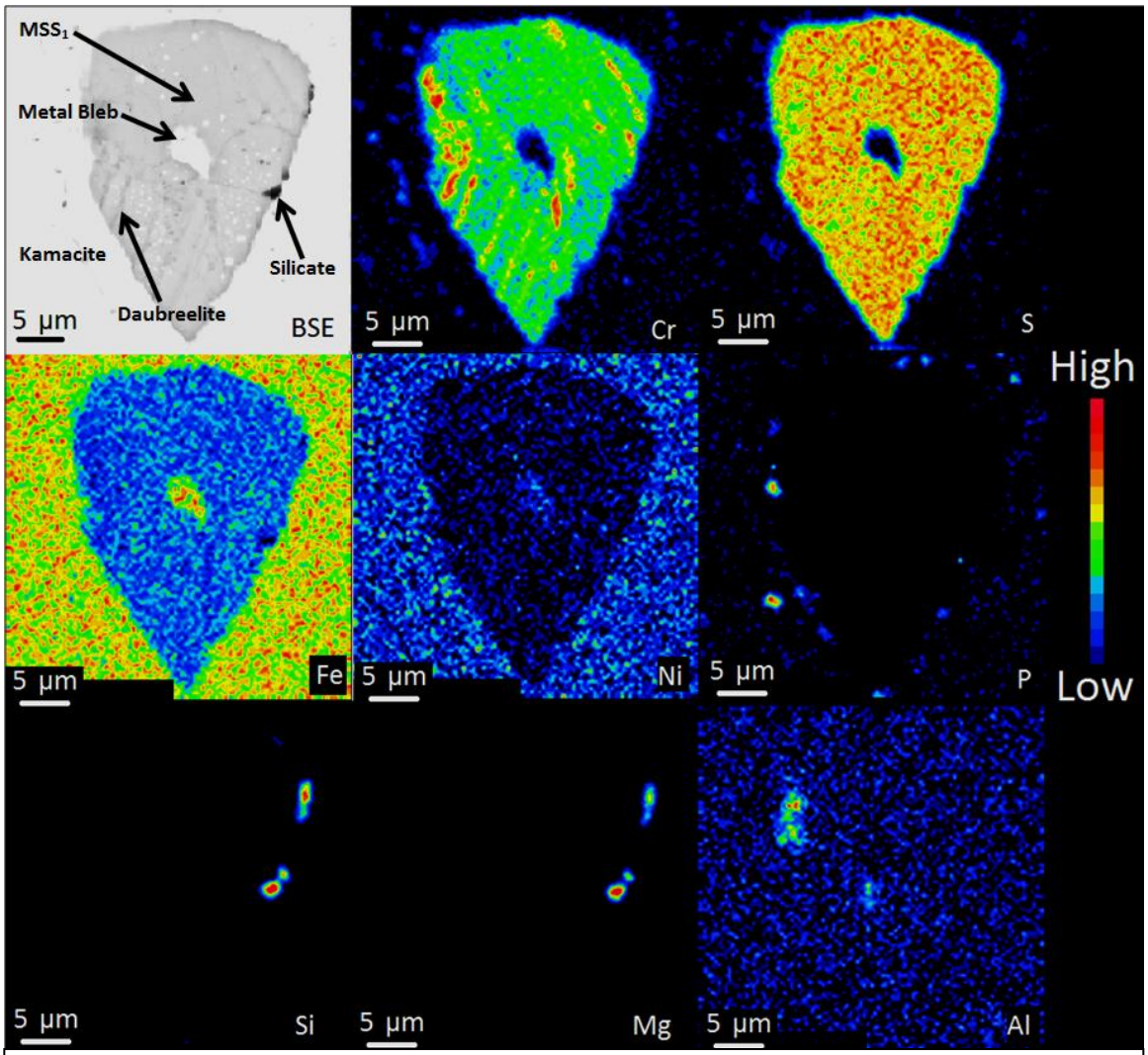

Figure 11. EPMA X-ray maps of an exsolved sulfide in CBa Gujba. In the Cr map, daubreelite lamellae (red) are seen in a MSS_1 host (green). The sulfide inclusion is located in a kamacite grain, and contains a ~5 µm-size metal bleb (Fe, Ni maps). Small silicates (Si, Mg maps) and phosphide inclusions (P map) are located at the interface between the sulfide inclusion and the surrounding kamacite metal. The Al map shows a region of high Al at the sulfide-metal interface – we have not identified this phase.

In addition to sulfide inclusions, silicate inclusions are also observed in a few kamacite grains in all four meteorites. These inclusions are typically 1-50 μm in diameter, and can be circular or elongated in shape (Figure 12a). Silicate inclusions are usually clustered together; they are found in areas of silicate-only inclusions and are also found coexisting with sulfide inclusions [see also Weisberg et al., 2001]. Nanometer-sized silicate inclusions also occur around a few sulfide inclusions at the sulfide-kamacite interface (Figure 11). We did not analyze individual silicate inclusions with EPMA, but we obtained an EDS spectrum from the SEM (Figure 12b), which showed that these inclusions have compositions similar to a Ca-bearing pyroxene.

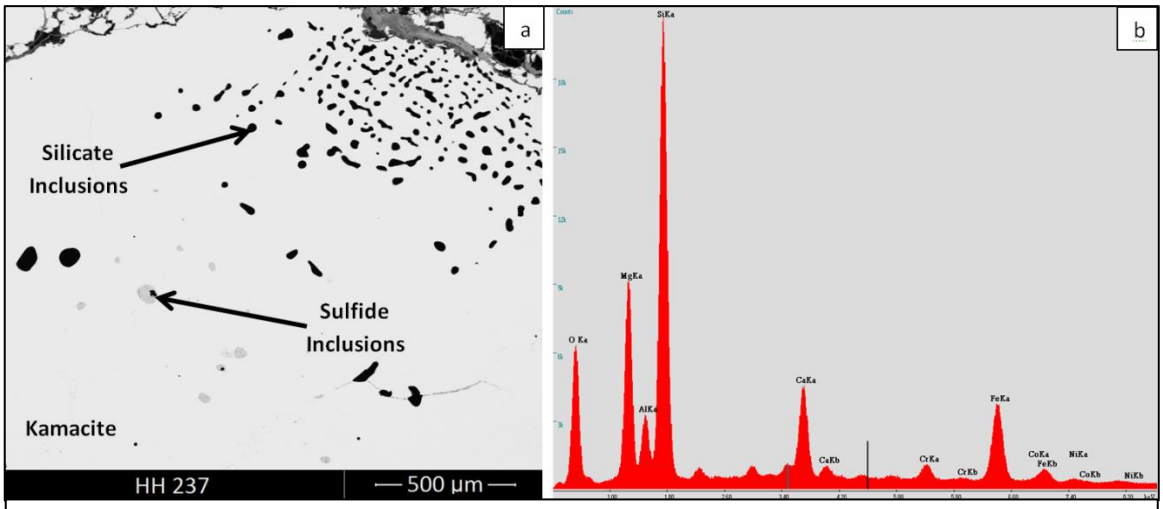

Figure 12. [a] BSE image of a metal particle in HH 237 with silicate and sulfide inclusions. [b] EDS spectrum of a silicate inclusion showing a composition similar to a Ca-bearing pyroxene.

3.2 Mineral Compositions Obtained by EPMA

Compositions of sulfides determined by EPMA are given in Table 4. Most homogeneous sulfides contain <4 wt.% Cr, and are monosulfide solid solution, MSS_1, $(Fe,Ni,Cr)_{1-x}S$. These sulfide inclusions have been previously described as Cr-bearing troilite (FeS) [Weisberg et al., 1990; 2001; Krot et al., 2002; Rubin et al., 2003];

however, we believe that because of the high amount of Cr in the sulfide, it is better described as MSS_1. Table 4 gives the sum of cations (Fe, Cr, Ni, V, Cu, Zn), based on 1 sulfur anion for this phase. If the homogeneous sulfides were troilite, then the ratio of cations:anion should be 1:1; however, our cation total is less than 1 for the majority of our analyses. The range in the sum of cations is between 0.953-1.010. The cation sum obtained with TEM analyses (see below) is 0.954-0.965, depending on the vanadium content, which indicates a cation deficiency consistent with MSS_1. In exsolved grains, the Cr-rich phase is daubreelite, $FeCr_2S_4$. EPMA analyses do not give the end-member

Table 4. Representative EPMA and TEM-EDS analyses of sulfides in CBa and CBb meteorites.

Sulfide Composition (Weight %)													
	QUE	HH 237			Weatherford			Gujba					
								EPMA			TEM-EDS		
	Homog	Homog	Ex-MSS	Ex-Daub	Homog	Ex-MSS	Ex-Daub	Homog	Ex-MSS	Ex-Daub	L-V MSS	H-V MSS	Daub
Grain	G5_S1	G17_S2	G19_S4	G19_S5	G5_S3	G9_S3	G8_S7	G11_S1	G9_S2	G6_S2	Spec 11	Spec 12	Spec 51
Si	B.D.	B.D.	B.D.	B.D.	B.D.	B.D.	B.D	B.D.	B.D.	B.D.	N.A.	N.A.	N.A.
P	B.D.	B.D.	B.D.	B.D.	B.D.	B.D.	0.06	B.D.	B.D.	B.D.	N.A.	N.A.	N.A.
S	36.6	37.2	36.5	41.7	36.7	37.2	36.5	36.9	37.5	38.4	37.5	37.8	42.6
V	0.02	0.06	0.37	0.62	B.D.	B.D.	0.38	B.D.	0.29	0.27	0.38	1.88	0.05
Cr	2.07	2.37	7.56	24.2	2.67	6.41	15.5	2.29	6.76	15.6	6.02	4.23	35.3
Mn	0.02	0.06	0.11	0.24	0.03	0.32	0.09	0.04	0.26	0.18	N.A.	N.A.	N.A.
Fe	61.0	60.7	54.7	32.6	59.5	54.3	45.1	60.1	54.8	44.3	56.0	56.2	22.0
Co	B.D.	0.02	B.D.	B.D.	B.D.	B.D.	0.02	0.03	B.D.	B.D.	N.A.	N.A.	N.A.
Ni	0.26	0.19	0.86	0.11	0.20	0.25	0.69	0.21	0.14	0.20	0.12	0.00	0.00
Cu	B.D.	B.D.	B.D.	B.D.	B.D.	B.D.	0.10	B.D.	B.D.	0.14	N.A.	N.A.	N.A.
Zn	0.02	B.D.	B.D.	0.24	B.D.	B.D.	B.D	B.D.	B.D.	B.D.	N.A.	N.A.	N.A.
Total	100.02	100.58	100.03	99.61	99.05	98.50	98.38	99.50	99.72	99.05	100.00	100.01	100.00
Sulfide Composition (Atomic)													
Si	--	--	--	--	--	--	--	--	--	--	--	--	--
P	--	--	--	--	--	--	--	--	--	--	--	--	--
S	1.000	1.000	1.000	4.000	1.000	1.000	4.000	1.000	1.000	4.000	1.000	1.000	4.000
V	--	0.001	0.006	0.038	--	--	0.026	--	0.005	0.017	0.006	0.031	0.003
Cr	0.035	0.039	0.128	1.430	0.045	0.106	1.049	0.038	0.111	0.999	0.099	0.069	2.046
Mn	--	0.001	0.002	0.013	0.001	0.005	0.006	0.001	0.004	0.011	--	--	--
Fe	0.956	0.938	0.861	1.794	0.931	0.838	2.840	0.935	0.839	2.650	0.858	0.854	1.189
Co	--	--	--	--	--	--	--	--	--	--	--	--	--
Ni	0.004	0.003	0.013	0.006	0.003	0.004	0.041	0.003	0.002	0.011	0.002	0.000	0.000
Cu	--	--	--	--	--	--	0.005	--	--	0.008	--	--	--
Zn	--	--	--	0.011	--	--	--	--	--	--	--	--	--
Cations	0.995	0.982	1.010	3.292	0.980	0.953	3.967	0.977	0.961	3.696	0.965	0.954	3.238

Homog. = Homogeneous sulfide
Ex-MSS = MSS lamella in exsolved sulfide
Ex-Daub = Daubreelite lamella in exsolved sulfide

L-V MSS = Low-V phase in MSS lamella
H-V MSS = High-V phase in MSS lamella

B.D. = Below detection
N.A. = Not analyzed

compositions of daubreelite and MSS_1 because the widths of the lamellae are smaller than the beam size, so most analyses are mixtures of the two phases. Table 4 gives representative EPMA analyses that lie at the extremes of the range of mixed compositions. End-member analyses of each phase obtained with TEM techniques are also included in Table 4: these analyses are discussed in the next section. Tables of individual sulfide analyses are given in Appendix B.

Compositions of homogeneous (unzoned) metal and metal blebs, also obtained by EPMA, are given in Table 5. All metal grains are kamacite (Fe,Ni). The average Fe content is ~93 wt.% and Ni is ~6 wt.%. The range for Ni in CBa meteorites is 5.2-7.2 wt.% and CBb is 4.8-9.2 wt.% (Figure 13). This is comparable to Weisberg et al. (2001), where they found Ni contents to be 4.8 – 8.2 wt.% in CBa and 4.1-14.8 wt.% in CBb meteorites. Because this study primarily focuses on sulfide inclusions, we only analyzed homogeneous (unzoned) metal grains, since zoned metal particles do not contain sulfide inclusions

Table 5. Average compositions of metal in CBa and CBb meteorites determined by EPMA.

Average Metal Composition (Weight %)					
	QUE 94411	**HH 237**	**Weatherford**	**Gujba**	**Metal Blebs**
#	21	30	32	56	4
Si	B.D.	0.03 (0.02)	0.02 (0.02)	0.02 (0.02)	0.02 (0.01)
P	0.50 (0.47)	0.32 (0.06)	0.34 (0.03)	0.32 (0.04)	0.21 (0.15)
S	0.02 (0.06)	B.D.	0.07 (0.14)	0.01 (0.01)	0.19 (0.10)
V	B.D.	B.D.	B.D.	B.D.	B.D.
Cr	0.12 (0.04)	0.19 (0.10)	0.22 (0.09)	0.24 (0.10)	0.50 (0.08)
Mn	B.D.	B.D.	B.D.	B.D.	B.D.
Fe	94.4 (1.31)	94.3 (0.69)	93.2 (0.57)	93.1 (0.91)	92.9 (3.52)
Co	0.29 (0.04)	0.29 (0.02)	0.29 (0.01)	0.31 (0.03)	0.25 (0.10)
Ni	6.08 (0.96)	5.87 (0.43)	5.85 (0.36)	6.23 (0.65)	6.56 (2.89)
Cu	B.D.	B.D.	B.D.	B.D.	B.D.
Zn	B.D.	B.D.	B.D.	B.D.	B.D.
Total	101.4 (0.25)	101.0 (0.38)	100.0 (0.40)	100.3 (0.51)	100.6 (0.65)
Average Metal Composition (Atomic)					
Si	--	--	--	--	--
P	0.01	0.01	0.01	0.01	
S	--	--	--	--	--
V	--	--	--	--	--
Cr	0.00	0.00	0.00	0.00	0.01
Mn	--	--	--	--	--
Fe	0.93	0.93	0.93	0.93	0.92
Co	--	--	--	--	--
Ni	0.06	0.06	0.06	0.06	0.06
Cu	--	--	--	--	--
Zn	--	--	--	--	--
Total	1.00	1.00	1.00	1.00	1.00

B.D. = Below detection
Standard deviations given in parentheses
= Number of analyses included in average

[Campbell et al., 2005]. We therefore did not find any high Ni content, which is attributable to zoned metal in the CBb meteorites. Figure 13 shows Co vs. Ni contents in metal particles in each meteorite. Most metal compositions in the four CB meteorites plot slightly above the solar ratio line. The grey ellipse in Figure 13 shows the range of metal compositions in CBa Weatherford and CBb QUE 94411 from Weisberg et al. (2001). The data from this study fall within the upper region of this grey ellipse. Differences between our data and the grey ellipse are possibly due to the fact that we focused this study on homogeneous metal grains with sulfide inclusions; therefore, we could have excluded some metal grains that would fall in the lower region of the grey ellipse.

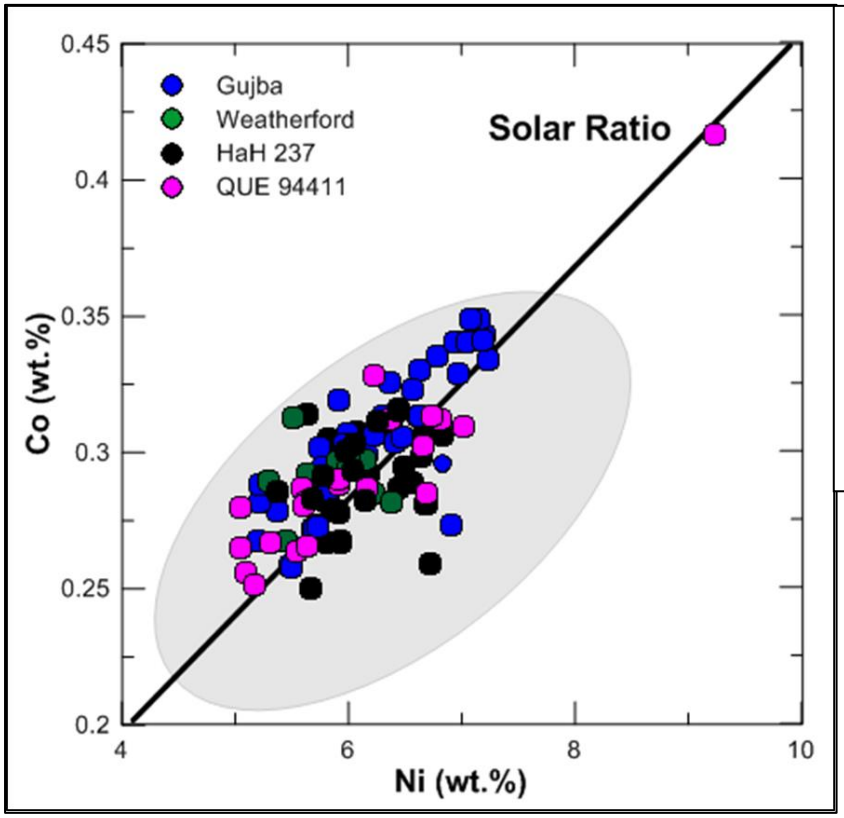

Figure 13. Co and Ni data from kamacite metal obtained using EPMA. CB homogeneous (unzoned) metal analyses lie on and slightly above the solar ratio line. The grey ellipse represents analyses of homogeneous metal particles from CBa Weatherford and CBb HH 237 from Weisberg et al. (2001).

Metal grains also contain minor amounts of phosphorus (0.1-1.6 wt.%), cobalt (0.2-0.4 wt.%), and chromium (bd-0.4 wt.%) [Table 4 and Appendix B]. Weisberg et al. (2001)

reported similar ranges of P (0.1-0.7 wt.%), Co (0.1-0.5 wt.%), and Cr (bd-0.6 wt.%). A few metal grains in CBa Bencubbin have previously been shown to contain ~2 wt.% Si [Newsom & Drake, 1979; Weisberg et al., 1990], but we did not observe any Si-rich metal in our study. Tables of individual metal analyses are given in Appendix B.

Metal blebs in sulfide inclusions were also analyzed. However, because most blebs are on the nanometer-scale, they are difficult to analyze with EPMA techniques. Compositions of four larger metal blebs in homogeneous sulfides from Gujba and HaH 237 are averaged and included in Table 5, with individual analyses given in Appendix B. The composition of the blebs is similar to the metal surrounding the sulfide inclusions in terms of Ni content, with the exception of one that has higher Ni content (~10 wt.%). The four metal bleb analyses plot a long way off the Co/Ni solar ratio line. The three metal bleb analyses from Gujba plot below the line, whereas the metal host analyses from this meteorite plot slightly above the line.

Individual sulfide and metal analyses are shown on a Fe-Cr-S ternary diagram for each meteorite in Figure 14. Compositions of metal grains and metal blebs are also plotted, but are hard to distinguish as they overlap at the Fe end of the ternary. The composition of stoichiometric daubreelite (44.5 wt.% S, 36.1 wt.% Cr, 19.4 wt.% Fe) is indicated as a point in each diagram. EPMA analyses are differentiated by type of sulfide: homogeneous, homogeneous with metal blebs, and exsolved. The main difference between homogeneous and exsolved sulfides is bulk chromium content. Homogeneous sulfides have low Cr content, and cluster closer to the Fe-S join. If the homogeneous sulfides contain metal blebs, compositions lie between MSS_1 and metal (Fe,Ni,Cr), which lies on the Fe,Cr join in the diagram. EPMA analyses of exsolved sulfides lie between

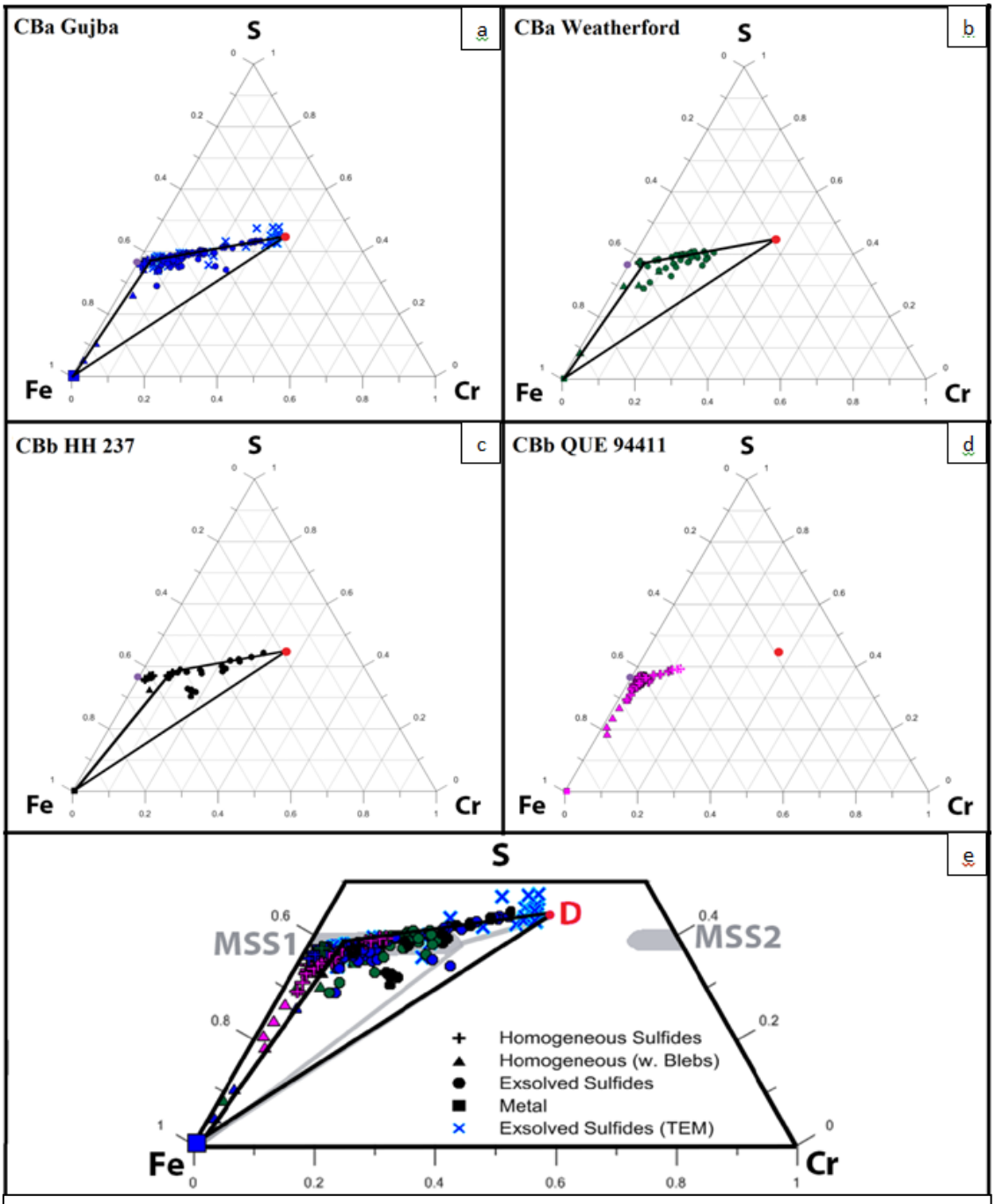

Figure 14. Fe-Cr-S ternary diagrams (wt.%) showing compositions of homogeneous sulfides, homogeneous sulfides with metal blebs, exsolved sulfides, and metal, obtained with EPMA, for each CB meteorite. Stoichiometric daubreelite (red) and troilite (purple) are indicated with a circle on each figure, and extreme compositions of exsolved sulfide phases are represented with a black triangle. [a] CBa Gujba. TEM analyses for Sulfide 5 are also included; [b] CBb Weatherford; [c] CBb HH 237; [d] CBb QUE 94411 [e] Combined data for the four meteorites. Grey areas and grey lines show MSS solid solution fields and phase relations at 600°C from El Goresy & Kullerud (1969). Black triangle shows the three-phase assemblage present in CB meteorites, based on TEM analyses of MSS_1 from Gujba Sulfide 5 and stoichiometric daubreelite.

low Cr MSS_1 and daubreelite, as well as scattering towards the Fe apex when metal blebs are present. We were not able to obtain stoichiometric daubreelite analyses from EPMA techniques because of the small size of the lamellae; however, some analyses of exsolved sulfides in Gujba and HH 237 come close to this composition. For inclusions with μm-sized phases, each EPMA analysis is a mixture of phases. The bulk compositions of the exsolved sulfides lie within the two- or three-phase region defined by the component minerals: bulk compositions of exsolved sulfides are more Cr-rich than bulk compositions of homogeneous grains. Endmember compositions (daubreelite, MSS_1, and metal) are traced in a black triangle on each diagram to show the field of coexisting phases. The triangle on Gujba is defined by TEM data and the triangles on Weatherford and HH 237 are defined by EPMA data. The black triangles are very similar for Gujba, Weatherford, and HH 237. We do not have any analyses of exsolved sulfides for QUE 94411, but it is interesting to note that the homogeneous inclusions with higher Cr content show a similar trend towards the daubreelite point.

Figure 14e is a compilation of data for all four meteorites. The ternary is truncated at 50% S, since none of the data plot above this line. CBa and CBb meteorites show almost the same trends in their sulfide and metal compositions. Fe-Cr-S phase relations at 600°C [El Goresy & Kullerud, 1969] are superimposed on this figure. Grey areas represent MSS solid solution fields (MSS_1 with low Cr and MSS_2 with high Cr), and the grey triangle shows the three-phase region between daubreelite, MSS_1, and Fe metal at this temperature. The three-phase triangle defined by our Gujba TEM data does not plot on the grey triangle, but is offset towards the left of the diagram.

3.3 An EPMA and TEM Study of Gujba Exsolved Sulfide 5

We selected a large, 30 μm long, irregularly shaped exsolved sulfide inclusion from Gujba (Sulfide 5) for a detailed EPMA and TEM study. We chose this particular inclusion because it was one of the largest exsolved sulfides observed, and it had linear, parallel lamellae, which is representative of most exsolved sulfides in CB meteorites. Figure 15a is a BSE image of Sulfide 5 showing that it contains parallel, linear lamellae of daubreelite (dark grey) in a MSS_1 (light grey) host. The inclusion is surrounded by kamacite metal. EPMA X-ray maps were obtained for this sulfide to show elemental distributions. The Cr-map illustrates differences between the high Cr daubreelite and low Cr MSS_1 (Figure 15b; see Appendix A for Fe, Ni, S, and P maps). Yellow and green colors in this map are mixtures of the two phases, since the beam size of the microprobe is larger in diameter than the individual lamellae. The location of a 12 μm line array of EPMA analyses across a portion of the sulfide is shown as a red line in Figure 15a. Figure 15c shows the results for Fe, Cr, S, Mn, and V from this line array. Sulfur stays relatively constant throughout the sulfide, with S content ranging between 35-40 wt.%. High Cr (>25 wt.%) and low Fe (<30 wt.%) corresponds to daubreelite, whereas low Cr (~10 wt.%) and high Fe (~50 wt.%) corresponds to MSS_1. The thin sizes of most of the lamellae cause mixing in all analyses, particularly between 7 – 10 μm in the line array. As discussed later in this section, lamellae are at a low angle relative to the surface. This accentuates the overlap between the lamellae in the excitation volume, causing a mixture of analyses between MSS_1 and daubreelite. Vanadium and manganese are correlated with chromium content in the sulfide: daubreelite shows higher values for both elements. However, we are likely still seeing overlap between phases through EPMA.

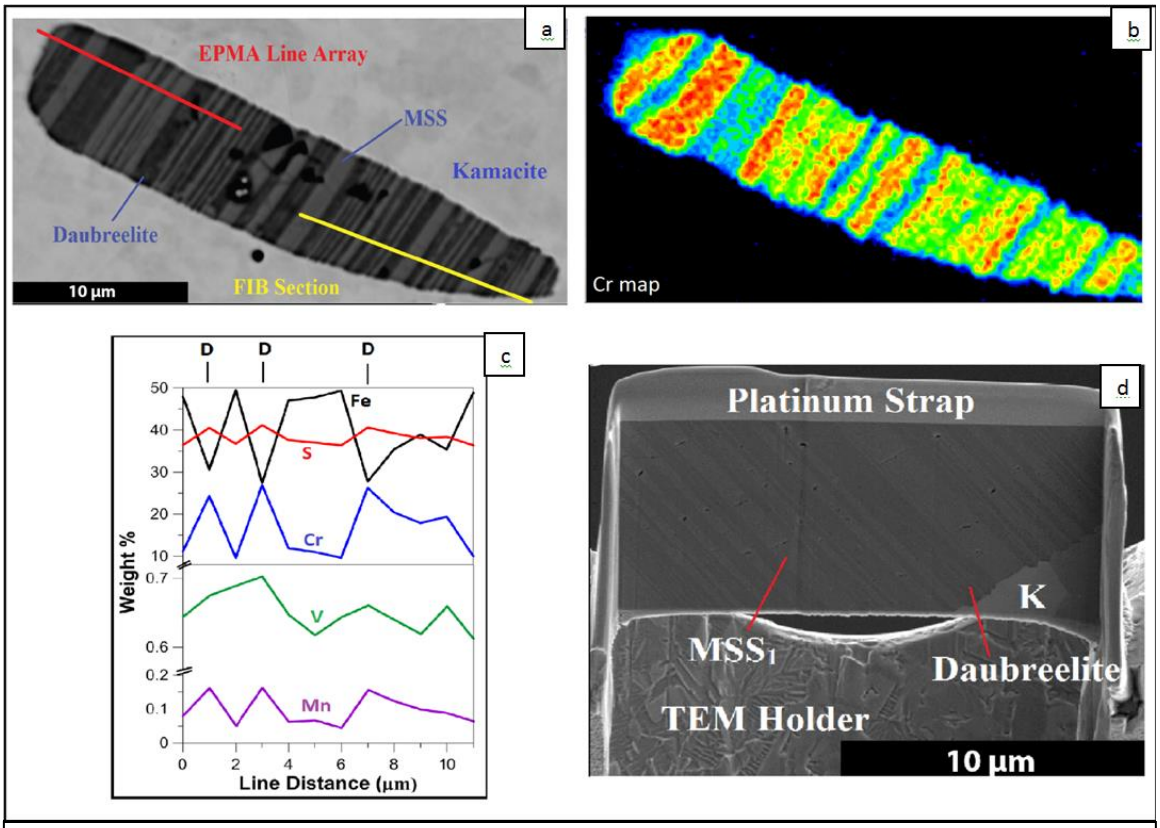

Figure 15. [a] BSE image of exsolved Sulfide 5 in CBa Gujba, located in a kamacite grain. Differences in grey level show a two-phase assemblage of daubreelite (dark grey) and MSS_1 (light grey); [b] EPMA Cr X-ray map of exsolved Sulfide 5. Daubreelite has high Cr content (red) and MSS_1 has low Cr content (blue). Yellow and green colors show mixtures of the two phases due to the thin size of the lamellae; [c] EPMA line array across Sulfide 5. Red line on the BSE image [a] shows the location of the line array. Fe, S, Cr, V and Mn contents vary among the individual lamellae. Areas of high Cr and low Fe are daubreelite (indicated by a "D"). V and Mn follow Cr content, and are higher in daubreelite; [d] SEM image of the FIB section (yellow line on [a]) prepared for TEM analysis. FIB section shows angled, linear, parallel daubreelite lamellae in a MSS_1 host. "K" = kamacite metal.

We used TEM techniques to obtain accurate endmember analyses on the individual lamellae. Because the beam size of the electron microprobe is larger than the individual lamellae, we cannot obtain chemical analyses of each lamella through this method; all EPMA analyses are mixtures of daubreelite and MSS_1. Therefore, we cut a ~20 µm wide section of Sulfide 5 from Gujba with the focused ion beam (FIB) to use for TEM analysis (Figure 15d). The cut is perpendicular to the surface of the sample, and is indicated by a yellow line on Figure 15a. The FIB section shows lamellae are inclined at

a low angle, 47°, relative to the surface. The widths of lamellae are variable, and daubreelite (darker grey in Figures 15a and 15d) lamellae extend farther into the metal phase than MSS_1 lamellae. TEM images show that what appear to be individual lamellae of daubreelite in SEM images actually consist of fine-scale intergrowths of daubreelite and MSS_1. This explains why it is difficult to obtain stoichiometric daubreelite analyses with EPMA. Table 4 gives representative analyses of MSS_1 and daubreelite obtained with the TEM. Our analysis of daubreelite has a Fe:Cr:S ratio of 1.19:2.05:4.0, which is close to stoichiometric daubreelite, which has a 1:2:4 ratio. Cr content is ~36 wt.%, Fe is ~22 wt.%, and S is ~43 wt.%. We found compositional variation within the MSS_1 phase, and therefore separated it into two categories: low V and high V (which range from ~0.5-2.5 wt.%, see below).

Dark-field STEM images from Sulfide 5 are shown in Figure 16. The thicknesses of the MSS_1 and daubreelite lamellae are variable. Nanometer-sized voids are scattered throughout some of the MSS_1 lamellae, but voids are not seen in the daubreelite phase (Figure 16a). Ni-rich inclusions are present around some of the voids in MSS_1 (Figure 16b). There is a great deal of strain in individual lamellae, which is especially apparent in the mottled texture of the MSS_1 phase (Figure 16c). As mentioned previously, some exsolved sulfides show daubreelite lamellae extending further into the surrounding metal than the MSS_1 lamellae (Figures 6c, 6g; 14a). This was also observed in TEM images (Figure 16d). An explanation for this feature is that the interfacial energy is lowest between daubreelite and metal when daubreelite extends further into the metal host phase. Nanometer-sized precipitates were also observed within the MSS_1 phase in high resolution TEM images, based on the contrast in the image (Figure 16e).

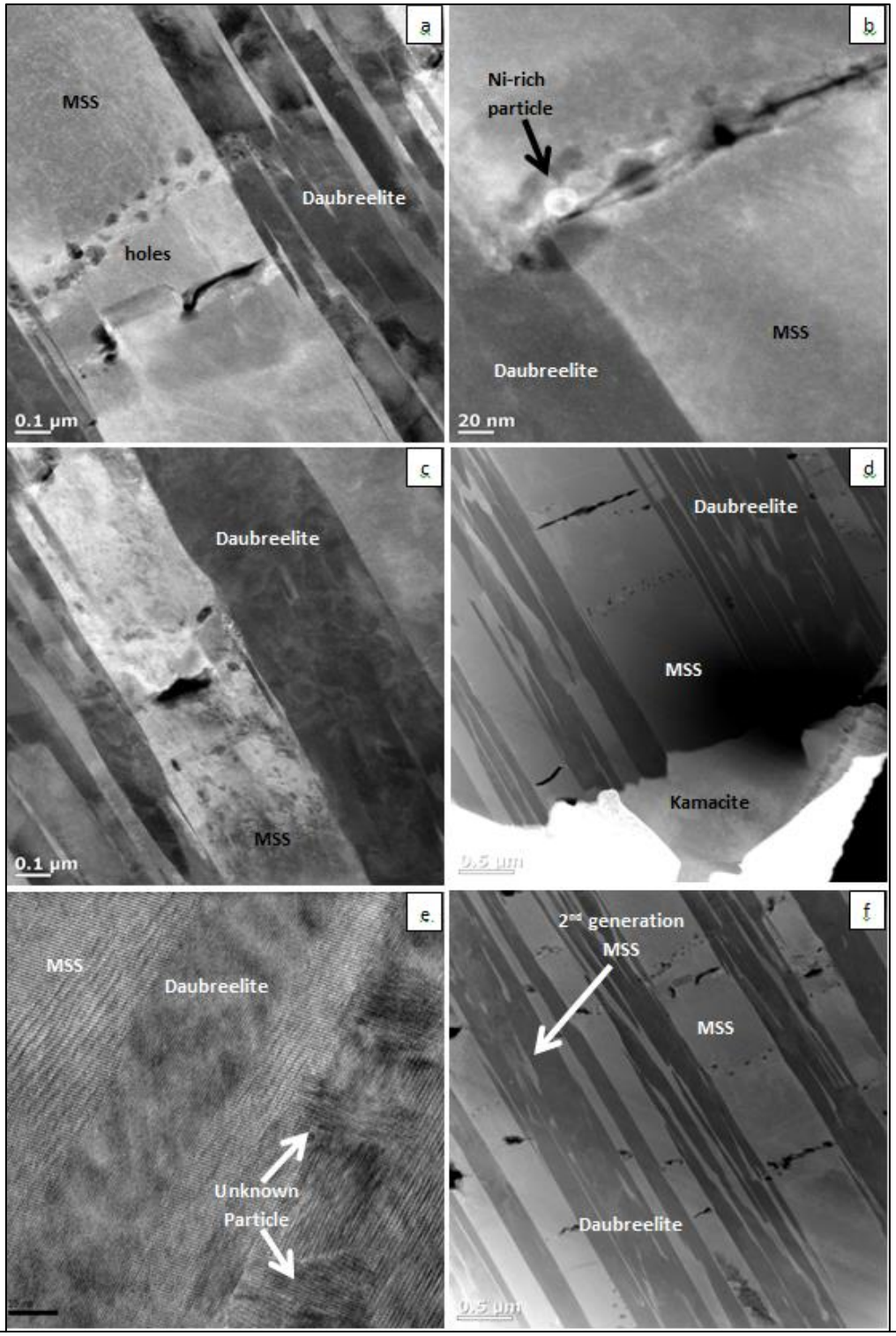

Figure 16. Dark field STEM (a-d, f) and bright field TEM (e) High resolution TEM lattice image of lamellae in exsolved Sulfide 5. Daubreelite lamellae are more complicated than they appear in BSE images shown previously. [a] Nanometer-sized voids are present in MSS_1; [b] Ni-rich particle in MSS_1 found near voids; [c] Strain in sulfides seen through mottled contrast. MSS_1 lamellae show a greater amount of strain than daubreelite lamellae; [d] Interface between sulfide and metal. Daubreelite lamellae extend further into the surrounding kamacite metal than MSS_1 lamellae; [e] Nanometer-sized particles in MSS_1 lamellae. Composition of particles is unknown; [f] Daubreelite lamellae showing a second generation of parallel lamellae, presumed to be MSS_1.

These particles also appear to lie in the plane of the FIB section. We were unable to resolve the composition of these precipitates, but they likely formed at very low temperatures because of their small size (~15 nm).

Dark-field STEM images show a second generation of parallel lamellae within the daubreelite lamellae (Figure 16f). Although we could not obtain analyses of this phase, we suggest that it is likely a later growth of MSS_1 from daubreelite. If this is the case, the initial daubreelite composition would have been slightly Fe-rich instead of strictly stoichiometric. Daubreelite would exsolve MSS_1 to get rid of its excess iron.

X-ray maps of an area ~2x2 μm within Sulfide 5 were obtained with the TEM in STEM mode (Figure 17). A dark-field STEM image is also included in Figure 17, where the dark grey phase is daubreelite and the light grey phase is MSS_1. MSS_1 has lower Cr and higher Fe, as expected. MSS_1 also has significantly higher vanadium contents. The V X-ray map shows differences in intensities within MSS_1, with a high V phase and a low V phase. High V tends to occur around the edges of the lamellae. Not much can be said of the differences in S between MSS_1 and daubreelite; the intensities are similar in both sulfide phases. The Ni X-ray map shows a slight enrichment of Ni in the MSS_1 phase compared to daubreelite. Nanometer-sized blebs of a Ni-rich phase are seen in the Ni X-ray map, and these all lie within the MSS_1 lamellae.

3.4 Mn, V, and Cr Relationships in Sulfides

Manganese, vanadium, and chromium contents of both exsolved and homogeneous sulfides are displayed in Figure 18. V and Cr contents were determined by both EPMA and TEM techniques. Manganese data could not be obtained using TEM

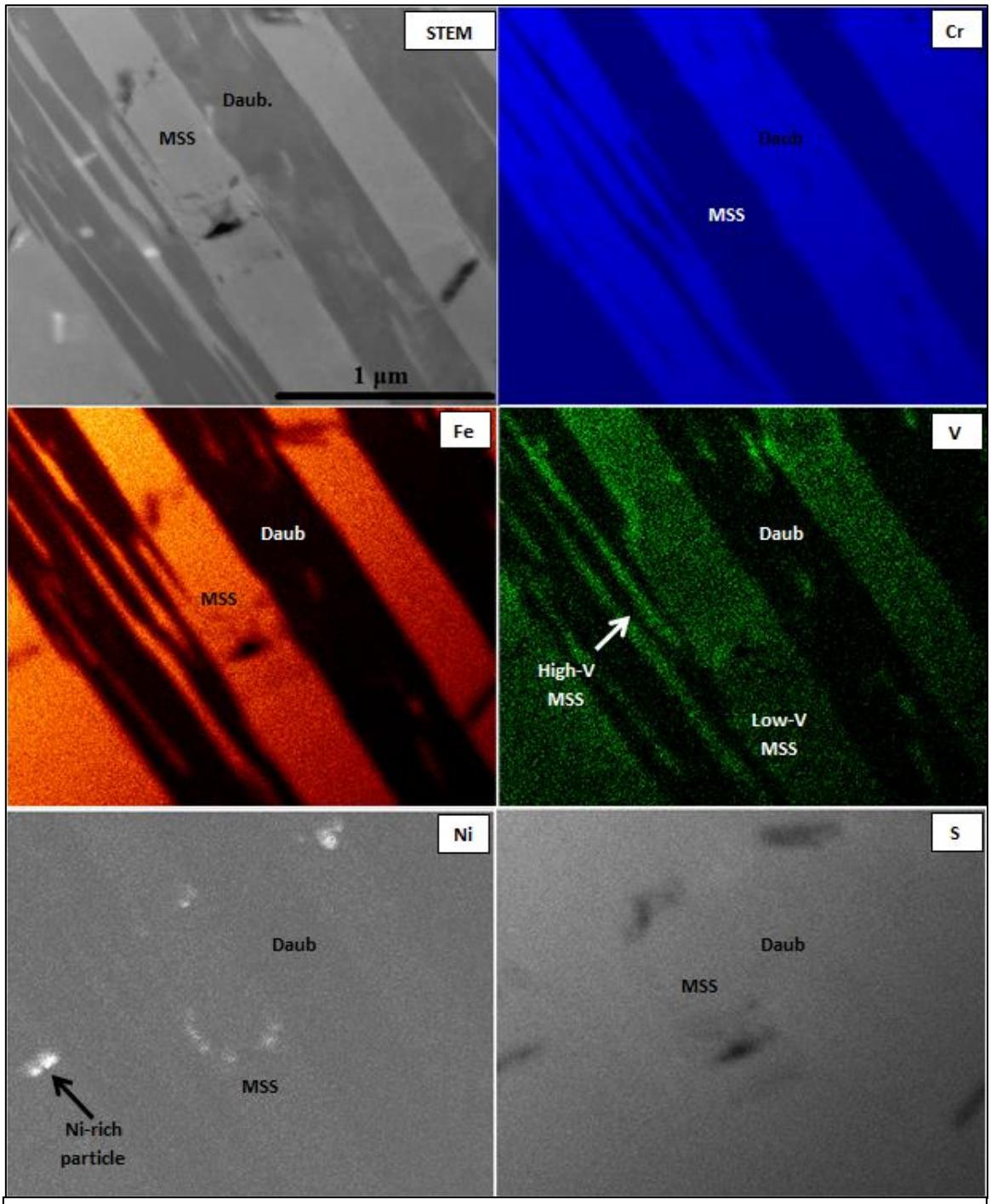

Figure 17. STEM X-ray maps from Gujba exsolved Sulfide 5 showing compositional differences between daubreelite and MSS_1 lamellae. The V map shows intensity differences between MSS_1 and daubreelite, with higher V in MSS_1. MSS_1 consists of higher V and lower V regions. The Ni map shows nanometer-sized Ni-rich blebs that mostly occur within MSS_1.

because the Mn Kα peak overlaps the Cr Kβ peak in the EDS spectrum. Since Cr has much higher concentrations than Mn in most of the sulfides analyzed, we are not able to deconvolve Mn peaks through the EDS software.

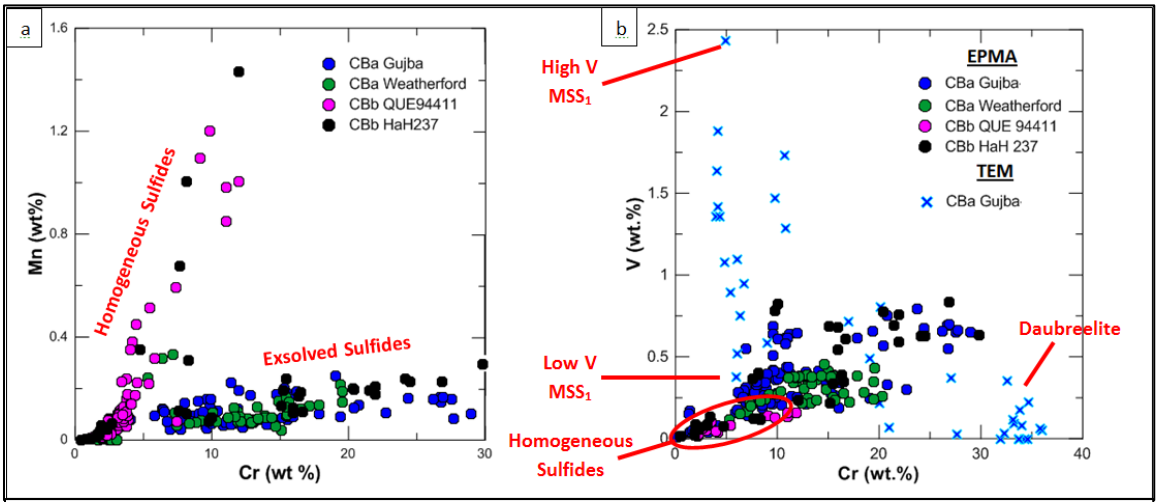

Figure 18. EPMA and TEM compositional data for sulfides in CB meteorites. [a] Mn vs. Cr (EPMA data only) graph shows different trends for homogeneous and exsolved sulfides. Homogeneous sulfides in CBb meteorites spread to higher Mn contents than those in CBa meteorites; [b] V vs. Cr graph showing analyses obtained with EPMA and TEM. Homogeneous sulfides contain little V. Gujba Sulfide 5 analyses from the TEM show two types of MSS_1: high V and low V. Most of the V is within the MSS_1 phase, and not within daubreelite. EPMA analyses are a mixture between one of the MSS_1 phases and daubreelite.

Homogeneous and exsolved sulfides show different trends on the Mn vs. Cr plot (Figure 18a). Homogeneous sulfides have lower Cr contents than exsolved sulfides, ~1-11 wt.%,but mostly <5 wt.%, and high Mn/Cr ratios. Manganese contents go up to 1.4 wt.% in the most Cr-rich homogeneous sulfides. CBb meteorites, QUE 94411 and HH 237, tend to have higher manganese and chromium contents in their homogeneous sulfides than the CBa meteorites. EPMA analyses of sulfides with daubreelite exsolution are a mixture of MSS_1 and daubreelite, and therefore show a larger spread in chromium. These sulfides have a lower Mn/Cr ratio than homogeneous sulfides, with manganese contents being slightly higher in daubreelite (~0.3 wt.%) than in MSS_1 (~0.1 wt.%).

Vanadium and Cr contents are shown in Figure 18b. EPMA analyses show that homogeneous sulfides have low V, while exsolved sulfides have higher V content. Based on the EPMA data alone, vanadium appears to be correlated with chromium in sulfides with daubreelite exsolution (Figure 15c). However, TEM analyses for Gujba Sulfide 5 show vanadium decreasing with increasing chromium. Daubreelite (~36 wt.% Cr) has little V, while MSS_1 has up to ~2.5 wt.% V. Differences between these two techniques are attributable to the spatial resolution of the analyses. BSE images obtained with the SEM show daubreelite lamellae are homogeneous in composition (Figure 15a), but dark field STEM images obtained with the TEM show daubreelite lamellae contain a second generation of MSS_1 lamellae. STEM V X-ray maps show the high-V MSS_1 phase is found at the daubreelite-MSS_1 interface (Figure 17), likely associated with the second generation of MSS_1. EPMA analyses (spot size = 1 μm) on daubreelite are therefore including this second generation of MSS_1, and appear to have a higher vanadium content. EPMA is therefore measuring mixtures of high-V MSS_1 with daubreelite, giving the apparent increasing trend in Figure 18b. On the other hand, the TEM is measuring analyses on individual lamellae within each sulfide. Our data indicate that low V MSS_1 has higher Cr content (~6 wt.%) and high V has lower Cr content (~4 wt.%). However, the vanadium content for Sulfide 5 is higher than in most exsolved sulfide inclusions. Some exsolved sulfides therefore might actually show a real positive correlation between V and Cr. It is hard to decipher the difference through EPMA, but further TEM analyses on other exsolved sulfides might be able to distinguish this.

4. Discussion

This discussion section first focuses on textural and compositional variations between the CBa and CBb meteorites to address the similarities and differences between the samples studied. We then discuss origins of CB metal and sulfides in the vapor plume scenario, and the impact-generated reheating events that occurred later on the CB parent body.

4.1 Textural and Compositional Comparison of CB Meteorites

CBa and CBb meteorites are texturally very different from one another (Figure 2). CBa meteorites have large, mm-to-cm-sized metal particles and chondrules. Gujba metal particles are primarily circular and elliptical in shape. This morphology suggests that they formed from melt droplets. Weatherford metal particles are long and elongated, and appear to be plastically deformed. CBa meteorites have appreciable amounts of impact melt interstitial to their metal and chondrule particles, and this is especially apparent in Weatherford. CBb meteorites are mainly composed of μm-to-mm-sized metal particles and chondrules. In the section we examined, HH 237 contains a few larger metal particles, similar to the shapes and sizes in CBa Gujba; however, they appear to be fragmented (Figure 2c). The section of QUE 94411 only contains small, μm-to-mm metal particles. HH 237 appears to be a combination of Gujba-like metal particles and QUE 94411-like metal particles. This observation supports the interpretation that CBa and CBb come from the same parent body.

Although each of the CBs we studied is texturally different, all four meteorites contain a high modal abundance of metal (40-50%, Table 2) and chemically similar

sulfides within the metal particles. Regardless of the size differences between CBa and CBb, homogeneous (unzoned) metal particles in both groups consist of kamacite (Fe,Ni) grains with ~93 wt.% Fe, ~6 wt.% Ni, and contain minor amounts of Co, P, and Cr (Table 4). CBb meteorites also contain some zoned metal particles [Weisberg et al., 2001; Krot et al., 2002], but these particles were not analyzed in this study. Some kamacite grains in each meteorite contain sulfides. Arcuate sulfides lie along metal grain boundaries [Rubin et al., 2003] (Figure 4a, 4b, 4d), and are typically homogeneous with low Cr content (≤5 wt.% Cr); however, a few appear to also contain a higher Cr phase (Figure 6h). Arcuate sulfide textures are more abundant in CBa meteorites than CBb meteorites, and are only found in large, mm-cm-sized metal particles. All four meteorites contain some kamacite grains with homogeneous sulfide inclusions (Figure 4d, 4e, 4f, 5a) composed of monosulfide solid solution, MSS_1 $(Fe,Cr)_{1-x}S$, with low Cr content (≤11 wt.%). Sulfide inclusions are more abundant and, on average, larger in CBa meteorites than CBb. Exsolved sulfide inclusions consist of a high Cr daubreelite ($FeCr_2S_4$) phase in a low Cr MSS_1 host [Weisberg et. al, 2001; Rubin et al., 2003] (Figure 6). We observed exsolved sulfides in all four meteorites, and found that they are more common in CBa meteorites than CBb. Only two metal particles in QUE 94411 display exsolved sulfides. Weisberg et al. (2001) observed silicate inclusions in metal particles in QUE 94411 and HH 237 in close association with sulfide inclusions. We found silicate inclusions in all four meteorites we studied. Metal blebs were also observed in Gujba, QUE 94411, and HH 237 in previous studies [Weisberg et al., 2001]. We observed metal blebs in both homogeneous and exsolved sulfide inclusions in all four meteorites (Figure 5b, 6g). Eutectic textures were also observed where sulfides and the surrounding metal have

melted and cooled to form a “fizzed” or dendritic texture (Figure 8). Eutectic sulfide-metal textures are more abundant in CBa meteorites, and located close to impact melt areas.

Homogeneous and exsolved sulfides have distinct compositions. Vanadium appears to partition preferentially into the MSS_1 phase over the daubreelite phase, which was seen from the STEM V X-ray map (Figure 17) and quantitative TEM analyses (Figure 18b). Exsolved Sulfide 5 from Gujba shows two types of MSS_1: low V and high V. High V MSS_1 was found on the edges of the MSS_1 lamellae (Figure 17). Manganese content tends to be higher in the homogeneous sulfides than in the exsolved sulfides (Figure 18a). Homogeneous sulfides have higher Mn/Cr ratios than exsolved sulfides. CBb meteorites, which consist of smaller metal grains, also have a higher amount of Mn in their homogeneous sulfides than CBa meteorites, which consist of larger metal grains. Hence, smaller grains have both higher Mn (Figure 18a) and S content (Figure 9), which could indicate a faster cooling rate for these grains.

Despite obvious differences in sizes and morphologies of the metal particles, the similarities in metal and sulfide compositions between these four meteorites suggest that they not only have similar origins, but that they have also experienced similar secondary processes. In the next section, we use these observations to provide further insights into the thermal history and formation conditions of CB meteorites.

4.2 Origin of CB Meteorites

Oxygen isotopes indicate that different types of CB meteorites have related origins, and are also closely related to the metal-rich CH chondrites. Oxygen isotopic

compositions for CBa Gujba and Weatherford, and CBb HH 237 and QUE 94411 all fall just under the CR-mixing line on an oxygen 3-isotope diagram (Figure 1b), close to where the CHs and CRs lie [Clayton and Mayeda, 1999; Weisberg et al., 1995; 2001; Krot et al., 2002]. These three groups are different from the other carbonaceous chondrites, which generally lie along the carbonaceous chondrite anhydrous minerals (CCAM) line. Oxygen isotopes indicate that CB-CR-CH meteorites formed in the same isotopic reservoir. Furthermore, similarities in compositions between CB and CH chondrites indicate that they might have come from the same parent body.

The formerly leading idea for CB formation is condensation of metal and silicate particles in the primitive solar nebula. Evidence for the nebular model comes from compositions of unzoned metal in CB meteorites, which plot along the solar Co-Ni ratio [Newsom and Drake, 1979; Weisberg et al., 2001; Krot et al., 2002]. The presence of zoned metal grains in CBb meteorites also indicates formation at high temperatures in a rapidly cooling nebular gas [Meibom et al., 2000; Petaev et al., 2001; Weisberg et al., 2001; Campbell et al., 2005b]. However, there are many problems pertaining to this model due to the gas composition and pressures required for formation of CB components. CB meteorites contain >40 vol.% metal, which is higher than any other chondrite group [Weisberg et al., 2001]. If these meteorites formed by condensation, condensation of metal would require extremely high partial pressures, and gas would have to be enriched in siderophile elements by a factor of ~10^7 x solar [Campbell et al., 2002]. These two requirements for CB material are not consistent with formation from a gas of solar composition under canonical conditions.

The current leading model for CB formation is condensation from a post-nebular impact-generated vapor plume. In the vapor plume model, a collision between a metal-rich body and a silicate-rich body could produce a dense vapor plume highly enriched in siderophile elements (Figure 19a,b) [Wasson and Kallemeyn, 1990; Kallemeyn et al., 2001; Campbell et al., 2002; Rubin et al., 2003; Fedkin et al., 2013]. The enrichment in siderophile elements in the plume from the metal-rich impactor would allow for a high abundance of metal to condense. The plume must have been a reducing environment. Under oxidizing conditions, iron would condense into silicates, but the high abundance of metal and low FeO contents in silicates suggests formation under reduced conditions, but less reduced than enstatite chondrites [Ebel, 2006; Fedkin and Grossman, 2006].

Based on the textures of CB components, chondrules and metal could have formed in various ways in the plume scenario. Most chondrules in CBs are cryptocrystalline and nonporphyritic barred olivine [Weisberg et al., 2001]. This is unusual compared to the other carbonaceous chondrite groups, where these two types of chondrules are a minority and most chondrules are porphyritic [Scott, 2007]. The high temperatures created by the large-scale impact could form melt droplets of unzoned metal and olivine chondrules from surficial material [Campbell et al., 2002; Rubin et al., 2003; Krot et al., 2005; Davidson et al., 2010; Fedkin et al., 2013] (Figure 19b). The idea of unzoned metal and olivine chondrules forming as melt droplets is especially apparent from CBa Gujba components; particles are mostly spherical and rounded in shape. Temperatures and pressures in the vapor plume must also be heterogeneous to form the different components. Krot et al. (2005) suggests that cryptocrystalline chondrules in CBb HH 237 formed by gas-liquid condensation in the plume. Fedkin et al. (2013)

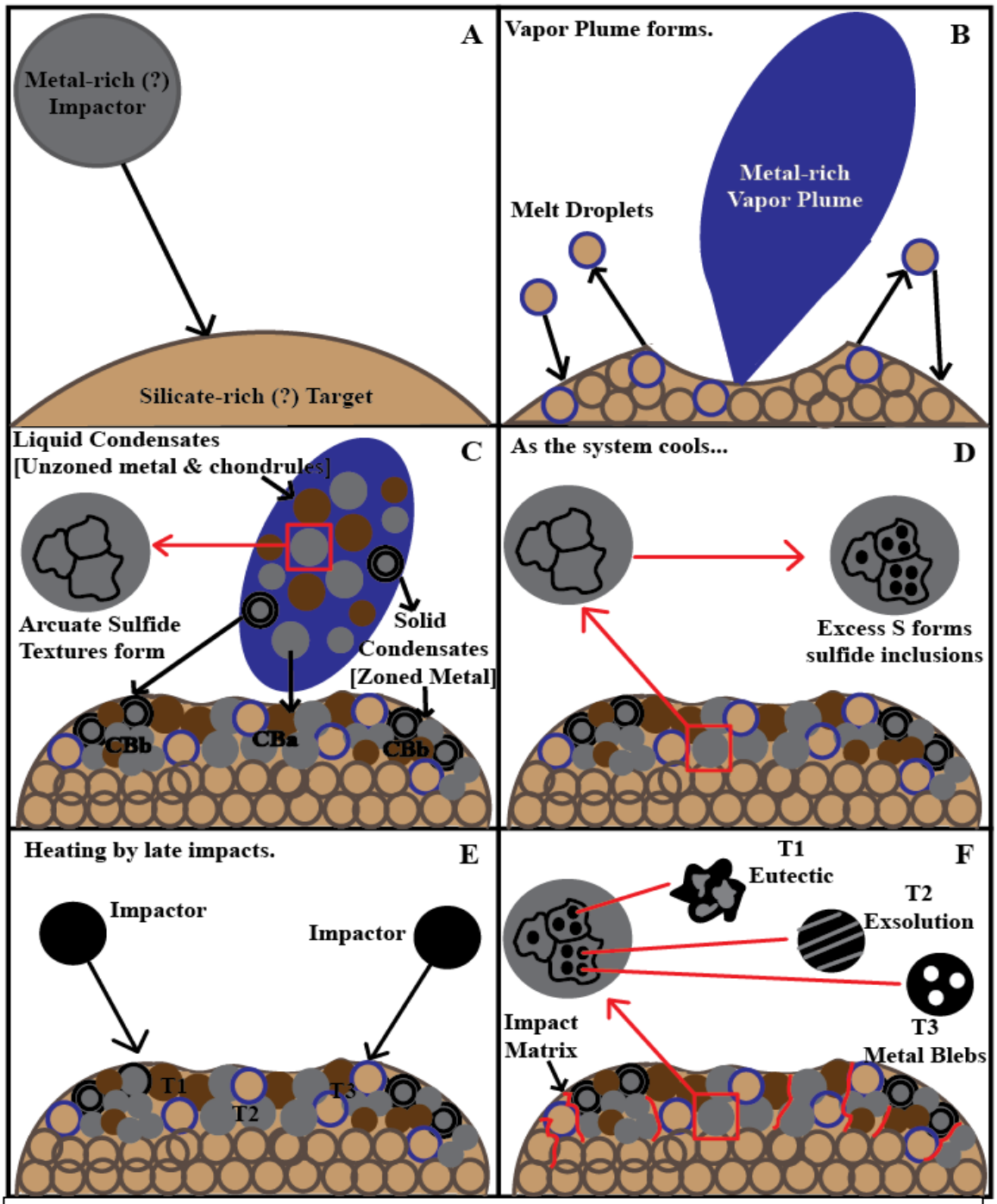

Figure 19. Illustration depicting the formation of CB material. [a] A metal-rich body and a silicate-rich body collide; [b] A metal-rich vapor plume forms from the collision. Melt droplets are ejected from the body; [c] Metal and silicate condensates form in the dense vapor plume as gas-liquid condensates in a region of high pressure. Metal begins crystallizing, and S-rich metal melt crystallizes arcuate sulfide textures along metal grain boundaries, and solidifies before falling to the parent body. Zoned metal grains form as gas-solid condensates in a region of high temperature. CBa components fall closer to impact site, and CBb fall farther away; [d] As the system cools, solidified metal (some containing arcuate sulfides) with excess sulfur precipitates small sulfide inclusions; [e] Later impacts cause heterogeneous heating on the CB parent body; [f] Depending on composition and temperature, sulfides either reach the eutectic and melt, are exsolved if they contain high Cr, or form metal blebs if they contain high Fe,Ni. Impact melt is found interstitial to metal and silicate material.

modeled the vapor plume scenario and suggested that if unzoned metal condensed as liquids, the pressure in this region of the plume was $10^{-2} – 10^{-3}$ bar. The presence of zoned metal in CBb meteorites implies formation in a different region of the vapor plume [Rubin et al., 2003]. Krot et al. (2005) suggested that zoned metal in HH 237 formed by gas-solid condensation in the plume. Zoned metal requires higher temperatures than unzoned metal, evidenced by their zoning patterns, and likely formed in a region of lower pressure, $10^{-5} – 10^{-8}$ bar [Fedkin et al., 2013]. In addition to forming in different regions of the plume, the size variations between CBa and CBb meteorites also indicate particles in both groups were likely deposited differently. Rubin et al. (2003) suggested that metal and chondrules were sorted during deposition based on settling velocities and density of grains. CBa material might represent an earlier depositional component, since these meteorites consist of coarser grains compared to the CBb meteorites [Rubin et al., 2003]. If CBa and CBb material condensed in different regions of the plume, we suggest that CBa and CBb material fell back onto the parent body in different areas as well. Larger particles, found in CBa meteorites, fall closer to where the impact originated. Smaller particles and zoned grains, found in CBb meteorites, fall farther from the impact area. HH 237 is an example of an intermediate region, since it contains some large, CBa-like metal particles, as well as small, CBb-like metal particles. Because of the high temperatures at the surface, matrix material melts and is injected among the plume fallout material (Figure 19c).

The young ages of chondrules in CBs also provide evidence of a post-nebula impact origin. Chondrules from CBa Gujba give Pb-Pb formation ages of 4562.7 ± 0.5 Ma, and chondrules from CBb HH 237 have Pb-Pb ages of 4562.8 ± 0.5 Ma [Krot et al.,

2004; 2005]. Pb-Pb dating on CV chondrules show ages of 4567.2 ± 0.6 Ma [Amelin et al., 2002; 2004], which is ~ 5 million years before CB chondrules. Some chondrules in CBa Weatherford have Ar-Ar ages of 4.5 Ga [Kelly and Turner, 1987], and some in CBa Gujba have Pb-Pb ages of 4545.4 ± 3.9 Ma [Krot et al., 2004; 2005; Amelin and Krot, 2005]. The younger aged chondrules might indicate a resetting event that occurred after the original formation of chondrules in CBs (Figure 19e). Given the relatively young ages of all CB chondrules, formation of CBs possibly postdates the lifetime of the solar nebula [Amelin and Krot, 2005; Krot et al., 2005]. Overall, chondrules in CB chondrites likely formed through a different mechanism than chondrules in the other chondrites because of their textures and young ages, and this mechanism is most likely impact-related.

4.3 Formation of Sulfide Inclusions

Many ideas have been proposed to explain the presence of sulfides in some unzoned metal particles. Weisberg et al. (2001) suggested sulfide formation could occur if metal particles were porous initially and reacted with surrounding H_2S gas at lower temperatures to form troilite. However, studies on primitive ordinary chondrites by Lauretta et al., (1996) show that this process would have resulted in an outer shell of sulfide around an inner shell of slightly different composition. Neither of these compositions are seen in CB meteorites [Lauretta et al., 1996; 2001; Campbell et al., 2005b]. Rubin et al. (2003) suggested metal could have been evaporative residues that melted and boiled. Metal that was rapidly removed from heat retained higher concentrations of S, allowing for later precipitation of sulfides.

We believe sulfides that occur in CBs likely formed as a result of crystallization and subsequent processing of what was initially a sulfur-rich Fe,Ni metal melt. Sulfide

inclusions are only observed in unzoned metal grains [Campbell et al., 2005b]. Variations in temperature, pressure, and cooling rates can control the sulfur content in metal. We assume that S solubility decreases with temperature. Fe-Ni-S melts could have formed either by gas-liquid condensation in an impact plume (Figure 19c) or as a melt droplets that were formed and ejected during the collision (Figure 19b). Rubin et al. (2003) suggested that as some kamacite (Fe,Ni) metal grains crystallize, they allow S to partition into the melt phase and enrich the residual melt. As the system cools further, sulfur from the residual melt begins to crystallize as MSS_1. Sulfides solidify along metal grain boundaries as arcuate sulfide textures, consistent with immiscible S-metal melt. Our observations of arcuate sulfides indicate that these textures must have crystallized from the metal melt before the particles fell back onto the CB parent body. This is especially apparent in arcuate textures from CBa Gujba, where metal grains are mainly rounded (Figure 4a). The metal and arcuate sulfides must be solid by the time they land on the surface in order to preserve their morphologies and textures (Figure 19d). Rubin et al. (2003) also suggested that some metal grains in CBs crystallized rapidly and incorporated more S. As the system cooled further, small sulfide inclusions precipitated from the metal [Rubin et al., 2003]. We also observed grains that contain both arcuate sulfides and sulfide inclusions (Figures 4b,d; 5a). We suggest that sulfide inclusions precipitated later from excess S in solidified metal, indicating that there was a minor abundance of S still present in the metal after the grains crystallized at lower temperatures. In this case, a disproportionation reaction occurs: S^0, Fe^0, and Cr^0 in the metal phase change valences and precipitate as S^{2-}, Fe^{2+}, and Cr^{2+} in the sulfides. Because the solubility of S in metal decreases with temperature, S will precipitate to form the small sulfide inclusions in the

same grains as arcuate sulfides (Figure 19d). Our work shows that the range of modal abundances for fine-grained and coarse-grained sulfide inclusions is similar for all four meteorites (~0.5-7.5 wt.%, Figure 9, Table 3). Metal grains that contain sulfides possibly cooled at different rates, and the textures of the sulfides are reflecting these different cooling rates. Coarse-grained inclusions cooled more slowly than fine-grained inclusions. The slower cooling rate allows for inclusions to grow larger in size.

Although the modal abundances of sulfides was generally similar for all grains, there was a slight distinction in sulfide content between small and large metal grains. Smaller metal grains, mainly seen in CBb meteorites, showed slightly higher sulfide modal abundances than the larger grains of the CBa meteorites (Figure 9). The modal abundances of sulfide inclusions reflect the primary bulk S contents of the metal grains. The primary sulfur content can also reflect the maximum temperature that metal melts reached. At higher temperatures, more sulfur is lost due to volatilization. The grain size of individual sulfide inclusions can either be attributed to cooling rate and/or Ostwald ripening. As the sulfides are precipitating out of the solid metal phase, over time, energetic factors will cause large precipitates to grow and smaller precipitates to shrink. Large particles have a lower surface to volume ratio, resulting in a more favorable lower energetic state [Yao et al., 1993]. The size of the sulfide inclusions observed in the metal grains denotes this thermodynamically-driven process.

The presence of V and Mn in sulfide inclusions can potentially put constraints on the formation of metal grains. We observed that sulfides in CBs contain ≤ 10 wt.% bulk Cr, and minor amounts of Mn and V (Figure 18). Unlike Ni and Cr, which have condensate preferentially by dissolving into Fe alloys in a canonical nebula, Mn and V

partition into silicates and oxides at high temperatures [Lodders and Fegley, 1998]. Vanadium, a refractory lithophile element, has a 50% condensation temperature of 1455 K in a gas of solar composition, and condenses into $CaTiO_3$ [Kornacki and Fegley, 1984; Lodders, 2003]. Manganese, a moderately volatile element, has a 50% condensation temperature of 1190 K in a gas of solar composition and condenses into olivine as Mn_2SiO_4 [Wai and Wasson, 1977]. However, if sulfides formed by precipitation from metal in the solid state, these minor elements must have been present in the metal before partitioning into the sulfides. Calculated condensation of Fe sulfides from a gas of solar composition begins at ~700 K [Grossman, 1972; Lauretta et al., 1996]. Vanadium and manganese would have to be present in the metal phase until the system cooled to this temperature, which is unlikely to occur. These two elements would likely have partitioned out of the metal phase by the time the system cooled to lower temperatures. Because Mn and V tend not to be siderophile elements, neither is likely to go into the metal unless conditions were very reducing. The presence of these two elements in the sulfide inclusions provides evidence against condensation of metal as either solid or melt in a canonical solar nebula.

Some sulfide inclusions show exsolution, and we interpret this as evidence of reheating episodes. Observations of other components (as discussed below) lead us to believe this sulfide texture formed from impact heating and subsequent rapid cooling. Later impacts on the CB parent body, indicated by Marty et al. (2010), Weisberg et al. (2010), and Goldstein et al. (2011), would have caused heterogeneous heating within the CB parent body (Figure 19e). Sulfide inclusions that had previously precipitated from metal could then have been reheated to a point where they unmixed and exsolved a Cr-

rich phase (Figure 19f). An alternative scenario is that sulfide inclusions could have precipitated and exsolved during a single reheating event, with exsolution taking place during cooling. All four CB meteorites show the same exsolution textures in their sulfide inclusions, which indicates they all experienced the same process. CBa meteorites contain a higher abundance of exsolved sulfides than the CBb meteorites, suggesting that more material in the CBa's was reheated, possibly because they were closer to the impact site. CBa sulfides also have higher bulk Cr than CBb sulfides, possibly allowing for the greater quantity of exsolution we observe in CBa meteorites.

Silicate inclusions observed in some metal grains are also found in close proximity to sulfide inclusions (Figure 12). We believe these inclusions could have formed if two molten particles, one metal and one silicate, collided, resulting in an immiscible silicate liquid and a metal liquid. This silicate liquid could also account for other necessary lithophile elements, such as Mg, Al, and Ca.

4.4 Evidence of Later Impacts

Multiple observations from CB components provide evidence of thermal episodes that are most likely caused by impact. CB interstitial matrix consists of impact melt. CBs only contain ~5 vol.% matrix (Table 1), which is lower than all other chondrite groups [Scott, 2007]. The presence of melt matrix is due to melting during impact events [Ramdohr, 1973; Newsom & Drake, 1979; Weisberg et al., 2001]. There are larger areas of impact melt in CBa meteorites than in CBb meteorites, which is especially seen in CBa Weatherford (Figure 2). Glass from impact melt areas in CBa Bencubbin has Ar-Ar ages of 4.20 ± 0.05 Ga [Marty et al., 2010], and glass from CBa Weatherford has Ar-Ar ages

of 3.6 Ga [Kelly & Turner, 1987]. Differences in ages indicate multiple impact events that occurred after initial accretion of CB material.

Several of our observations support late impacts. Some sulfide inclusions in metal particles show evidence of melting. This process must have occurred after sulfide inclusions already precipitated from the metal. These sulfide-metal textures appear "fizzed" and are typically found near impact melt areas (Figure 8). These textures indicate that the grains have been heated to at least the Fe-Ni-S eutectic, 950°C, and then cooled rapidly at 10^5 °C/sec [Scott, 1982; Chappell et al., 2011]. We observed this texture in all four CB meteorites; however, it is much more common in CBa than in CBb. CBs also have some metal grains with two-phase microstructures of taenite and kamacite which show heating to ~675°C, and subsequent cooling to ~550°C in a month or less [Goldstein et al., 2011]. The two temperatures above indicate heterogeneous heating of CB metal and sulfides.

All four meteorites we studied also show plastic deformation in some of their sulfide inclusions, metal particles, and chondrules. Several papers have discussed deformation as a result of secondary, later impact events [Weisberg et al., 2002; 2004; 2010; Meibom et al., 2005], for example deformation of barred olivine chondrules in CBa Gujba [Weisberg et al., 2002]. Chondrules are shown to be primary materials that were later plastically deformed by multiple impact heating events. Of the four CB meteorites we studied, CBa Weatherford appears to have undergone the greatest degree of deformation (Figure 2b). Many metal particles in this meteorite are elongated and irregular in shape, especially near areas closest to impact melt, which is unlike the nearly-round metal particles in CBa Gujba (Figure 2a). Our observations provide additional

evidence for deformation. In some cases, the metal particles as well as the sulfides within them show plastic deformation (Figure 7). Since the sulfide inclusions in the deformed metal curve in the same direction and manner, deformation must have occurred after these particular sulfide inclusions formed. We also observe deformation in exsolved sulfides, indicating that deformation of the lamellae occurred after the sulfides exsolved (Figure 7b). This provides evidence of multiple episodes of impact heating.

4.5 Interpretation of Sulfide Textures

The sulfide textures we observe could have formed by impacts in multiple heating stages.. We suggest that later impacts caused multiple stages of reheating of CB material, resulting in exsolution in sulfides that have high bulk Cr content (Figure 20a). In this multiple-stage impact scenario, metal particles form in the vapor plume as liquid condensates, and rapidly cool. Arcuate sulfide textures crystallize around metal grain boundaries before emplacement on the parent body. An impact on the parent body causes reheating of solid metal, precipitating homogeneous sulfide inclusions, and subsequently cooling rapidly. The cooling rates during initial formation of sulfide inclusions were likely too fast to allow exsolution to occur. Another stage of reheating occurs, and sulfides cool a bit slower to allow exsolution. Reheating to high temperatures, >950°C, cause sulfide inclusions and surrounding metal to melt, creating Fe-Ni-S eutectic textures. This is followed by a greater degree of rapid cooling to preserve the “fizzed” textures. The final reheating episode causes metal and sulfide inclusions to plastically deform. In an alternative scenario, exsolved sulfides could have formed in a single-stage impact event (Figure 20b). In this scenario, metal particles and arcuate textures form in a likewise manner as above. An impact on the parent body causes reheating of solid metal,

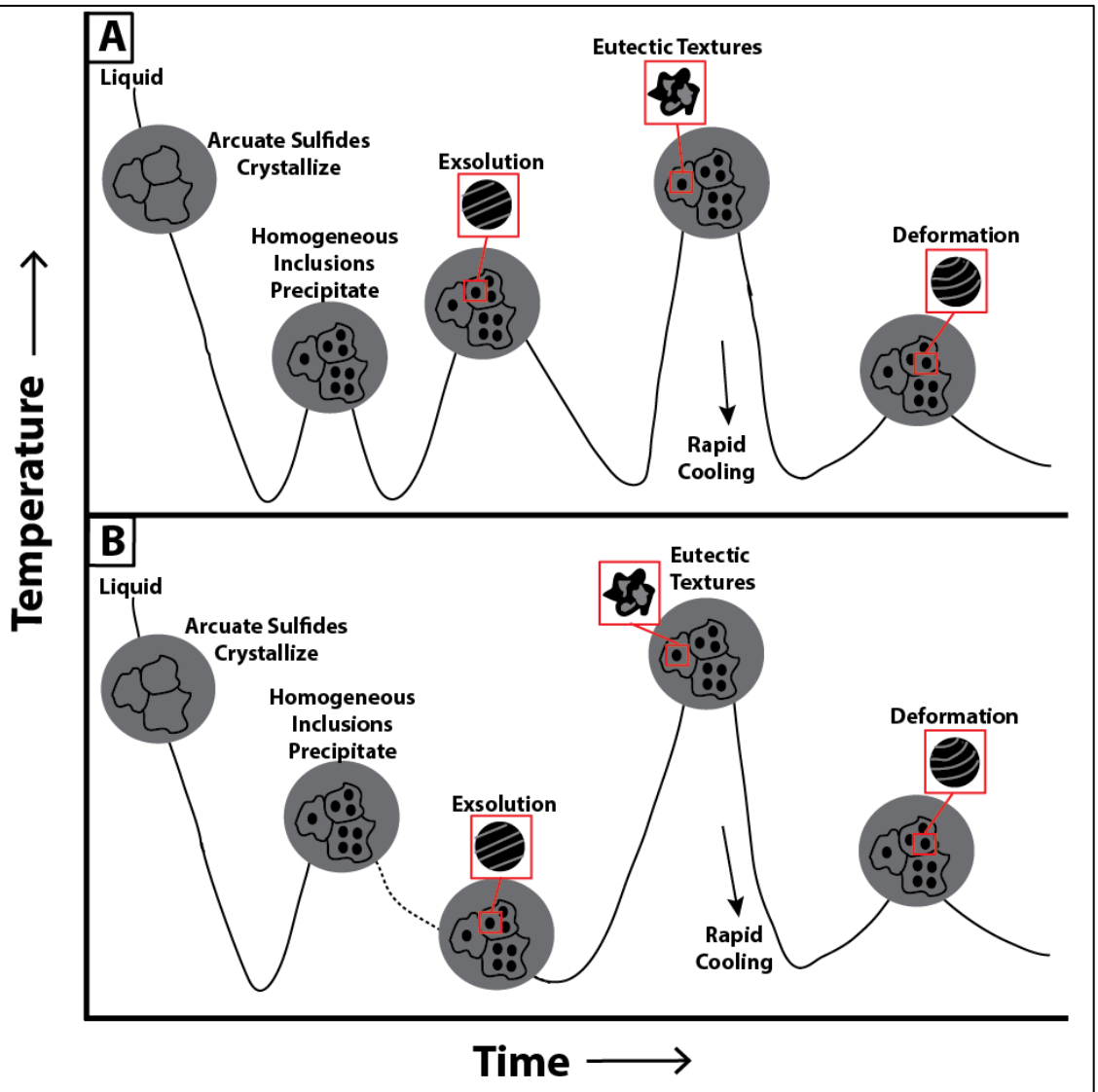

Figure 20. Thermal history diagrams for sulfide formation in CB meteorites. In both scenarios, A and B, metal particles form in a vapor plume as liquid condensates, and as they cool, arcuate sulfide textures crystallize around metal grain boundaries. [a] Sulfide inclusions form from a multiple-stage impact scenario. A reheating event causes homogeneous sulfides to precipitate out of solid metal. Inclusions cool too rapidly to allow exsolution to occur. A second stage of impacts cause reheating of sulfide inclusions, and slow cooling allows sulfides with high bulk Cr to exsolve. Later episodes of impacts cause melting (temperatures >950°C) of some sulfides and surrounding metal, creating Fe-Ni-S eutectic textures that subsequently rapidly cool, as well as plastically deforming some particles. [b] Sulfide precipitation and exsolution result from a single-stage impact. A reheating event causes homogeneous sulfides to precipitate out of solid metal. Inclusions cool slowly enough to allow exsolution to occur. Eutectic textures and deformation are caused by later impacts in a similar manner to [a].

and homogeneous sulfide inclusions precipitate from solid metal. During cooling, those that have high bulk Cr will exsolve. Eutectic Fe-Ni-S textures form from high

temperature reheating and rapid cooling after the precipitation of sulfide inclusions. Finally, late stage impacts causes metal and sulfide inclusions to deform.

Assuming the multiple-stage impact scenario, Fe-Cr-S phase diagrams from El Goresy and Kullerud (1969) (Figure 3) allows constraints to be made on the maximum reheating temperature exsolved sulfides have experienced. Figure 21 shows the 700°C and 600°C phase diagrams of El Goresy and Kullerud (1969) that have been simplified to only show the relevant phases of this study. At 700°C, tie lines exist between MSS_1 and MSS_2, and daubreelite cannot coexist with Fe metal, which is also Cr-rich (Figure 21a). The three-phase region we observe in our four CB samples is plotted on the phase diagram, and clearly shows that the assemblage MSS_1 + daubreelite + Fe metal is inconsistent with 700°C phase relationships. At lower temperatures, the MSS_1-MSS_2 join

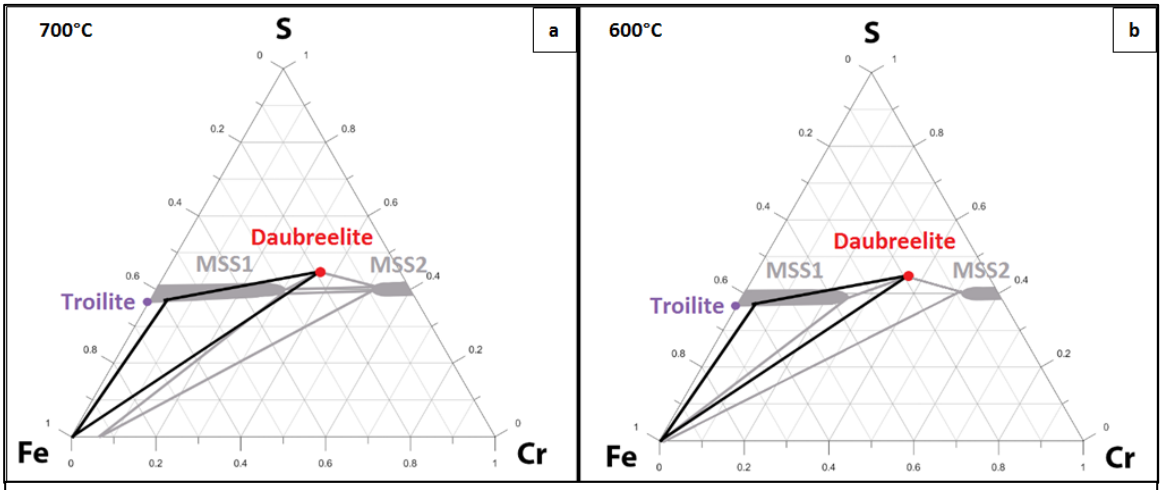

Figure 21. Simplified Fe-Cr-S phase diagrams from El Goresy and Kullerud (1969) (see also Figure 2). [a] At 700°C, daubreelite is not stable with Fe metal. The three-phase triangle from CB meteorites (black) does not fit with the stable equilibrium assemblages at this temperature. [b] At 600°C, daubreelite is now stable with MSS_1 and Fe metal, but the three phase triangle from CB meteorites is still very different from the stable assemblage at this temperature: MSS_1 has much lower Cr content. CBs have been reheated to maximum temperatures <<600°C.

is no longer stable, and at 600°C the three-phase region between MSS_1, daubreelite, and Fe metal exists (Figure 21b). Iron metal at this temperature is Cr-poor. These are the

three phases we see in CB meteorites, so we must be seeing an assemblage that equilibrated at <700°C. However, the three-phase triangle observed in CBs is very different from compositions stable at 600°C. In exsolved sulfides in CBs, MSS_1 has much lower Cr than we would expect at 600°C. Comparing the 700°C and 600°C phase diagrams, the MSS_1 solid solution field has lower solubility of Cr as temperature decreases. At lower temperatures, we would expect to see the same trend – MSS_1 in equilibrium with daubreelite should continue to become less Cr-rich. We therefore conclude that exsolved sulfides in CBs have been reheated to maximum temperatures <<600°C. If we consider the alternative model for formation of exsolved sulfides, in which exsolution occurs upon cooling in the same heating event that formed the sulfide inclusions (scenario B in Figure 21), then the temperature recorded by exsolved sulfides, <<600°C, would be interpreted as the closure temperature of the system.

Because of their low bulk Cr content, homogeneous sulfides did not exsolve when reheated. CBb QUE 94411 shows homogeneous sulfides with higher Cr content (<11 wt.%) than the other three CBs (Figure 14d). Since these sulfides did not exsolve, they were likely heated to higher temperatures than the other homogeneous sulfides. Homogeneous sulfides also contain higher Mn content than exsolved sulfides, which might be stabilizing the sulfides at higher temperatures.

After CB sulfides were reheated, they must have subsequently cooled rapidly. Evidence for this is observed from the daubreelite lamellae in the exsolved sulfide inclusions. Daubreelite lamellae are very fine in scale, and range between a few hundred nanometers to ~2 μm (Figure 6c-d; 16). TEM analysis also shows a second-generation of MSS_1 lamellae within the daubreelite lamellae (Figure 16f), nanometer-sized Ni-rich

particles (Figure 16b), as well as an unknown nanometer-size phase (Figure 16e) in the MSS_1 lamellae. If particles cooled more slowly, the size of the metal blebs and the thicknesses of lamellae would be larger and coarser-grained. The presence of these fine grained particles indicates cooling at a rapid rate after a low temperature heating event. We suggest that this is consistent with heating resulting from an impact.

5. Conclusion

Although they are texturally different, all four CB meteorites we studied have very similar metal and sulfide compositions. Multiple studies have shown that CB components form from an impact-generated vapor plume, either as melt droplets, gas-liquid condensates, or gas-solid condensates. We observed that Gujba, Weatherford, HH 237, and QUE 94411 all contain homogeneous and exsolved sulfide inclusions within some kamacite grains. The differences in sizes of metal and chondrule components between CBa and CBb meteorites indicate they formed in various regions of the vapor plume (differing in temperature and pressure), and fell back onto distinct regions on the parent body. We interpret that CBa meteorites, which consist of large mm-to-cm-sized particles, fell close to the impact site, and CBb, which consists of small μm-to-mm-sized particles, traveled greater distances from the impact site. HH 237, which contains both large and small metal grains, likely accreted in an area between CBa and CBb regions. Smaller metal particles might also have cooled more quickly than larger particles. All four meteorites also contain homogeneous sulfide inclusions found in unzoned metal. This unzoned metal likely formed as either a gas-liquid condensate, or by impact splashing on melt droplets. Arcuate textures formed from residual S-rich melt as metal crystallized, and particles containing arcuate textures must have solidified before falling

onto the parent body in order to preserve the elliptical/rounded morphologies of the metal particles. Sulfide inclusions later formed from excess S in the solid metal phase. All four meteorites also have exsolved sulfides and sulfide inclusions containing nanometer-sized metal blebs, indicating they experienced similar secondary heating processes. Our detailed analysis of exsolved sulfide inclusions suggest that CBs have been reheated to <<600°C. The fine-grained sizes of inclusions and lamellae indicate sulfides must have cooled rapidly. TEM analyses on an exsolved sulfide from CBa Gujba show multiple stages of exsolution as the grains cooled.

After formation of CB components in an impact plume, the CB parent body experienced multiple impact events that caused heterogeneous heating of CB material. Evidence for the impact(s) is seen through exsolution in sulfides [this study], Fe-Ni-S eutectic textures [this study; Chappell et al., 2010], two-phase microstructures of taenite-kamacite [Goldstein et al., 2011], impact melt areas [Weisberg et al., 2001; Meibom et al., 2005], deformation (of sulfide inclusions, metal particles, and chondrules) [this study; Weisberg et al., 2002], and high pressure phases [Weisberg et al., 2004; 2010].

Appendices

Appendix A – BSE Images and X-ray Maps

This appendix contains additional BSE images obtained from the scanning electron microscope and X-ray maps obtained from the electron microprobe.

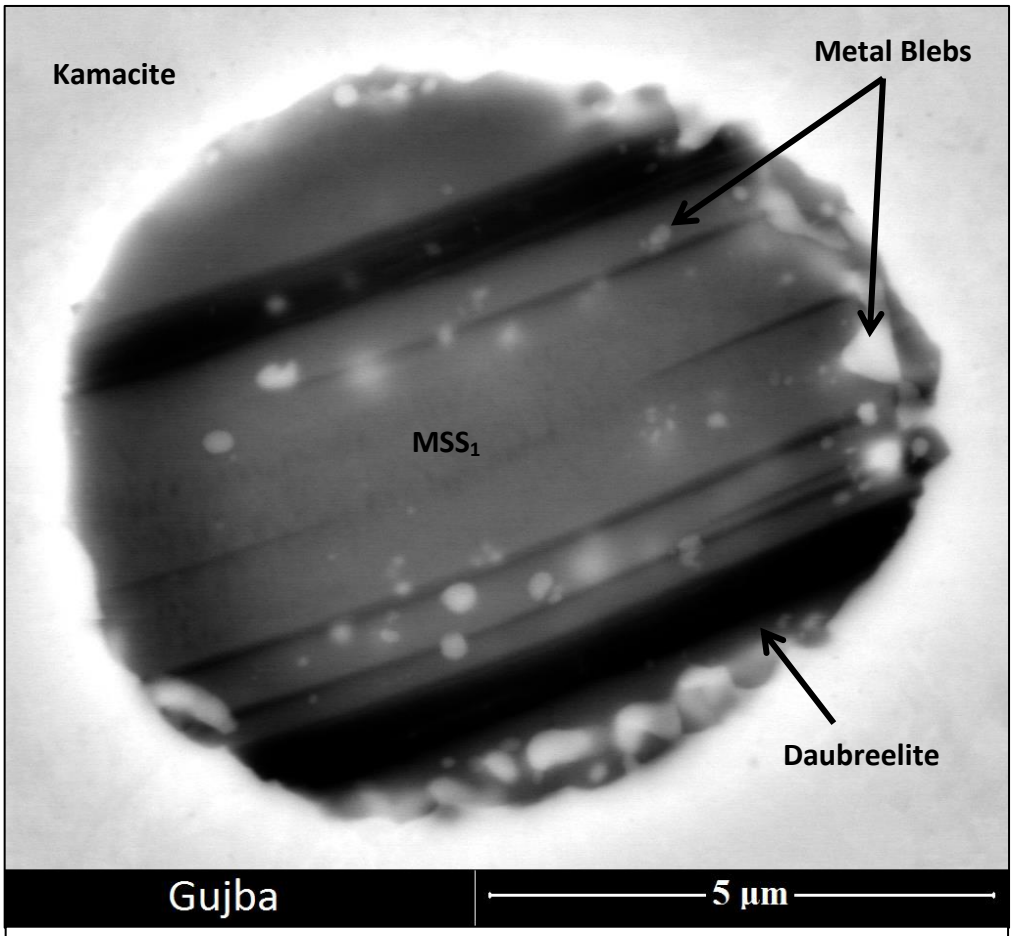

Figure A-1. Metal blebs in an exsolved sulfide inclusion from CBa Gujba. Blebs are located in the outer regions of the sulfide inclusion, compared to other sulfides that have blebs only located in the cores of the sulfide inclusions (Figures 5b, 6g).

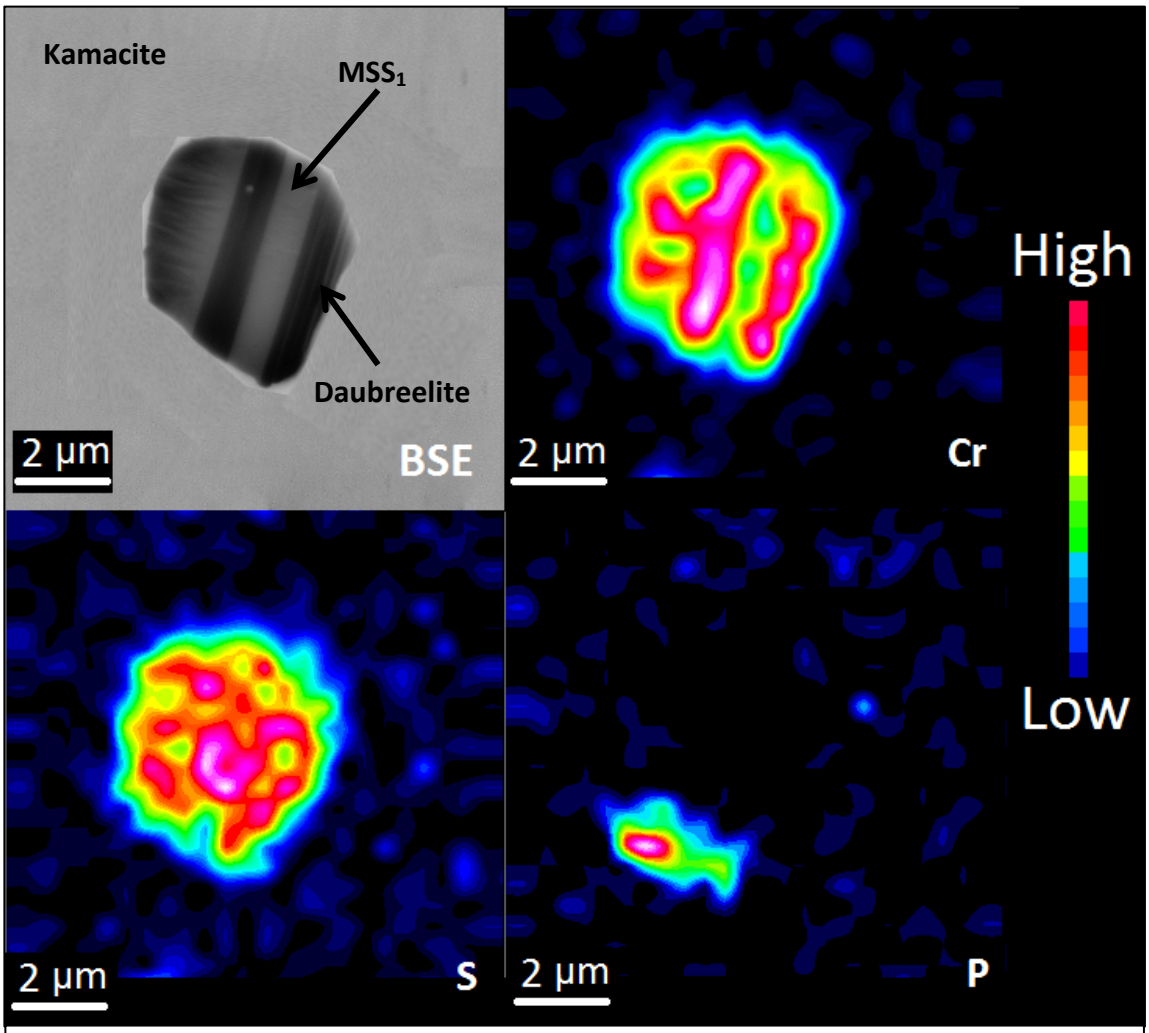

Figure A-2. EPMA X-ray maps of an exsolved sulfide inclusion in CBa Gujba. The sulfide inclusion is located in a kamacite grain (Fe,Ni). The Cr map shows individual lamellae of daubreelite (red), and MSS_1 (green). The S map shows sulfur distribution is relatively constant. The P map shows a phosphide located at the metal-sulfide interface, which is not seen in the BSE image. The X-ray maps have been smoothed to remove pixelation.

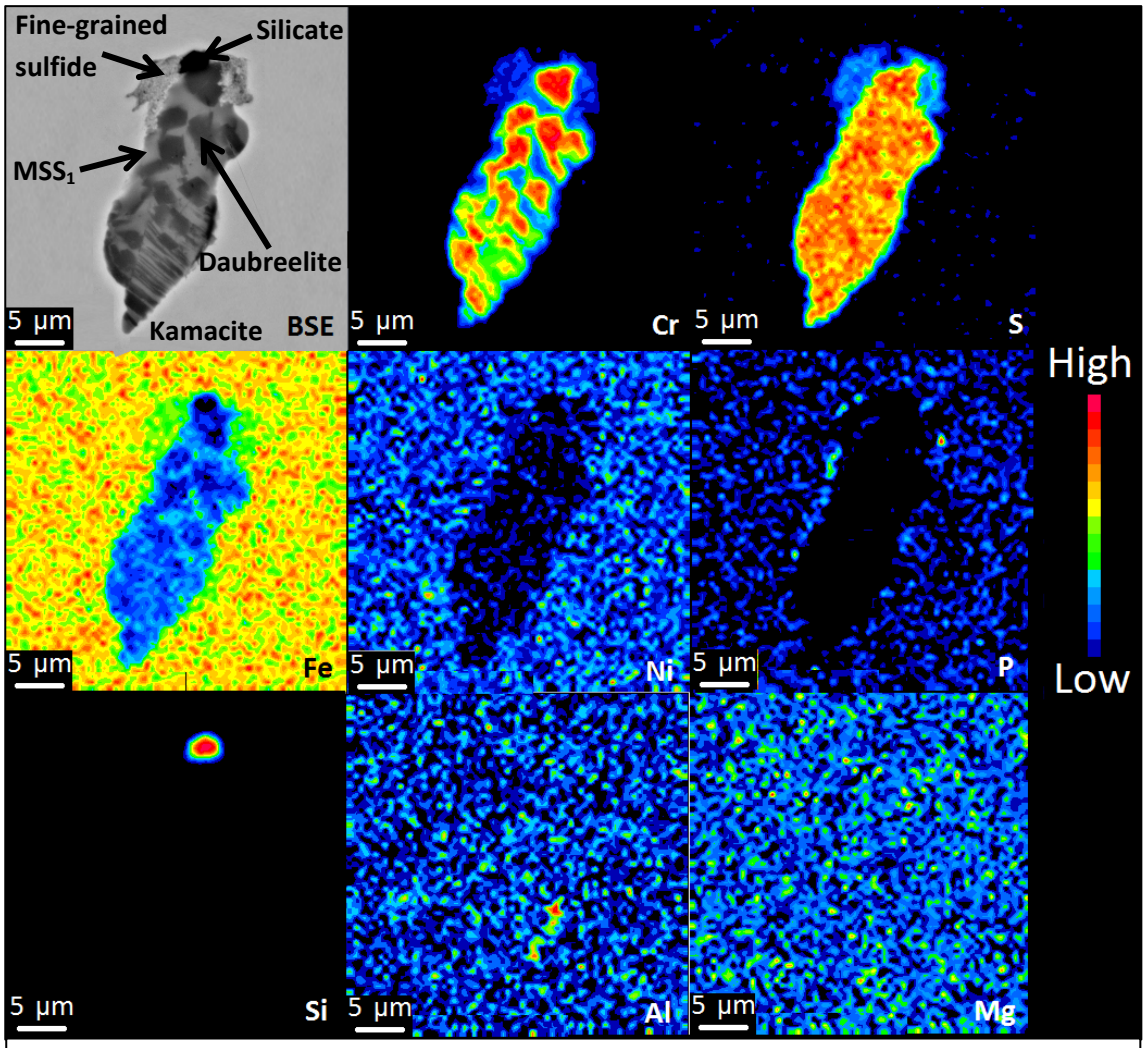

Figure A-3. EPMA X-ray maps of an exsolved sulfide inclusion in CBa Gujba. The BSE image is the same as in Figure 6e. The Cr map shows linear and blocky daubreelite (red) in an MSS_1 host (green), as well as a fine-grained sulfide at the top region (blue). The S map shows sulfur distribution is relatively constant in the sulfide, except for a lower concentration in the fine-grained region. The Fe and Ni maps show the sulfide is located in a kamacite grain. A slight enrichment is seen at the metal-sulfide interface in the P map, indicating the presence of phosphides. A silicate inclusion is located in the top region of the sulfide inclusion, indicated by the Si map. The Al map shows a region of high Al at the sulfide-metal interface, however, we have not identified this phase. The Mg map shows Mg is relatively low for both the metal and sulfide inclusion.

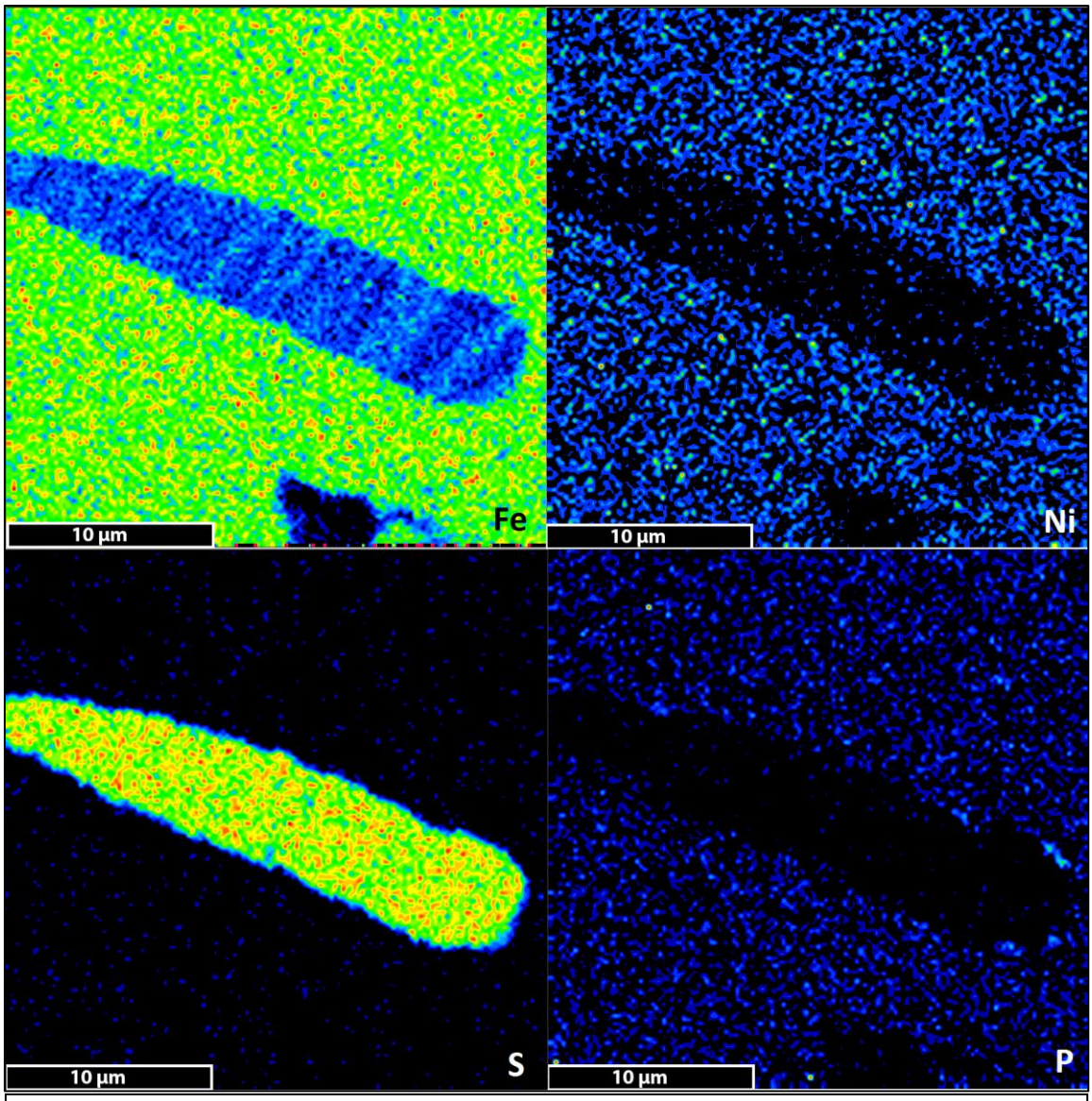

Figure A-4. EPMA X-ray maps of exsolved Sulfide 5 in CBa Gujba. BSE image and Cr map are shown in Figures 15a and b. Fe and Ni maps show the sulfide is located in a kamacite grain. The Fe map also shows a slight increase of Fe in the MSS_1 lamellae. The P map shows small phosphide inclusions at the sulfide-metal interface.

Appendix B – Tables of EPMA Analyses

This appendix contains EPMA analyses from sulfide inclusions, metal grains, and metal blebs from all four CB meteorites.

Table B-1. EPMA analyses of sulfides in CBa Gujba (wt.%)

	Line Numbers	Line	Si	P	S	Ni	Co	Fe	Cr	Mn	Cu	Zn	V	Total
Exsolved Sulfides	Un 51 Gujba_Grain9_Sulfide4	90	0.00	0.00	37.16	0.25	0.01	52.30	8.03	0.14	0.00	0.00	0.24	98.11
	Un 52 Gujba_Grain9_Sulfide5	91	0.00	0.00	37.87	0.14	0.00	50.02	9.64	0.16	0.00	0.00	0.42	98.25
	Un 3 Gujba_Grain6_Sulfide1	13	0.00	0.00	37.80	0.27	0.00	51.51	9.06	0.15	0.00	0.00	0.27	99.07
	Un 4 Gujba_Grain6_Sulfide2	14	0.00	0.00	38.39	0.20	0.01	44.31	15.56	0.18	0.14	0.00	0.27	99.07
	Un 50 Gujba_Grain6_Sulfide3	89	0.00	0.00	38.50	0.22	0.01	46.95	11.90	0.12	0.05	0.00	0.26	98.01
	Un 58 Gujba_Grain06_Sulfide1	111	0.00	0.01	37.84	0.20	0.00	50.19	9.93	0.07	0.00	0.01	0.36	98.61
	Un 59 Gujba_Grain06_Sulfide1	112	0.00	0.00	39.99	0.16	0.01	35.57	20.77	0.14	0.14	0.00	0.33	97.11
	Un 61 Gujba_Grain06_Sulfide4	118	0.00	0.07	35.86	0.46	0.03	54.11	7.46	0.06	0.03	0.00	0.25	98.34
	Un 62 Gujba_Grain06_Sulfide5	119	0.00	0.04	32.60	0.89	0.04	56.91	6.98	0.04	0.00	0.00	0.31	97.81
	Un 48 Gujba_Grain5_FIB_light	87	0.00	0.00	41.37	0.12	0.02	26.36	27.60	0.16	0.00	0.06	0.65	96.34
	Un 49 Gujba_Grain5_FIB_light(real)	88	0.00	0.00	37.11	0.27	0.00	48.50	10.86	0.05	0.06	0.00	0.62	97.46
	Un 66 Gujba_Grain05_Sulfide1	123	0.00	0.00	40.98	0.10	0.00	27.47	26.72	0.17	0.02	0.00	0.70	96.14
	Un 69 Gujba_Grain05_Sulfide4	137	0.00	0.01	41.31	0.23	0.00	28.32	26.79	0.15	0.08	0.00	0.55	97.44
	Un 72 Gujba_Grain03_Sulfide1	140	0.00	0.00	37.34	0.23	0.01	49.89	10.41	0.11	0.00	0.00	0.21	98.19
	Un 73 Gujba_Grain03_Sulfide2	141	0.00	0.00	38.37	0.22	0.02	41.22	16.08	0.17	0.00	0.00	0.19	96.25
	Un 76 Gujba_Grain03_Sulfide 4	147	0.00	0.00	37.46	0.22	0.00	52.22	8.47	0.08	0.00	0.00	0.21	98.66
	Un 77 Gujba_Grain03_Sulfide 5	148	0.00	0.00	37.98	0.22	0.00	45.82	12.82	0.17	0.00	0.00	0.21	97.23
	Un 79 Gujba_Grain03_Sulfide6	150	0.00	0.00	37.65	0.19	0.02	50.57	10.06	0.11	0.02	0.00	0.37	98.99
	Un 80 Gujba_Grain03_Sulfide6	151	0.00	0.01	39.30	0.20	0.00	43.35	14.78	0.17	0.02	0.00	0.33	98.18
	Un 81 Gujba_Grain03_Sulfide6	152	0.00	0.01	37.83	0.32	0.02	42.66	16.26	0.19	0.00	0.00	0.35	97.63
	Un 82 Gujba_Grain03_Sulfide7	153	0.00	0.00	37.73	0.23	0.01	50.67	9.50	0.10	0.00	0.00	0.21	98.44
	Un 53 Gujba_Grain9_Sulfide6 line	96	0.00	0.02	35.55	0.57	0.03	43.90	15.30	0.20	0.00	0.00	0.28	95.85
		97	0.00	0.01	34.55	0.50	0.03	51.81	9.86	0.13	0.08	0.00	0.25	97.23
		98	0.00	0.03	33.74	0.61	0.04	56.44	6.47	0.12	0.07	0.00	0.25	97.76
		99	0.00	0.04	33.10	0.72	0.04	50.23	11.44	0.22	0.18	0.01	0.26	96.24

		100	0.00	0.04	32.20	0.79	0.05	57.20	6.54	0.11	0.00	0.00	0.25	97.19
		101	0.00	0.03	33.47	0.78	0.04	49.58	12.00	0.19	0.10	0.00	0.26	96.46
		102	0.02	0.02	34.70	0.55	0.02	55.54	6.79	0.07	0.00	0.00	0.26	97.97
		103	0.00	0.01	35.81	0.41	0.02	49.95	9.95	0.16	0.00	0.03	0.28	96.60
		104	0.00	0.02	36.45	0.37	0.02	52.02	8.54	0.09	0.00	0.00	0.27	97.78
		105	0.00	0.01	36.31	0.36	0.01	53.30	7.76	0.08	0.02	0.02	0.28	98.16
		106	0.00	0.02	35.32	0.45	0.02	51.53	9.11	0.10	0.04	0.00	0.27	96.86
	Un 60 Gujba_Grain06_Sulfide3 line	115	0.00	0.02	41.31	0.25	0.02	27.01	27.73	0.08	0.05	0.00	0.67	97.13
		116	0.00	0.01	41.67	0.11	0.00	25.21	29.03	0.10	0.12	0.00	0.65	96.90
Exsolved Sulfides	Un 90 Gujba_Grain05_Sulfide1 line	161	0.00	0.01	36.44	0.26	0.01	47.92	11.18	0.08	0.00	0.00	0.64	96.55
		162	0.00	0.01	40.53	0.07	0.00	30.44	24.39	0.16	0.13	0.00	0.67	96.40
		163	0.04	0.00	36.72	0.25	0.00	49.49	9.62	0.05	0.00	0.00	0.69	96.86
		164	0.00	0.00	41.15	0.04	0.00	27.36	26.92	0.16	0.06	0.00	0.70	96.39
		165	0.00	0.00	37.62	0.22	0.00	46.96	11.93	0.06	0.06	0.01	0.65	97.51
		166	0.00	0.00	37.01	0.14	0.00	47.71	11.00	0.07	0.00	0.00	0.62	96.54
		167	0.00	0.00	36.34	0.22	0.01	49.31	9.64	0.04	0.02	0.00	0.64	96.23
		168	0.00	0.00	40.59	0.07	0.00	27.71	26.26	0.16	0.00	0.00	0.66	95.45
		169	0.00	0.00	39.24	0.10	0.01	35.37	20.43	0.12	0.00	0.02	0.57	95.87
		170	0.00	0.00	38.04	0.15	0.01	38.86	17.91	0.10	0.12	0.00	0.62	95.82
		171	0.00	0.00	38.41	0.20	0.02	35.30	19.41	0.09	0.03	0.00	0.66	94.12
		172	0.00	0.00	36.38	0.17	0.00	48.84	10.04	0.06	0.02	0.02	0.61	96.15
	Un 67 Gujba_Grain05_Sulfide2 line	124	0.04	0.00	39.00	0.12	0.01	42.43	15.51	0.08	0.00	0.00	0.39	97.59
		125	0.05	0.00	38.48	0.18	0.01	43.06	14.61	0.08	0.00	0.00	0.36	96.82
		126	0.02	0.00	38.56	0.16	0.01	42.20	15.55	0.09	0.04	0.00	0.38	97.02
		127	0.01	0.00	37.87	0.14	0.01	47.15	12.31	0.05	0.00	0.00	0.39	97.91
		128	0.00	0.00	38.09	0.17	0.00	48.14	11.41	0.06	0.01	0.00	0.39	98.29
		129	0.00	0.00	38.22	0.19	0.02	45.64	13.32	0.08	0.00	0.00	0.38	97.85
		130	0.00	0.00	38.35	0.18	0.00	45.73	12.84	0.06	0.05	0.00	0.41	97.63
		131	0.00	0.00	38.58	0.13	0.00	42.82	15.17	0.09	0.00	0.00	0.37	97.16
		132	0.00	0.00	38.20	0.16	0.00	44.39	14.07	0.06	0.00	0.04	0.42	97.35
		133	0.01	0.01	37.21	0.24	0.01	41.26	15.98	0.09	0.00	0.00	0.38	95.19

Exsolved Sulfides		134	0.02	0.00	37.29	0.22	0.00	53.37	7.73	0.04	0.00	0.04	0.37	99.07
		135	0.00	0.00	39.49	0.11	0.00	33.82	22.74	0.10	0.00	0.00	0.30	96.56
	Un 75 Gujba_Grain03_Sulfide 3 line	144	0.04	0.32	27.57	1.50	0.08	59.20	8.54	0.07	0.00	0.00	0.19	97.52
		145	0.00	0.01	38.61	0.26	0.01	39.80	19.09	0.25	0.00	0.00	0.25	98.28
		146	0.00	0.03	33.53	0.69	0.03	53.07	9.35	0.11	0.00	0.00	0.22	97.02
	Un 7 GujbaBruker_G16_S1	29	0.00	0.00	37.79	0.09	0.01	50.38	9.62	0.14	0.15	0.06	0.50	98.74
	Un 8 GujbaBruker_G16_S2	30	0.00	0.00	38.02	0.14	0.01	51.50	9.03	0.14	0.08	0.00	0.39	99.30
	Un 9 GujbaBruker_G16_S3	31	0.00	0.00	38.74	0.14	0.01	49.35	10.99	0.13	0.00	0.03	0.43	99.81
	Un 10 GujbaBruker_G16_S4	32	0.00	0.02	36.37	0.32	0.00	49.78	11.13	0.14	0.06	0.00	0.43	98.26
	Un 36 GujbaBruker_G16_S5	57	0.00	0.01	36.72	0.20	0.02	55.39	6.15	0.09	0.01	0.00	0.28	98.87
	Un 37 GujbaBruker_G16_S6	58	0.00	0.00	37.75	0.19	0.00	52.51	8.29	0.15	0.07	0.00	0.12	99.07
	Un 21 GujbaBruker_G9_S1_L	42	0.00	0.00	37.84	0.13	0.02	54.44	7.17	0.28	0.06	0.03	0.13	100.10
	Un 23 GujbaBruker_G9_S2	44	0.00	0.00	37.49	0.14	0.01	54.79	6.76	0.26	0.04	0.00	0.29	99.77
	Un 24 GujbaBruker_G9_S3	45	0.02	0.00	35.98	0.50	0.01	53.21	6.91	0.26	0.23	0.00	0.22	97.34
	Un 25 GujbaBruker_G9_S4	46	0.00	0.00	37.65	0.17	0.00	52.59	7.84	0.26	0.17	0.00	0.22	98.91
	Un 56 GujbaBruker_G9_S5	77	0.01	0.00	37.99	0.13	0.02	52.57	7.72	0.27	0.64	0.00	0.23	99.58
	Un 26 GujbaBruker_G8_S1	47	0.00	0.01	38.24	0.09	0.00	50.59	9.72	0.21	0.12	0.01	0.41	99.39
	Un 28 GujbaBruker_G8_S2	49	0.00	0.01	37.36	0.22	0.01	55.73	6.07	0.14	0.01	0.00	0.17	99.71
	Un 59 GujbaBruker_G8_S3	80	0.00	0.01	38.79	0.12	0.01	45.77	13.03	0.28	0.00	0.00	0.39	98.39
	Un 60 GujbaBruker_G8_S4	81	0.01	0.00	37.33	0.17	0.03	51.46	8.80	0.16	0.02	0.00	0.26	98.25
	Un 61 GujbaBruker_G8_S5	82	0.00	0.00	37.87	0.10	0.00	52.13	8.54	0.24	0.00	0.00	0.20	99.09
	Un 29 GujbaBruker_G4_S1	50	0.00	0.01	37.85	0.20	0.00	49.54	10.85	0.16	0.05	0.00	0.57	99.23
	Un 30 GujbaBruker_G4_S2	51	0.06	0.03	35.83	0.44	0.01	51.27	8.97	0.09	0.06	0.03	0.30	97.09
	Un 64 GujbaBruker_G4_S3	85	0.00	0.01	36.48	0.37	0.02	53.59	8.03	0.09	0.01	0.00	0.32	98.93
	Un 65 GujbaBruker_G4_S4	86	0.00	0.04	35.77	0.68	0.04	51.03	10.28	0.10	0.03	0.00	0.40	98.35
	Un 32 GujbaBruker_G25_S1	53	0.59	0.03	35.23	0.40	0.01	50.32	8.89	0.07	0.01	0.00	0.34	95.89
	Un 67 GujbaBruker_G25_S2	88	0.00	0.01	34.76	0.27	0.03	53.47	8.00	0.08	0.02	0.00	0.34	96.97
	Un 68 GujbaBruker_G25_S3	89	0.00	0.03	37.17	0.26	0.02	54.50	6.64	0.07	0.01	0.00	0.25	98.94

	Un 69 GujbaBruker_G25_S4	90	0.00	0.04	32.89	0.87	0.06	57.48	6.92	0.05	0.00	0.00	0.55	98.86
	Un 73 GujbaBruker_G26_S2	94	0.00	0.06	32.03	1.38	0.06	37.90	23.75	0.12	0.00	0.00	0.79	96.10
	Un 74 GujbaBruker_G26_S3	95	0.00	0.06	33.59	1.35	0.08	40.70	20.80	0.16	0.08	0.00	0.75	97.56
Homogeneous Sulfides	Un 83 Gujba_Grain11_Sulfide1	154	0.00	0.00	36.91	0.18	0.00	55.36	5.86	0.09	0.00	0.06	0.16	98.63
	Un 84 Gujba_Grain11_Sulfide2	155	0.00	0.00	36.39	0.26	0.03	57.79	4.05	0.08	0.00	0.04	0.08	98.73
	Un 85 Gujba_Grain11_Sulfide3	156	0.00	0.01	36.65	0.31	0.01	55.07	6.41	0.12	0.00	0.00	0.16	98.74
	Un 2 GujbaBruker_G20_S1	25	0.00	0.00	35.96	0.21	0.01	59.94	2.27	0.02	0.08	0.00	0.02	98.51
	Un 3 GujbaBruker_G20_S2	26	0.01	0.00	36.24	0.20	0.00	60.98	1.67	0.03	0.10	0.00	0.03	99.26
	Un 4 GujbaBruker_G20_S3	27	0.01	0.01	36.25	0.11	0.01	61.14	1.78	0.02	0.00	0.00	0.04	99.36
	Un 16 GujbaBruker_G13_S2_L	37	0.00	0.01	36.44	0.28	0.00	61.33	1.48	0.02	0.05	0.00	0.04	99.63
	Un 18 GujbaBruker_G13_S3_L	39	0.00	0.01	36.19	0.16	0.02	61.30	1.40	0.04	0.02	0.08	0.16	99.39
	Un 42 GujbaBruker_G13_S2_L	63	0.03	0.00	36.48	0.15	0.01	61.64	1.51	0.03	0.09	0.00	0.04	99.97
	Un 44 GujbaBruker_G13_S3_L	65	0.01	0.03	33.89	0.18	0.00	60.41	1.30	0.05	0.08	0.00	0.15	96.12
	Un 50 GujbaBruker_G11_S1	71	0.00	0.00	36.87	0.21	0.03	60.05	2.29	0.04	0.03	0.00	0.01	99.54
	Un 51 GujbaBruker_G11_S2	72	0.00	0.00	36.64	0.25	0.02	58.84	3.53	0.04	0.02	0.00	0.08	99.43
	Un 52 GujbaBruker_G11_S3	73	0.00	0.01	35.75	0.17	0.01	61.09	1.94	0.01	0.05	0.03	0.04	99.12
Homogeneous w. Metal Blebs	Un 63 Gujba_Grain06_Sulfide6_Metal blob	120	0.00	0.10	24.16	4.31	0.09	64.95	3.50	0.01	0.00	0.00	0.11	97.23
	Un 15 GujbaBruker_G13_S1_metal globule	36	0.02	0.22	4.75	7.48	0.26	86.32	0.76	0.02	0.00	0.00	0.02	99.85
	Un 27 GujbaBruker_G8_S2_metal globule	48	0.01	0.31	0.34	10.30	0.32	88.65	0.61	0.00	0.03	0.00	0.00	100.58
	Un 87 Gujba_Grain11_Sulfide4_Metal glob	158	0.01	0.23	9.74	7.80	0.21	80.44	1.30	0.02	0.02	0.00	0.03	99.81
	Un 33 GujbaBruker_G20_S4	54	0.00	0.00	36.25	0.27	0.01	61.12	1.75	0.02	0.03	0.00	0.04	99.50
	Un 41 GujbaBruker_G13_S1	62	0.00	0.00	36.63	0.20	0.02	59.32	3.20	0.13	0.06	0.00	0.04	99.60
	Un 53 GujbaBruker_G11_S4	74	0.00	0.00	34.45	0.66	0.00	60.05	1.92	0.03	0.17	0.00	0.04	97.33
	Un 78 GujbaBruker_G23_S1	99	0.02	0.02	33.92	1.33	0.04	62.18	2.59	0.07	0.06	0.00	0.06	100.29

Table B-2. TEM-EDS analyses of Sulfide 5 in CBa Gujba (wt.%)						
Spectrum	**S**	**V**	**Cr**	**Fe**	**Ni**	**Total**
Spectrum 1 FeS lamellae	34.15	0.95	6.77	59.86	0.00	100.00
Spectrum 2 same as spot 1	36.02	0.52	6.13	57.19	0.14	100.00
Spectrum 3	45.78	0.35	32.64	22.91	0.00	100.00
Spectrum 4	48.17	0.03	27.69	25.78	0.00	100.00
Spectrum 5 Thick lamellae	44.47	0.10	33.25	22.19	0.00	100.00
Spectrum 6 dark lamellae	45.27	0.00	34.36	20.49	0.01	100.00
Spectrum 9	38.58	0.72	16.98	42.36	1.36	100.00
Spectrum 11 adjacent to particle in host	37.48	0.38	6.02	56.01	0.12	100.00
Spectrum 13	44.48	0.18	33.84	21.53	0.00	100.00
Spectrum 14	44.73	0.23	34.67	20.43	0.00	100.00
Spectrum 15	45.45	0.00	33.77	20.67	0.19	100.00
Spectrum 18	38.96	0.22	20.02	42.18	0.00	100.00
Spectrum 19	46.94	0.00	34.59	20.61	0.00	100.00
Spectrum 21	48.81	0.00	33.78	19.48	0.00	100.00
Spectrum 22	36.26	0.80	20.14	45.04	0.00	100.00
Spectrum 24	35.75	0.59	9.05	56.45	0.00	100.00
Spectrum 25	44.39	0.00	33.71	23.85	0.00	100.00
Spectrum 26	48.32	0.00	31.98	21.04	0.00	100.00
Spectrum 27	40.58	0.49	19.11	41.69	0.00	100.00
Spectrum 46	44.65	0.08	34.02	21.22	0.02	100.00
Spectrum 47	37.98	0.90	5.38	55.63	0.11	100.00
Spectrum 48	36.32	0.75	6.36	58.39	0.00	100.00
Spectrum 49	43.90	0.07	21.05	36.56	0.00	100.00
Spectrum 51	43.46	0.05	36.06	22.49	0.00	100.00
Spectrum 52	41.97	0.03	32.29	25.75	0.00	100.00
Spectrum 55	41.32	0.37	27.09	31.22	0.00	100.00
Spectrum 56	42.49	0.12	33.17	24.00	0.22	100.00
Spectrum 57	43.54	0.06	35.82	22.69	0.00	100.00
Spectrum 7 bright lamellae core	37.35	1.64	4.05	57.11	0.00	100.00
Spectrum 8 same lamellae	36.85	1.42	4.17	57.50	0.05	100.00

Spectrum 12 Bright lamellae	37.78	1.88	4.23	56.19	0.00	100.00
Spectrum 16	34.02	2.44	4.98	59.13	0.00	100.00
Spectrum 17	39.44	1.73	10.78	49.41	0.00	100.00
Spectrum 20	38.04	1.08	4.84	56.01	0.03	100.00
Spectrum 23	35.42	1.10	6.11	59.42	0.00	100.00
Spectrum 44	38.03	1.36	3.96	58.14	0.00	100.00
Spectrum 50	38.98	1.47	9.81	49.75	0.00	100.00
Spectrum 53	35.25	1.36	4.37	58.89	0.13	100.00
Spectrum 54	38.41	1.29	10.85	51.60	0.00	100.00
Spectrum 45 Ni-bearing nanoparticles	34.28	1.33	9.48	47.23	7.69	100.00
Spectrum 10 Ni-rich particle	27.95	0.10	5.18	50.35	16.41	100.00

Table B-3. EPMA analyses of metal in CBa Gujba (wt.%)													
Line Numbers	**Line**	**Si**	**P**	**S**	**Ni**	**Co**	**Fe**	**Cr**	**Mn**	**Cu**	**Zn**	**V**	**Total**
Un 54 Gujba_Grain9_Metal4	107	0.05	0.35	0.02	5.73	0.27	93.18	0.36	0.00	0.00	0.00	0.00	99.95
Un 56 Gujba_Grain9_Metal2	109	0.06	0.36	0.03	5.81	0.29	93.20	0.28	0.01	0.01	0.00	0.00	100.04
Un 64 Gujba_Grain06_Metal1	121	0.00	0.37	0.01	6.79	0.34	92.23	0.23	0.00	0.00	0.00	0.00	99.97
Un 70 Gujba_Grain05_Metal2	138	0.00	0.37	0.01	6.96	0.33	92.10	0.35	0.00	0.00	0.00	0.01	100.13
Un 74 Gujba_Grain03_Metal1	142	0.02	0.30	0.01	6.36	0.33	93.54	0.06	0.00	0.00	0.00	0.00	100.62
Un 88 Gujba_Grain11_Metal1	159	0.02	0.34	0.01	5.49	0.26	93.41	0.20	0.00	0.01	0.00	0.00	99.74
Un 55 Gujba_Grain9_Metal3	108	0.04	0.35	0.01	5.69	0.27	93.13	0.32	0.00	0.00	0.00	0.00	99.82
Un 57 Gujba_Grain9_Metal1	110	0.07	0.38	0.01	5.73	0.27	92.98	0.36	0.00	0.00	0.00	0.00	99.80
Un 65 Gujba_Grain06_Metal2	122	0.01	0.33	0.00	6.62	0.31	92.70	0.31	0.00	0.00	0.00	0.00	100.29
Un 71 Gujba_Grain05_Metal1	139	0.00	0.23	0.01	6.94	0.34	92.05	0.33	0.00	0.00	0.00	0.02	99.92
Un 78 Gujba_Grain03_Metal2	149	0.00	0.32	0.00	6.41	0.30	92.64	0.09	0.00	0.03	0.00	0.00	99.80
Un 89 Gujba_Grain11_Metal2	160	0.00	0.27	0.00	5.38	0.28	93.52	0.28	0.00	0.01	0.03	0.00	99.78
Gujba3_sulfide-11	13	0.00	0.24	0.29	6.92	0.25	92.70	0.13	0.00	0.00	0.00	0.00	100.53
Gujba3_sulfide-12	14	0.00	0.31	0.01	5.99	0.28	94.21	0.11	0.00	0.00	0.00	0.00	100.92
Gujba3_sulfide-13	15	0.01	0.31	0.00	6.17	0.29	94.14	0.13	0.00	0.00	0.00	0.00	101.06
Gujba3_sulfide-14	16	0.00	0.30	0.00	6.64	0.29	93.83	0.14	0.00	0.00	0.07	0.00	101.28
Gujba3_sulfide-15	17	0.01	0.17	0.01	6.93	0.29	92.88	0.05	0.01	0.02	0.00	0.00	100.37
Gujba3_sulfide-16	18	0.00	0.29	0.00	6.25	0.28	93.47	0.17	0.00	0.00	0.09	0.00	100.54
Gujba3_sulfide-17	19	0.00	0.28	0.00	6.44	0.27	93.94	0.16	0.01	0.03	0.00	0.00	101.13
Gujba4-2	21	0.01	0.28	0.01	5.96	0.40	93.91	0.18	0.07	0.08	0.16	0.00	101.07
Gujba5-8	31	0.02	0.27	1.22	6.68	0.40	92.24	0.75	0.07	0.11	0.23	0.00	101.98
Gujba5-9	32	0.02	0.28	1.08	6.74	0.42	91.53	0.97	0.07	0.05	0.09	0.00	101.24
Gujba5-16	39	0.02	0.31	0.00	6.98	0.42	92.77	0.38	0.06	0.14	0.27	0.00	101.34
Gujba5-17	40	0.01	0.34	0.00	6.82	0.32	92.87	0.36	0.00	0.00	0.03	0.00	100.74
Gujba5-18	41	0.01	0.31	0.01	6.69	0.28	93.03	0.37	0.00	0.00	0.00	0.00	100.69
Gujba5-19	42	0.01	0.33	0.01	6.80	0.33	93.12	0.33	0.00	0.00	0.00	0.00	100.92
Gujba6-1	43	0.00	0.31	0.20	6.62	0.28	92.99	0.47	0.00	0.00	0.09	0.00	100.95
Gujba6-2	44	0.00	0.40	0.05	6.86	0.31	92.71	0.41	0.00	0.05	0.02	0.00	100.80
Gujba6-4	75	0.03	0.43	0.02	6.64	0.30	92.57	0.22	0.00	0.00	0.06	0.00	100.25
Gujba6-7	78	0.02	0.35	0.02	6.61	0.31	93.14	0.31	0.00	0.00	0.00	0.00	100.76

Gujba6-8	79	0.02	0.38	0.35	6.71	0.30	92.29	0.31	0.00	0.00	0.18	0.00	100.54
Gujba6-9	80	0.01	0.36	0.01	6.67	0.33	92.93	0.31	0.00	0.00	0.00	0.00	100.62
Gujba6-10	81	0.01	0.29	0.02	6.69	0.31	92.82	0.24	0.00	0.00	0.00	0.00	100.38
Gujba6-11	82	0.00	0.40	0.01	6.56	0.31	92.32	0.30	0.00	0.00	0.00	0.00	99.91
Gujba6-12	83	0.02	0.33	0.01	6.52	0.31	93.19	0.31	0.00	0.00	0.00	0.00	100.68
Un 6 GujbaBruker_G20_M1	28	0.01	0.31	0.00	6.63	0.33	93.26	0.10	0.00	0.04	0.00	0.01	100.67
Un 13 GujbaBruker_G16_M1	34	0.03	0.32	0.01	5.91	0.32	92.73	0.33	0.00	0.00	0.00	0.01	99.66
Un 14 GujbaBruker_G16_M2	35	0.07	0.33	0.00	6.03	0.30	93.35	0.39	0.00	0.00	0.00	0.00	100.47
Un 31 GujbaBruker_G4_M1	52	0.03	0.34	0.01	7.20	0.34	92.47	0.30	0.00	0.00	0.00	0.00	100.69
Un 35 GujbaBruker_G20_M3	56	0.00	0.28	0.00	6.56	0.32	92.60	0.11	0.00	0.00	0.00	0.00	99.89
Un 40 GujbaBruker_G16_M3	61	0.04	0.34	0.02	5.96	0.30	92.96	0.36	0.00	0.00	0.00	0.01	99.98
Un 47 GujbaBruker_G13_M1	68	0.01	0.33	0.01	5.20	0.27	95.16	0.11	0.00	0.00	0.00	0.00	101.08
Un 48 GujbaBruker_G13_M2	69	0.01	0.28	0.00	5.22	0.28	95.17	0.12	0.00	0.05	0.00	0.00	101.13
Un 49 GujbaBruker_G13_M3	70	0.00	0.33	0.01	5.22	0.29	94.69	0.16	0.00	0.00	0.00	0.01	100.71
Un 54 GujbaBruker_G11_M1	75	0.00	0.29	0.00	5.99	0.31	94.01	0.11	0.00	0.01	0.00	0.01	100.74
Un 55 GujbaBruker_G11_M2	76	0.00	0.31	0.01	6.02	0.30	94.16	0.10	0.00	0.00	0.00	0.00	100.90
Un 57 GujbaBruker_G9_M1	78	0.00	0.32	0.01	5.75	0.30	94.05	0.21	0.00	0.00	0.00	0.00	100.64
Un 58 GujbaBruker_G9_M2	79	0.01	0.29	0.01	5.97	0.30	94.82	0.10	0.00	0.02	0.00	0.00	101.50
Un 62 GujbaBruker_G8_M1	83	0.04	0.35	0.00	6.48	0.31	92.69	0.34	0.01	0.00	0.00	0.01	100.22
Un 63 GujbaBruker_G8_M2	84	0.03	0.33	0.01	6.79	0.31	93.49	0.21	0.00	0.00	0.08	0.00	101.24
Un 66 GujbaBruker_G4_M2	87	0.03	0.22	0.00	7.05	0.34	92.13	0.35	0.00	0.00	0.00	0.00	100.13
Un 70 GujbaBruker_G25_M1	91	0.03	0.39	0.01	7.23	0.33	92.16	0.23	0.00	0.04	0.00	0.01	100.43
Un 71 GujbaBruker_G25_M2	92	0.03	0.38	0.00	7.15	0.35	91.68	0.30	0.00	0.00	0.00	0.01	99.91
Un 76 GujbaBruker_G26_M1	97	0.00	0.30	0.00	7.08	0.35	92.93	0.27	0.00	0.00	0.00	0.00	100.93
Un 77 GujbaBruker_G26_M2	98	0.02	0.32	0.00	7.19	0.34	92.74	0.33	0.00	0.05	0.00	0.01	101.00
Un 79 GujbaBruker_G23_M1	100	0.01	0.35	0.00	5.77	0.29	94.09	0.19	0.00	0.00	0.00	0.01	100.70

Table B-4. EPMA analyses of sulfides in CBa Weatherford (wt.%)														
	Line Numbers	**Line**	**Si**	**P**	**S**	**Ni**	**Co**	**Fe**	**Cr**	**Mn**	**Cu**	**Zn**	**V**	**Total**
Exsolved Sulfides	Un 7 Weather_Grain16_Sulfide2	16	0.00	0.05	35.28	0.64	0.02	48.51	11.93	0.11	0.09	0.03	0.35	97.00
	Un 8 Weather_Grain16_Sulfide3	17	0.00	0.02	33.55	0.46	0.02	50.81	10.13	0.10	0.06	0.00	0.27	95.43
	Un 9 Weather_Grain16_Sulfide4	18	0.00	0.06	35.81	0.52	0.01	49.22	11.67	0.12	0.03	0.00	0.34	97.79
	Un 13 Weather_Grain16_Sulfide6	22	0.00	0.00	37.47	0.20	0.01	53.45	7.37	0.11	0.00	0.00	0.22	98.82
	Un 14 Weather_Grain8_Sulfide1	23	0.00	0.01	38.25	0.20	0.02	49.38	10.41	0.07	0.00	0.02	0.28	98.65
	Un 15 Weather_Grain8_Sulfide2	24	0.00	0.05	33.34	0.69	0.04	53.73	8.86	0.07	0.00	0.00	0.24	97.01
	Un 19 Weather_Grain8_Sulfide3	40	0.00	0.02	36.95	0.48	0.02	47.03	13.10	0.07	0.06	0.00	0.33	98.07
	Un 20 Weather_Grain8_Sulfide7	41	0.00	0.06	36.45	0.69	0.02	45.08	15.50	0.09	0.10	0.03	0.38	98.41
	Un 24 Weather_Grain9_Sulfide 1	59	0.02	0.04	35.08	0.65	0.02	56.62	5.34	0.24	0.04	0.00	0.11	98.17
	Un 25 Weather_Grain9_Sulfide 2	60	0.01	0.00	37.63	0.16	0.01	53.17	7.18	0.33	0.00	0.00	0.16	98.65
	Un 26 Weather_Grain9_Sulfide 3	61	0.00	0.01	37.20	0.25	0.00	54.33	6.41	0.32	0.00	0.00	0.15	98.66
	Un 29 Weather_Grain6_Sulfide1	64	0.00	0.02	39.95	0.11	0.01	43.26	14.89	0.15	0.05	0.00	0.30	98.74
	Un 30 Weather_Grain6_Sulfide2	65	0.00	0.01	37.30	0.22	0.01	41.56	17.17	0.13	0.03	0.00	0.22	96.66
	Un 31 Weather_Grain6_Sulfide3	66	0.06	0.01	38.34	0.14	0.01	35.98	20.39	0.20	0.10	0.03	0.26	95.51
	Un 33 Weather_Grain6_Sulfide4	72	0.00	0.02	38.57	0.19	0.00	46.13	13.05	0.07	0.00	0.00	0.24	98.27
	Un 34 Weather_Grain6_Sulfide5	73	0.15	0.01	38.66	0.19	0.02	42.22	15.49	0.17	0.01	0.03	0.25	97.19
	Un 36 Weather_Grain6_Sulfide7	75	0.00	0.00	39.00	0.13	0.01	45.58	13.33	0.13	0.06	0.00	0.22	98.45
	Un 37 Weather_Grain6_Sulfide8	76	0.00	0.03	37.97	0.43	0.03	42.77	15.71	0.15	0.07	0.00	0.24	97.39
	Un 38 Weather_Grain6_Sulfide9	77	0.00	0.02	38.62	0.18	0.00	44.56	13.95	0.10	0.05	0.00	0.24	97.71
	Un 39 Weather_Grain6_Sulfide10	78	0.01	0.04	34.73	0.81	0.07	41.41	19.47	0.21	0.11	0.00	0.24	97.10
	Un 43 Weather_Grain5_Sulfide2	82	0.00	0.01	36.73	0.22	0.01	58.93	2.96	0.02	0.04	0.00	0.06	98.99
	Un 44 Weather_Grain5_Sulfide3	83	0.00	0.00	36.67	0.20	0.00	59.47	2.67	0.03	0.04	0.00	0.06	99.17
	Un 45 Weather_Grain5_Sulfide4	84	0.02	0.00	36.83	0.22	0.01	59.00	2.57	0.05	0.14	0.06	0.05	98.95
	Un 16 Weather_Grain8_Sulfide4 line	25	0.00	0.02	35.73	0.54	0.04	44.66	15.09	0.04	0.00	0.00	0.41	96.54
		26	0.00	0.01	38.76	0.19	0.02	43.90	14.70	0.05	0.00	0.04	0.46	98.13
		27	0.00	0.03	36.93	0.48	0.05	38.55	19.61	0.15	0.03	0.00	0.43	96.25
	Un 17 Weather_Grain8_Sulfide5 line	31	0.00	0.08	29.96	1.57	0.07	58.60	8.38	0.06	0.05	0.00	0.23	99.00
		32	0.00	0.10	27.42	1.85	0.09	59.82	7.48	0.06	0.04	0.00	0.20	97.05
	Un 18 Weather_Grain8_Sulfide6 line	35	0.00	0.03	33.89	0.61	0.03	47.92	12.65	0.08	0.00	0.00	0.31	95.52

		36	0.00	0.01	38.80	0.23	0.00	44.72	13.89	0.09	0.06	0.00	0.36	98.17
		37	0.00	0.01	38.86	0.20	0.00	45.17	13.42	0.08	0.02	0.00	0.33	98.10
	Un 23 Weather_Grain8_Sulfide 8 line	44	0.00	0.03	36.81	0.52	0.04	39.86	19.55	0.19	0.03	0.00	0.35	97.38
		45	0.00	0.00	38.82	0.09	0.00	47.07	11.96	0.07	0.07	0.00	0.37	98.46
		46	0.00	0.00	38.86	0.11	0.00	45.61	12.90	0.08	0.05	0.00	0.37	97.99
		47	0.00	0.00	38.81	0.10	0.01	46.02	12.64	0.08	0.00	0.00	0.38	98.05
		48	0.00	0.00	39.58	0.09	0.01	41.93	15.53	0.10	0.00	0.00	0.38	97.63
		49	0.00	0.01	39.01	0.40	0.00	43.52	14.40	0.09	0.00	0.00	0.38	97.82
		50	0.00	0.00	38.83	0.11	0.00	45.90	12.95	0.07	0.05	0.00	0.39	98.29
		51	0.00	0.00	38.76	0.30	0.00	44.99	13.43	0.08	0.00	0.00	0.37	97.94
		52	0.00	0.00	39.42	0.12	0.01	39.13	17.92	0.14	0.01	0.02	0.38	97.14
		53	0.00	0.01	38.77	0.13	0.01	47.02	12.09	0.09	0.03	0.00	0.37	98.51
		54	0.00	0.00	38.66	0.43	0.02	46.09	12.19	0.07	0.03	0.03	0.38	97.90
		55	0.00	0.00	38.56	0.39	0.00	47.30	11.74	0.09	0.00	0.00	0.38	98.45
		56	0.00	0.01	38.51	0.43	0.00	47.53	11.20	0.09	0.00	0.00	0.37	98.13
		57	0.00	0.02	37.43	0.55	0.03	43.11	15.37	0.13	0.00	0.04	0.37	97.06
	Un 32 Weather_Grain6_Sulfide6 line	67	0.00	0.04	37.71	0.25	0.02	41.14	16.56	0.12	0.00	0.01	0.28	96.13
		68	0.00	0.05	38.79	0.25	0.02	39.04	18.56	0.16	0.06	0.00	0.28	97.20
		69	0.00	0.07	30.58	1.08	0.04	49.81	12.52	0.08	0.01	0.00	0.22	94.40
Homogeneous Sulfides	Un 43 Weather_Grain5_Sulfide2	82	0.00	0.01	36.73	0.22	0.01	58.93	2.96	0.02	0.04	0.00	0.06	98.99
	Un 44 Weather_Grain5_Sulfide3	83	0.00	0.00	36.67	0.20	0.00	59.47	2.67	0.03	0.04	0.00	0.06	99.17
	Un 45 Weather_Grain5_Sulfide4	84	0.02	0.00	36.83	0.22	0.01	59.00	2.57	0.05	0.14	0.06	0.05	98.95
Homogeneous w. Metal Blebs	Un 12 Weather_Grain16_Sulfide5_Metal glob	21	0.00	0.08	28.57	2.48	0.06	60.35	5.57	0.07	0.01	0.00	0.17	97.36
	Un 15 Weather_Grain8_Sulfide2	24	0.00	0.05	33.34	0.69	0.04	53.73	8.86	0.07	0.00	0.00	0.24	97.01
	Un 41 Weather_Grain5_Sulfide1_Metal glob	80	0.02	0.18	7.20	14.11	0.28	77.27	0.55	0.00	0.09	0.00	0.00	99.70
	Un 42 Weather_Grain5_Sulfide1_Metal glob2	81	0.00	0.03	28.24	3.48	0.09	64.00	1.83	0.01	0.00	0.00	0.03	97.72

Table B-5. EPMA analyses of metal in CBa Weatherford (wt.%)													
Line Numbers	**Line**	**Si**	**P**	**S**	**Ni**	**Co**	**Fe**	**Cr**	**Mn**	**Cu**	**Zn**	**V**	**Total**
Un 10 Weather_Grain16_Metal1	19	0.018	0.357	0.112	6.226	0.285	93.473	0.235	0.000	0.005	0.000	0.008	100.72
Un 21 Weather_Grain8_Metal1	42	0.042	0.330	0.021	6.377	0.282	92.128	0.241	0.000	0.063	0.000	0.002	99.49
Un 27 Weather_Grain9_Metal1	62	0.000	0.327	0.005	5.896	0.297	93.392	0.150	0.000	0.000	0.000	0.004	100.07
Un 35 Weather_Grain6_Metal1	74	0.004	0.348	0.015	5.288	0.289	93.892	0.106	0.000	0.000	0.000	0.000	99.94
Un 46 Weather_Grain5_Metal1	85	0.004	0.299	0.463	6.142	0.297	92.342	0.257	0.000	0.000	0.000	0.000	99.81
Un 11 Weather_Grain16_Metal2	20	0.032	0.387	0.003	6.003	0.298	93.521	0.298	0.016	0.000	0.000	0.002	100.56
Un 22 Weather_Grain8_Metal2	43	0.051	0.403	0.002	5.505	0.313	93.545	0.395	0.000	0.000	0.000	0.007	100.22
Un 28 Weather_Grain9_Metal	63	0.012	0.343	0.018	5.637	0.292	93.424	0.178	0.007	0.001	0.000	0.000	99.91
Un 40 Weather_Grain6_Metal2	79	0.008	0.327	0.001	5.451	0.267	93.495	0.180	0.000	0.000	0.000	0.000	99.73
Un 47 Weather_Grain5_Metal2	86	0.000	0.304	0.021	5.991	0.294	92.890	0.123	0.000	0.006	0.000	0.000	99.63
weath8-33	93	0.041	0.333	3.440	5.627	0.252	87.192	1.484	0.000	0.000	0.000	0.000	98.37
weath6-14	44	0.018	0.313	0.003	5.823	0.271	92.542	0.131	0.000	0.050	0.000	0.000	99.15
weath2-14	74	0.015	0.317	0.011	5.904	0.289	92.660	0.203	0.000	0.044	0.000	0.000	99.44
weath8-34	94	0.057	0.354	0.002	6.068	0.301	91.435	0.383	0.000	0.050	0.000	0.000	98.65
weath8-37	97	0.056	0.380	0.000	5.953	0.304	90.993	0.355	0.000	0.039	0.000	0.000	98.08
weath4-8	82	0.053	0.168	2.679	7.109	0.307	86.741	0.280	0.000	0.064	0.000	0.000	97.40
weath8-36	96	0.046	0.414	0.000	6.300	0.313	91.834	0.299	0.000	0.089	0.006	0.000	99.30
weath4-11	85	0.078	0.237	1.788	7.117	0.320	87.361	0.121	0.000	0.161	0.000	0.000	97.18
weath8-35	95	0.046	0.366	0.002	5.888	0.328	91.588	0.434	0.001	0.111	0.000	0.000	98.76
weath4-2	76	0.038	0.210	0.524	7.381	0.332	90.378	0.133	0.000	0.047	0.000	0.000	99.04
weath4-14	88	0.018	0.267	0.035	7.341	0.333	90.995	0.106	0.000	0.042	0.024	0.000	99.16
weath4-6	80	0.017	0.209	0.056	7.314	0.343	91.433	0.123	0.000	0.058	0.000	0.000	99.55
weath4-5	79	0.031	0.155	0.106	6.852	0.346	91.239	0.135	0.000	0.019	0.000	0.000	98.88
weath4-12	86	0.028	0.237	0.027	7.291	0.349	90.824	0.094	0.000	0.050	0.000	0.000	98.90
weath4-9	83	0.035	0.201	0.052	7.396	0.353	91.166	0.073	0.000	0.025	0.006	0.000	99.31
weath4-4	78	0.039	0.200	0.131	7.158	0.356	90.451	0.138	0.000	0.000	0.033	0.000	98.51
weath4-13	87	0.023	0.254	0.021	7.359	0.357	91.174	0.113	0.000	0.083	0.081	0.000	99.47
weath4-7	81	0.024	0.200	0.067	7.184	0.359	91.372	0.113	0.000	0.061	0.000	0.000	99.38
weath4-10	84	0.019	0.246	0.038	7.322	0.360	91.571	0.096	0.000	0.102	0.072	0.000	99.83
weath6-11	41	0.023	0.321	0.000	6.288	0.383	92.359	0.196	0.047	0.108	0.117	0.000	99.84

weath2-13	73	0.040	0.388	0.005	5.377	0.383	93.175	0.252	0.073	0.127	0.021	0.000	99.84
weath8-14	16	0.038	0.292	0.010	6.444	0.390	91.271	0.429	0.000	0.132	0.214	0.000	99.22

Table B-6. EPMA analyses of sulfides in CBb HH 237 (wt.%)														
	Line Numbers	Line	Si	P	S	Ni	Co	Fe	Cr	Mn	Cu	Zn	V	Totals
Exsolved Sulfides	Un 2 HaH_G19_S1	25	0.00	0.00	38.35	0.22	0.01	50.00	10.01	0.09	0.00	0.00	0.82	99.48
	Un 3 HaH_G19_S2	26	0.00	0.00	43.53	0.09	0.01	24.75	29.79	0.29	0.00	0.03	0.63	99.10
	Un 4 HaH_G19_S3	27	0.00	0.00	41.76	0.11	0.00	28.32	26.85	0.22	0.00	0.00	0.83	98.10
	Un 5 HaH_G19_S4	28	0.00	0.02	40.48	0.85	0.02	32.32	24.46	0.22	0.00	0.00	0.62	99.00
	Un 21 HaH_G9_S1	44	0.04	0.02	38.48	0.23	0.02	45.10	15.46	0.24	0.02	0.00	0.33	99.94
	Un 22 HaH_G9_S2	45	0.00	0.09	36.95	0.73	0.03	44.46	16.33	0.17	0.02	0.00	0.39	99.17
	Un 23 HaH_G9_S3	46	0.00	0.05	29.38	2.36	0.07	46.23	16.52	0.18	0.00	0.00	0.35	95.12
	Un 26 HaH_G8_S1	49	0.00	0.00	37.69	0.23	0.00	48.81	11.98	1.43	0.05	0.04	0.23	100.48
	Un 27 HaH_G8_S2	50	0.00	0.02	35.66	0.55	0.04	54.34	8.17	1.00	0.12	0.00	0.38	100.29
	Un 31 HaH_G28_S1	54	0.00	0.03	30.21	0.99	0.06	47.33	15.20	0.19	0.13	0.00	0.21	94.35
	Un 36 HaH_G23_S1	59	0.00	0.06	38.38	0.53	0.02	37.36	21.92	0.18	0.00	0.01	0.59	99.04
	Un 37 HaH_G23_S2	60	0.00	0.02	38.85	0.21	0.00	37.46	20.38	0.19	0.00	0.00	0.77	97.89
	Un 39 HaH_G23_S4	62	0.00	0.12	29.31	2.44	0.10	50.31	16.66	0.11	0.00	0.00	0.61	99.66
	Un 3 G19_S1 exsolution	27	0.00	0.05	32.37	2.14	0.11	51.09	15.09	0.13	0.00	0.00	0.68	101.66
	Un 4 HaH_G19_S2 exsolution	28	0.02	0.04	37.89	1.21	0.00	44.48	15.91	0.10	0.00	0.00	0.55	100.20
	Un 5 HaH_G19_S5 L exsolution	29	0.00	0.01	37.24	0.45	0.02	50.97	9.80	0.07	0.00	0.00	0.78	99.36
	Un 6 HaH_G19_S5 D exsolution	30	0.00	0.00	41.67	0.11	0.00	32.56	24.17	0.24	0.01	0.24	0.62	99.61
	Un 8 HaH_G19_S3	31	0.00	0.07	31.31	1.73	0.08	49.98	15.93	0.12	0.00	0.00	0.68	99.89
	Un 9 HaH_G19_S4	32	0.00	0.03	36.45	0.86	0.00	54.68	7.56	0.11	0.03	0.06	0.37	100.16
	Un 10 HaH_G19_S6 D exsolution	33	0.04	0.03	40.84	0.18	0.00	34.76	21.93	0.21	0.00	0.16	0.76	98.91
	Un 12 HaH_G19_7 exsolution	35	0.00	0.01	37.48	0.92	0.05	38.58	21.51	0.19	0.00	0.04	0.69	99.47
Homogeneous Sulfides	Un 16 HaH_G14_S1	39	0.00	0.01	37.05	0.23	0.00	52.41	8.31	0.31	0.02	0.00	0.11	98.46
	Un 18 HaH_G15_S1	41	0.00	0.01	37.15	0.20	0.03	59.60	3.40	0.05	0.00	0.00	0.13	100.56
	Un 19 HaH_G15_S2	42	0.00	0.06	35.89	0.96	0.05	62.19	1.96	0.00	0.01	0.00	0.08	101.21
	Un 28 HaH_G8_S3	51	0.00	0.03	36.79	0.57	0.02	54.83	7.61	0.67	0.10	0.00	0.12	100.75
	Un 34 HaH_G25_S2	57	0.01	0.01	37.00	0.23	0.01	60.38	3.14	0.05	0.01	0.00	0.08	100.91
Hom. w. Blebs	Un 6 HaH_G19_S5	29	0.00	0.00	37.99	0.20	0.00	53.04	8.16	0.10	0.00	0.00	0.40	99.88
	Un 10 HaH_G20_S1	33	0.01	0.03	36.14	0.39	0.01	62.22	1.85	0.04	0.14	0.00	0.02	100.83
	Un 11 HaH_G20_S2	34	0.00	0.00	36.31	0.29	0.02	62.21	1.83	0.03	0.03	0.01	0.03	100.76

Un 13 HaH_G17_S1	36	0.00	0.00	37.60	0.26	0.02	60.19	2.43	0.08	0.00	0.00	0.07	100.66
Un 14 HaH_G17_S2	37	0.00	0.00	37.17	0.19	0.02	60.71	2.37	0.06	0.00	0.00	0.06	100.58
Un 29 HaH_G8_S4	52	0.00	0.00	32.61	1.05	0.07	62.42	4.75	0.35	0.02	0.00	0.07	101.35
Un 33 HaH_G25_S1	56	0.33	0.00	36.62	0.24	0.00	59.26	3.14	0.05	0.00	0.05	0.08	99.76

Table B-7. EPMA analyses of metal in CBb HH 237 (wt.%)													
Line Numbers	**Line**	**Si**	**P**	**S**	**Ni**	**Co**	**Fe**	**Cr**	**Mn**	**Cu**	**Zn**	**V**	**Totals**
Un 14 HaH_G19_M2	37.000	0.034	0.328	0.002	8.309	0.266	91.290	0.369	0.000	0.000	0.000	0.013	100.61
Un 15 HaH_G19_M3	38.000	0.036	0.447	0.000	6.177	0.293	92.918	0.410	0.000	0.000	0.000	0.000	100.28
Un 18 HaH_G22_M1	41.000	0.000	0.301	0.011	6.839	0.306	93.163	0.068	0.000	0.000	0.000	0.000	100.69
Un 20 HaH_G22_M2	43.000	0.020	0.286	0.003	6.679	0.281	93.076	0.096	0.000	0.000	0.071	0.000	100.51
Un 26 HaH_G23_M1	49.000	0.055	0.376	0.176	6.678	0.307	92.537	0.351	0.000	0.000	0.000	0.002	100.48
Un 28 HaH_G23_M3	51.000	0.041	0.366	0.119	6.725	0.260	92.796	0.365	0.000	0.000	0.000	0.000	100.67
Un 35 HaH_G24_M1	58.000	0.017	0.312	0.000	6.695	0.282	94.187	0.086	0.000	0.000	0.008	0.017	101.60
Un 36 HaH_G24_M2	59.000	0.004	0.306	0.001	6.693	0.285	93.459	0.074	0.000	0.000	0.125	0.000	100.95
Un 42 HaH_G9_M1	65.000	0.028	0.347	0.030	5.819	0.305	94.347	0.111	0.000	0.036	0.000	0.000	101.02
Un 43 HaH_G9_M2	66.000	0.064	0.320	0.784	5.914	0.278	92.506	0.506	0.000	0.000	0.000	0.024	100.40
Un 48 HaH_G6_M1	71.000	0.005	0.365	1.223	6.567	0.289	91.796	0.260	0.000	0.000	0.000	0.000	100.50
Un 49 HaH_G6_M2	72.000	0.018	0.376	0.003	6.383	0.311	93.458	0.183	0.008	0.085	0.065	0.007	100.90
Un 54 HaH_G8_M1	77.000	0.019	0.273	0.123	5.808	0.267	92.543	0.336	0.001	0.000	0.030	0.000	99.40
Un 55 HaH_G8_M2	78.000	0.007	0.347	0.000	5.803	0.282	93.611	0.325	0.000	0.000	0.068	0.003	100.45
Un 56 HaH_G8_M3	79.000	0.000	0.352	0.006	5.665	0.251	93.871	0.271	0.000	0.007	0.000	0.003	100.43
Un 61 HaH_G28_M1	84.000	0.009	0.290	1.150	6.642	0.299	91.460	0.564	0.000	0.000	0.000	0.008	100.42
Un 62 HaH_G28_M2	85.000	0.019	0.418	0.753	6.068	0.308	93.125	0.301	0.000	0.000	0.109	0.000	101.10
Un 63 HaH_G28_M3	86.000	0.029	0.323	0.009	6.488	0.295	93.573	0.217	0.000	0.014	0.000	0.011	100.96
Un 8 HaH_G19_M1	31.000	0.052	0.414	0.001	5.782	0.292	93.605	0.314	0.000	0.000	0.000	0.003	100.46
Un 9 HaH_G19_M2	32.000	0.038	0.367	0.003	6.144	0.283	93.282	0.381	0.000	0.000	0.000	0.007	100.50
Un 12 HaH_G20_M1	35.000	0.000	0.372	0.008	6.061	0.303	94.761	0.105	0.000	0.000	0.000	0.002	101.61
Un 15 HaH_G17_M1	38.000	0.036	0.352	0.000	5.934	0.267	94.106	0.203	0.000	0.000	0.000	0.003	100.90
Un 17 HaH_G14_M1	40.000	0.002	0.204	0.002	6.044	0.294	94.233	0.117	0.000	0.000	0.000	0.000	100.90
Un 20 HaH_G15_M1	43.000	0.023	0.253	0.000	5.981	0.301	94.100	0.178	0.002	0.000	0.000	0.000	100.84
Un 24 HaH_G9_M1	47.000	0.044	0.295	0.013	4.826	0.319	95.763	0.123	0.000	0.000	0.000	0.012	101.39
Un 25 HaH_G9_M2	48.000	0.064	0.365	0.003	5.677	0.284	94.804	0.123	0.000	0.000	0.000	0.000	101.32
Un 30 HaH_G8_M1	53.000	0.016	0.310	0.006	5.369	0.286	94.767	0.326	0.000	0.000	0.000	0.001	101.08
Un 32 HaH_G28_M1	55.000	0.022	0.232	0.001	6.441	0.316	93.930	0.070	0.000	0.000	0.000	0.003	101.02
Un 35 HaH_G25_M1	58.000	0.006	0.365	0.010	5.864	0.279	94.952	0.144	0.000	0.000	0.000	0.013	101.63
Un 40 HaH_G23_M1	63.000	0.033	0.306	0.009	6.264	0.311	93.835	0.242	0.000	0.000	0.000	0.000	101.00

Table B-8. EPMA analyses of sulfides in CBb QUE 94411 (wt.%)														
	Line Numbers	**Line**	**Si**	**P**	**S**	**Ni**	**Co**	**Fe**	**Cr**	**Mn**	**Cu**	**Zn**	**V**	**Totals**
Homogeneous Sulfides	Un 25 M11_sulfide1	49	0.01	0.02	33.05	0.69	0.05	63.82	2.14	0.03	0.09	0.00	0.00	99.89
	Un 26 M11_sulfide2	50	0.01	0.04	32.27	0.96	0.03	64.15	2.08	0.02	0.00	0.00	0.00	99.55
	Un 27 M11_sulfide3	51	0.01	0.01	36.39	0.24	0.05	61.51	1.92	0.04	0.17	0.00	0.00	100.34
	Un 28 M11_sulfide4	52	0.01	0.10	26.49	2.22	0.11	70.60	1.58	0.02	0.00	0.00	0.00	101.12
	Un 29 M11_sulfide5	53	0.01	0.13	20.18	3.40	0.15	76.01	1.11	0.01	0.00	0.00	0.00	100.99
	Un 31 M11_sulfide7	55	0.01	0.11	23.31	2.96	0.13	74.09	1.34	0.01	0.02	0.01	0.00	102.00
	Un 37 M12_sulfide1	61	1.16	0.02	33.76	0.70	0.02	58.93	3.33	0.10	0.02	0.00	0.00	98.04
	Un 37 M12_sulfide1	62	0.52	0.04	33.89	0.79	0.05	59.57	3.42	0.11	0.00	0.00	0.00	98.38
	Un 38 M12_sulfide2	63	0.00	0.03	36.08	0.25	0.02	59.84	3.45	0.09	0.00	0.03	0.00	99.77
	Un 39 M12_sulfide3	64	0.01	0.02	34.62	0.88	0.02	61.42	3.26	0.10	0.00	0.06	0.00	100.38
	Un 40 M12_sulfide4	65	0.00	0.03	33.17	1.06	0.04	63.23	3.11	0.10	0.00	0.00	0.00	100.75
	Un 41 M12_sulfide5	66	0.01	0.02	33.90	0.92	0.03	61.69	3.15	0.08	0.00	0.00	0.00	99.81
	Un 45 M12_sulfide6	70	0.01	0.01	33.49	1.18	0.06	61.68	3.36	0.11	0.01	0.12	0.00	100.03
	Un 46 M12_sulfide7	71	0.00	0.04	34.59	0.80	0.02	62.01	3.08	0.09	0.01	0.00	0.00	100.64
	Un 47 M12_sulfide8	72	0.01	0.03	34.41	0.91	0.02	61.73	3.13	0.08	0.03	0.02	0.00	100.37
	Un 52 M13_sulfide1	77	0.01	0.06	33.51	0.50	0.03	59.13	2.46	0.04	0.00	0.04	0.00	95.78
	Un 53 M13_sulfide2	78	0.00	0.00	35.46	0.32	0.05	60.65	3.07	0.04	0.00	0.00	0.00	99.60
	Un 54 M13_sulfide3	79	0.00	0.01	36.43	0.30	0.02	60.86	2.56	0.02	0.00	0.00	0.00	100.20
	Un 55 M13_sulfide4	80	0.00	0.01	35.35	0.39	0.04	60.52	2.48	0.08	0.00	0.00	0.00	98.88
	Un 56 M13_sulfide5	81	0.00	0.00	36.18	0.40	0.02	60.31	2.61	0.02	0.17	0.00	0.00	99.70
	Un 61 M20_sulfide1	86	0.24	0.10	17.90	3.55	0.16	76.63	2.36	0.02	0.00	0.00	0.00	100.96
	Un 67 M14_sulfide1	92	0.00	0.05	33.22	1.00	0.03	62.68	3.02	0.08	0.00	0.00	0.00	100.07
	Un 68 M14_sulfide2	93	0.00	0.02	35.82	0.40	0.02	61.06	3.06	0.07	0.00	0.00	0.00	100.46
	Un 69 M14_sulfide3	94	0.00	0.01	35.34	0.63	0.00	60.76	3.04	0.09	0.01	0.01	0.00	99.88

Un 70	M14_sulfide4	95	0.00	0.01	36.19	0.29	0.03	59.90	3.21	0.06	0.02	0.00	0.00	99.71
Un 71	M14_sulfide5	96	0.00	0.03	34.78	0.58	0.03	61.84	3.12	0.07	0.05	0.06	0.00	100.55
Un 72	M14_sulfide6	97	0.00	0.05	29.08	1.73	0.10	67.45	2.38	0.07	0.00	0.09	0.00	100.96
Un 78	M15_sulfide1	103	0.01	0.02	33.98	1.22	0.01	61.56	3.19	0.10	0.00	0.00	0.00	100.08
Un 79	M15_sulfide2	104	0.03	0.04	32.39	0.61	0.01	58.34	3.22	0.07	0.00	0.01	0.00	94.73
Un 81	M15_sulfide3	106	0.00	0.01	36.12	0.37	0.00	59.65	3.74	0.05	0.04	0.17	0.00	100.16
Un 82	M15_sulfide4	107	0.00	0.00	36.73	0.25	0.02	59.13	3.90	0.08	0.00	0.12	0.00	100.22
Un 83	M15_sulfide5	108	0.00	0.00	35.79	0.44	0.02	59.77	3.51	0.07	0.00	0.07	0.00	99.69
Un 89	M16_sulfide1	114	0.00	0.01	35.46	0.31	0.02	60.30	3.50	0.08	0.00	0.00	0.00	99.69
Un 90	M16_sulfide2	115	0.00	0.00	36.31	0.25	0.02	59.46	3.50	0.13	0.00	0.00	0.00	99.67
Un 91	M16_sulfide3	116	0.01	0.01	36.53	0.22	0.00	61.27	2.24	0.05	0.08	0.00	0.00	100.41
Un 92	M16_sulfide4	117	0.00	0.03	34.87	0.68	0.00	61.05	3.54	0.10	0.00	0.00	0.00	100.27
Un 93	M16_sulfide5	118	0.01	0.01	36.30	0.22	0.03	59.09	3.78	0.09	0.00	0.00	0.00	99.53
Un 94	M16_sulfide6	119	0.01	0.02	34.16	0.72	0.03	61.32	3.12	0.09	0.08	0.00	0.00	99.56
Un 100	M17_sulfide1	125	0.00	0.00	36.33	0.29	0.01	59.81	3.72	0.11	0.04	0.11	0.00	100.43
Un 101	M17_sulfide2	126	0.01	0.01	36.29	0.27	0.03	59.79	3.49	0.10	0.00	0.07	0.00	100.05
Un 102	M17_sulfide3	127	0.00	0.02	35.29	0.60	0.02	58.13	5.35	0.22	0.00	0.00	0.00	99.63
Un 103	M17_sulfide4	128	0.00	0.00	36.87	0.22	0.05	54.08	7.39	0.59	0.00	0.00	0.00	99.20
Un 104	M17_sulfide6	129	0.01	0.01	35.30	0.37	0.05	57.89	4.38	0.18	0.00	0.00	0.00	98.20
Un 105	M17_sulfide7	130	0.01	0.00	36.19	0.25	0.00	58.82	4.03	0.14	0.00	0.00	0.00	99.43
Un 106	M17_sulfide8	131	0.00	0.00	36.13	0.25	0.00	59.02	4.08	0.14	0.00	0.20	0.00	99.81
Un 107	M17_sulfide5	132	0.00	0.00	37.04	0.26	0.01	56.62	5.80	0.32	0.00	0.02	0.00	100.06
Un 43	QUE_G12_S2	66	0.01	0.01	36.87	0.31	0.03	60.55	3.23	0.12	0.00	0.00	0.08	101.21
Un 53	QUE_G12_S1	76	0.00	0.01	37.10	0.25	0.01	60.07	3.13	0.10	0.02	0.04	0.07	100.80
Un 55	QUE_G12_S3	78	0.00	0.00	37.05	0.30	0.00	60.01	3.30	0.12	0.00	0.00	0.07	100.85
Un 56	QUE_G12_S4	79	0.00	0.00	36.87	0.28	0.00	59.74	3.50	0.11	0.00	0.00	0.11	100.60

	Un 44 QUE_G13_S1	67	0.00	0.00	37.16	0.23	0.01	60.72	2.57	0.03	0.05	0.01	0.05	100.83
	Un 45 QUE_G13_S2	68	0.00	0.02	35.21	0.52	0.03	62.22	2.42	0.03	0.00	0.01	0.04	100.51
	Un 58 QUE_G13_S3	81	0.00	0.01	36.72	0.28	0.01	61.12	2.77	0.04	0.00	0.00	0.06	101.00
	Un 59 QUE_G13_S4	82	0.00	0.01	36.43	0.29	0.00	60.63	3.06	0.05	0.00	0.00	0.05	100.53
	Un 46 QUE_G1_S2	69	0.00	0.01	35.86	0.31	0.03	62.36	2.02	0.02	0.00	0.00	0.03	100.65
	Un 62 QUE_G1_S1	85	0.00	0.02	34.17	0.60	0.04	63.87	1.88	0.01	0.00	0.00	0.03	100.64
	Un 47 QUE_G2_S3	70	0.00	0.00	35.30	0.62	0.02	59.86	4.17	0.38	0.15	0.01	0.04	100.55
	Un 65 QUE_G2_S1	88	0.00	0.02	34.72	0.66	0.00	60.27	4.05	0.35	0.06	0.03	0.04	100.20
	Un 66 QUE_G2_S2	89	0.00	0.03	34.51	0.57	0.03	58.57	5.41	0.52	0.05	0.00	0.08	99.76
	Un 48 QUE_G3_S1	71	0.00	0.00	37.83	0.28	0.01	51.26	9.10	1.09	0.36	0.00	0.14	100.10
	Un 49 QUE_G3_S2	72	0.00	0.00	38.38	0.28	0.01	47.44	11.93	1.00	0.61	0.04	0.16	99.85
	Un 69 QUE_G3_S3	92	0.00	0.01	38.69	0.27	0.02	48.56	11.04	0.85	0.79	0.00	0.13	100.36
	Un 70 QUE_G3_S4	93	0.00	0.01	38.44	0.28	0.04	48.36	11.03	0.98	0.83	0.00	0.16	100.13
	Un 71 QUE_G3_S5	94	0.00	0.01	38.10	0.30	0.02	49.99	9.81	1.20	0.48	0.04	0.13	100.07
	Un 50 QUE_G4_S2	73	0.00	0.01	36.11	0.29	0.01	61.28	2.18	0.03	0.16	0.00	0.02	100.10
	Un 74 QUE_G4_S1	99	0.00	0.07	34.41	0.46	0.03	64.03	2.17	0.04	0.11	0.02	0.01	101.36
	Un 51 QUE_G5_S1	74	0.00	0.01	36.63	0.26	0.00	61.00	2.07	0.02	0.00	0.02	0.02	100.03
	Un 76 QUE_G5_S2	101	0.05	0.08	32.38	0.96	0.02	59.49	2.26	0.05	0.00	0.03	0.03	95.35
	Un 52 QUE_G6_S1	75	0.00	0.01	35.48	0.35	0.01	61.11	2.40	0.03	0.04	0.00	0.06	99.49
	Un 79 QUE_G6_S1	104	0.00	0.02	36.19	0.48	0.02	61.36	2.37	0.03	0.07	0.00	0.06	100.60
	Un 80 QUE_G6_S2	105	0.01	0.01	37.00	0.18	0.01	61.36	2.16	0.02	0.02	0.00	0.06	100.82
	Un 81 QUE_G6_S3	106	0.00	0.03	30.65	2.06	0.07	65.97	2.64	0.02	0.01	0.00	0.06	101.52
Homogeneous w. Metal Blebs	Un 25 M11_sulfide1	49	0.01	0.02	33.05	0.69	0.05	63.82	2.14	0.03	0.09	0.00	0.00	99.89
	Un 26 M11_sulfide2	50	0.01	0.04	32.27	0.96	0.03	64.15	2.08	0.02	0.00	0.00	0.00	99.55
	Un 27 M11_sulfide3	51	0.01	0.01	36.39	0.24	0.05	61.51	1.92	0.04	0.17	0.00	0.00	100.34
	Un 28 M11_sulfide4	52	0.01	0.10	26.49	2.22	0.11	70.60	1.58	0.02	0.00	0.00	0.00	101.12

Un	29	M11_sulfide5	53	0.01	0.13	20.18	3.40	0.15	76.01	1.11	0.01	0.00	0.00	0.00	100.99
Un	31	M11_sulfide7	55	0.01	0.11	23.31	2.96	0.13	74.09	1.34	0.01	0.02	0.01	0.00	102.00
Un	67	M14_sulfide1	92	0.00	0.05	33.22	1.00	0.03	62.68	3.02	0.08	0.00	0.00	0.00	100.07
Un	68	M14_sulfide2	93	0.00	0.02	35.82	0.40	0.02	61.06	3.06	0.07	0.00	0.00	0.00	100.46
Un	69	M14_sulfide3	94	0.00	0.01	35.34	0.63	0.00	60.76	3.04	0.09	0.01	0.01	0.00	99.88
Un	70	M14_sulfide4	95	0.00	0.01	36.19	0.29	0.03	59.90	3.21	0.06	0.02	0.00	0.00	99.71
Un	71	M14_sulfide5	96	0.00	0.03	34.78	0.58	0.03	61.84	3.12	0.07	0.05	0.06	0.00	100.55
Un	72	M14_sulfide6	97	0.00	0.05	29.08	1.73	0.10	67.45	2.38	0.07	0.00	0.09	0.00	100.96
Un	78	M15_sulfide1	103	0.01	0.02	33.98	1.22	0.01	61.56	3.19	0.10	0.00	0.00	0.00	100.08
Un	79	M15_sulfide2	104	0.03	0.04	32.39	0.61	0.01	58.34	3.22	0.07	0.00	0.01	0.00	94.73
Un	81	M15_sulfide3	106	0.00	0.01	36.12	0.37	0.00	59.65	3.74	0.05	0.04	0.17	0.00	100.16
Un	82	M15_sulfide4	107	0.00	0.00	36.73	0.25	0.02	59.13	3.90	0.08	0.00	0.12	0.00	100.22
Un	83	M15_sulfide5	108	0.00	0.00	35.79	0.44	0.02	59.77	3.51	0.07	0.00	0.07	0.00	99.69

Table B-9. EPMA analyses of metal in CBb QUE 94411 (wt.%)													
Line Numbers	**Line**	**Si**	**P**	**S**	**Ni**	**Co**	**Fe**	**Cr**	**Mn**	**Cu**	**Zn**	**V**	**Total**
Un 42 QUE_G12_M1	65	0.009	0.309	0.003	5.604	0.287	95.068	0.166	0.000	0.005	0.000	0.001	101.45
Un 54 QUE_G12_M1	77	0.000	0.321	0.013	5.553	0.264	95.035	0.159	0.000	0.000	0.000	0.000	101.35
Un 57 QUE_G12_M2	80	0.008	0.226	0.004	5.631	0.282	94.746	0.171	0.000	0.000	0.000	0.000	101.07
Un 60 QUE_G13_M1	83	0.015	0.327	0.027	5.927	0.289	94.974	0.117	0.000	0.022	0.000	0.000	101.70
Un 61 QUE_G13_M2	84	0.006	0.322	0.007	5.931	0.290	94.842	0.116	0.000	0.000	0.000	0.004	101.52
Un 63 QUE_G1_M1	86	0.000	0.256	0.269	6.821	0.312	93.429	0.123	0.000	0.000	0.000	0.001	101.21
Un 64 QUE_G1_M2	87	0.000	0.285	0.011	6.366	0.312	94.449	0.107	0.000	0.000	0.000	0.000	101.53
Un 67 QUE_G2_M1	90	0.006	0.401	0.000	5.051	0.280	95.600	0.173	0.000	0.024	0.000	0.000	101.54
Un 68 QUE_G2_M2	91	0.001	0.472	0.014	5.062	0.265	95.288	0.196	0.002	0.029	0.000	0.000	101.33
Un 72 QUE_G3_M1	95	0.000	1.560	0.000	6.750	0.314	92.367	0.043	0.001	0.282	0.000	0.014	101.33
Un 73 QUE_G3_M2	96	0.003	1.552	0.011	7.030	0.310	92.333	0.040	0.000	0.180	0.000	0.002	101.46
Un 73 QUE_G3_M2	97	0.006	1.287	0.034	6.692	0.285	92.660	0.165	0.004	0.191	0.000	0.000	101.32
Un 73 QUE_G3_M2	98	0.009	1.301	0.032	6.672	0.303	93.056	0.174	0.000	0.180	0.000	0.000	101.73
Un 75 QUE_G4_M1	100	0.008	0.265	0.001	5.103	0.256	95.637	0.129	0.000	0.000	0.000	0.004	101.40
Un 77 QUE_G5_M1	102	0.000	0.326	0.002	5.173	0.252	95.447	0.085	0.000	0.000	0.000	0.010	101.30
Un 78 QUE_G5_M2	103	0.000	0.345	0.023	5.315	0.267	95.457	0.070	0.000	0.000	0.000	0.008	101.48
Un 82 QUE_G6_M1	107	0.000	0.241	0.005	5.650	0.266	95.958	0.110	0.000	0.000	0.000	0.000	102.23
Un 83 QUE_G6_M2	108	0.005	0.237	0.002	5.605	0.281	94.916	0.101	0.000	0.000	0.000	0.010	101.16
Un 85 QUE_G8_M1	110	0.003	0.108	0.003	6.240	0.328	94.403	0.096	0.000	0.000	0.000	0.000	101.18
Un 86 QUE_G9_M1	111	0.000	0.207	0.006	6.164	0.287	94.623	0.097	0.000	0.000	0.000	0.006	101.39
Un 84 QUE_G7_M1	109	0.004	0.182	0.000	9.239	0.417	91.212	0.151	0.000	0.000	0.000	0.005	101.21

Table B-10. EPMA analyses of metal blebs in CBa Gujba and CBb HH 237 (wt.%)													
Line Numbers	**Line**	**Si**	**P**	**S**	**Ni**	**Co**	**Fe**	**Cr**	**Mn**	**Cu**	**Zn**	**V**	**Total**
Un 86 Gujba_Grain11_Sulfide5_Metal glob	157	0.000	0.332	0.160	6.914	0.274	91.636	0.437	0.000	0.000	0.000	0.011	99.76
Un 11 GujbaBruker_G16_S5_metal globule	33	0.022	0.005	0.162	3.386	0.105	96.791	0.466	0.008	0.000	0.000	0.000	100.95
Un 27 GujbaBruker_G8_S2_metal globule	48	0.010	0.313	0.335	10.297	0.323	88.652	0.614	0.004	0.029	0.000	0.004	100.58
Un 7 HaH_G19_MB1	30	0.033	0.207	0.111	5.642	0.314	94.474	0.475	0.000	0.000	0.000	0.024	101.28

References

Adams, F. C. (2010). The birth environment of the solar system. *Annual Review of Astronomy and Astrophysics,* **48**, 47—85.

Amelin Y., Krot A., Twelker E. (2004). Pb isotopic age of the CB chondrite Gujba, and the duration of the chondrule formation interval. *Geochimica Cosmochimica Acta,* **68** (Suppl.), A759.

Amelin, Y., Krot, A. N. (2005). Young Pb-isotopic ages of chondrules in CB carbonaceous chondrites. *LSPC XXXVI,* Abst # 1247.

Amelin, Y., Krot, A. N., Hutcheon, I. D., Ulyanov, A. A. (2002). Lead isotopic ages of chondrules and calcium-aluminum–rich inclusions. *Science*, **297**, 1678 – 1683.

Bevan, A. W. R., Kinder, J., Axon, H. J. (1981). Complex shock-induced Fe-Ni-S-Cr-C melts in the Haig (IIIA) iron meteorite. *Meteoritics*, **16***(3)*, 261 – 267.

Bonal, L., Huss, G. R., Krot, A. N., Nagashima, K., Ishii, H. A., and Bradley, J. P. (2010). Highly 15N-enriched chondritic clasts in the CB/CH-like meteorite Isheyevo. *Geochimica Cosmochimica Acta*, **74**, 6590-6609.

Boss, A. P., Ipatov, S. I., Keiser, S. A., Myhill, E. A., Vanhala, H. A. T. (2008). Simultaneous triggered collapse of the presolar dense cloud core and injection of short-lived radioisotopes by a supernova shock wave. *The Astrophysical Journal,* **686**, 119 – 122.

Brearley, A. J., Jones, R. H. (1998). Chondritic meteorites. *Reviews in Mineralogy and Geochemistry,* **36**, 3.1 – 3.398.

Campbell, A. J., Humayun, M., Weisberg, M. K. (2005b) Compositions of unzoned and zoned metal in the CBb chondrites Hammadah al Hamra 237 and Queen Alexandra Range 94267, *Meteoritics and Planetary Science*, **40**, 1131–1148.

Campbell, A. J., Humayun, M., Weisberg, M. K., (2002). Siderophile element constraints on the formation of metal in the metal-rich chondrites Bencubbin, Weatherford,

and Gujba. *Geochimica Cosmochimica Acta*, **66***(4)*, 647 – 660.

Campbell, A. J., Zanda, B., Perron, C., Meibom, A., Petaev, M. I. (2005a). Origin and thermal history of Fe-Ni metal in primitive chondrites. *ASP Conference Series*, **341**, 407 – 431.

Chappell, H. M., Jones, R. H., Goldstein, J. I. (2011). Interaction between impact melt matrix and metal particles in the Weatherford CBa meteorite. *Meteoritical Society Meeting 74*, Abst 5168.

Chikami J., El Goresy, A., Janicke, J. (1998). Chemical zoning profiles of daubreelite in enstatite chondrites. *Meteoritics and Planetary Science*, **33***(4)*, A31.

Clayton, R. N. (1993). Oxygen isotopes in meteorites. *Annual Review in Earth and Planetary Sciences*, **21**, 115–49

Clayton, R. N. (2003). Oxygen isotopes in meteorites. *Treatise on Geochemistry.* Vol. 1. University of Chicago: Elsevier Ltd.. pp. 129-142.

Clayton, R. N., and Mayeda, T. K. (1999). Oxygen isotope studies of carbonaceous chondrites. *Geochimica Cosmochimica Acta*, **63**, 2089-2104.

Dauphas, N., Chaussidon, M. (2011). A perspective from extinct radionuclides on a young stellar object: The Sun and its accretion disk. *Annual Review in Earth and Planetary Science*, **39**, 351-386.

Davidson, T. M., Collins, G. S., and Ciesla, F. J. (2010). Numerical modelling of heating in porous planetesimal collisions. *Icarus*, **208**, 468-481.

Desch S. (2006). How to make a chondrule. *Nature*, **441**, 416–17.

Ebel, D. S. (2006). Condensation of rocky material in astrophysical environments. In Lauretta DS, McSween HY Jr. (Eds). *Meteorites and the Early Solar System II*.

Tucson: The University of Arizona Press, pp. 567 – 586.

El Goresy, A., & Kullerud, G. (1969). Phase relations in the system Cr-Fe-S. In P. Millman (Ed.), *Meteorite Research*. Dordrecht, Holland: D. Reidel Publishing Company, pp. 638 – 656.

Fedkin, A. K., and Grossman, L. (2006). The fayalite content of chondritic olivine: Obstacle to understanding the condensation of rocky material. In Lauretta DS, McSween HY Jr. (Eds). *Meteorites and the Early Solar System II*. Tucson: The University of Arizona Press, pp. 567 – 586.

Fedkin, A. V., Grossman, L., Campbell, A. J., and Humayun, M. (2013). CB chondrites could have formed in an impact plume. *LPSC XLIV*, Abst 2309.

Franchi, I. A., Wright, I. P. and Pillinger, C. T. (1986) Heavy nitrogen in Bencubbin – A light element isotopic anomaly in stony-iron meteorite. *Nature*, **323**, 138–140.

Goldstein, J. I., Jones, R. H., Kotula, P. G., Michael, J. R. (2007). Microstructure and thermal history of metal particles in CH chondrites. *Meteoritics and Planetary Science*, **42***(6)*, 913 – 933.

Goldstein, J. I., Jones, R. H., Kotula, P. G., Michael, J. R. (2011). Thermal history of metal particles in CB chondrites. *74th Annual Meeting of the Meteoritical Society*, Abst #5067.

Grady, M. M. and Pillinger, C. T. (1990) ALH 85085 — nitrogen isotope analysis of a highly unusual primitive chondrite. *Earth and Planetary Science Letters*, **97**, 29–40.

Grossman, L. 1972. Condensation in the primitive solar nebula. *Geochimica et Cosmochimica Acta*, **36**, 597–619.

Grossman, L., Larimer, J. W. (1974). Early chemical history of the solar system. *Review of Geophysics*, **12**, 71—101.

Haisch, K. E. Jr, Lada, E. A., Lada, C. J. (2001). Disk frequencies and lifetimes in young clusters. *Astrophysical Journal*, **553**, L153 – 156.

Huss, G. R., Rubin, A. E., Grossman, J. N. (2006). Thermal metamorphism in chondrites. In Lauretta DS, McSween HY Jr. (Eds). *Meteorites and the Early Solar System II*. Tucson: The University of Arizona Press, pp. 567 – 586.

Ivanova, M. A., Kononkova, N. N., Krot, A. N., Greenwood, R. C., Franchi, I. A., Verchovsky, A. B., Trieloff, M., Korochantseva, E. V. and Branstatter, F. (2008) The Isheyevo meteorite: mineralogy, petrology, bulk chemistry, oxygen, nitrogen, and carbon isotopic composition and 40Ar–39Ar ages. *Meteoritics and Planetary Science*, **43**, 915–940.

Kallemeyn, G. W., Rubin, A. E., Wasson, J. T. (2001) Compositional studies of Bencubbin dark silicate host and an OC clast: Relationships to other meteorites and implications for their origin. *LPSC XXXII*, Abst #2070.

Keeling, D. L., and Marti, K. (1987). Nitrogen anomalies in Weatherford metal clasts. *Meteoritics*, **22**, 426-427.

Keil, K. (1968). Mineralogical notes: Zincian daubreelite from the Kota-Kota and St. Mark's enstatite chondrites. *The American Mineralogist*, **53**, 491 – 494.

Kelly, S. and Turner, G. 1987. Laser probe 40Ar-39Ar investigation of the polymict breccia Bencubbin. *Meteoritics*, **22**, 427.

Kita, N.T., Huss, G.R., Tachibana, S., Amelin, Y., Nyquist, L.E., Hutcheon, I.D. (2005). Constraints on the origin of chondrules and CAIs from short-lived and long-lived radionuclides. In Chondrites and the Protoplanetary Disk. *Astronomical Society of the Pacific Conference Series*, **341**, 558–587.

Klein, T., Touboul, M., Bourdon, B., Nimmo, F., Mezger, K., Palme, H., Jacobsen, S. B., Yin, Q., Halliday, A. N. (2009). Hf-W chronology of the accretion and early evolution of asteroids and terrestrial planets. *Geochimica et Cosmochimica Acta*, **73**, 5150–5188.

Kornacki, A. S., and Fegley, B. (1984). Origin of spinel-rich chondrules and inclusions in carbonaceous and ordinary chondrites. *Proc. 14th Lunar Planet. Sci. Conf., J. Geophysics. Res.*, **89**, B588-B596.

Krot, A. N., Amelin, Y., Cassen, P., Meibom, A. (2005). Young chondrules in CB chondrites from a giant impact in the early Solar System. *Nature*, **436**, 989 – 992.

Krot, A. N., Libourel, G., Goodrich, C. A., Petaev, M. I. (2004). Silica-rich igneous rims around magnesian chondrules in CR carbonaceous chondrites: evidence for fractional condensation during chondrule formation. *Meteoritics and Planetary Science*, **39**,1931 – 1955.

Krot, A. N., Nagashima, K., Yoshitake, M. and Yurimoto, H. (2010). Oxygen isotopic compositions of chondrules from the metalrich chondrites Isheyevo (CH/CBb), MAC 02675 (CBb) and QUE 94627 (CBb). Geochim. Cosmochim. Acta 74, 2190–2211.

Krot, A.N., Meibom, A., Weisberg, M.K., Keil, K.. (2002). The CR chondrite clan: Implications for early solar system processes. *Meteoritics and Planetary Science*, **37**, 1451–90.

Lada, C. J., Lada, E. A. (2003). Embedded clusters in molecular clouds. *Annual Review of Astronomy and Astrophysics*, **41**, 57—115.

Lauretta D. S., Buseck P. R., and Zega T. J. (2001). Opaque minerals in the matrix of the Bishunpur (LL3.1) chondrite: Constraints on the chondrule formation environment. *Geochimica et Cosmochimica Acta*, **65**, 1337–1353.

Lauretta D. S., Kremser D. T., and Fegley B., Jr. (1996). The rate of iron sulfide formation in the solar nebula. *Icarus*, **22**, 288–315.

Lin, Y., El Goresy, A. (2002). A comparative study of opaque phases in Qingzhen (EH3) and MacAlpine Hills 88136 (EL3): Representatives of EH and EL parent bodies. *Meteoritics and Planetary Science*, **37**, 577 – 599.

Lodders, K., and Fegley, B. (1998). A planetary scientist's companion. New York: Oxford University Press. pp. 84-307.

Lundqvist, F. The crystal structure of daubreelite. *Arkiv for Kemi Mineralogi och Geologi*, **17**, 1- 4.

MacPherson, G. J. (2003). Calcium-aluminum inclusions in chondritic meteorites. In Davis A. M. (Ed.) *Meteorites, Comets, and Planets, Treatise on Geochemistry*, Vol. 1. Oxford: Elsevier-Pergamon, pp. 201 – 206.

Marty, B., Kelley, S., Turner, G. (2010). Chronology and shock history of the Bencubbin meteorite: A nitrogen, noble gas, and Ar-Ar investigation of silicates, metal and fluid inclusions. *Geochimica Cosmochimica Acta*, **74**, 6636 – 6653.

Meibom, A., Desch, S.J., Krot, A.N., Cuzzi, J.N., Petaev, M.I., et al. (2000). Large-scale thermal events in the solar nebula: Evidence from Fe,Ni metal grains in primitive meteorites. *Science*, **288**, 839–841.

Meibom, A., Righter, K., Chabot, N., Dehn, G., Antignano, A., McCoy, T. J., Krot, A. N., Zolensky, M. E., Petaev, M. I., and Keil, K. (2005). Shock melts in QUE 94411, Hammadah al Hamra 237, and Bencubbin: Remains of the missing matrix? *Meteoritics & Planetary Science*, **40**, 1377-1391.

Newsom, H. E. and Drake, M. J. 1979. The origin of metal clasts in the Bencubbin meteoritic breccia. *Geochimica et Cosmochimica Acta*, **43**, 689–707.

Petaev M. I., Meibom A., Krot A. N., Wood, J. A., and Keil, K. (2001). The condensation origin of zoned metal grains in Queen Alexandra Range 94411: Implications for the formation of the Bencubbin-like chondrites. *Meteoritics & Planetary Science*, **36**, 93–106.

Prombo, C. A., and Clayton, R. N. (1978). A striking isotope anomaly in the Bencubbin and Weatherford meteorites. *Science*, **230**, 935-937.

Ramdohr, F., and Epstein, S. (1982). The concentration and isotopic composition of hydrogen, carbon, and nitrogen in carbonaceous meteorites. *Geochimica Cosmochimica Acta*, **46**, 3283 – 3298.

Rubin, A. E., Kallemeyn, G. W., Wasson, J. T., Clayton, R. N., Mayeda, T. K., Grady, M., Verchovsky, A. B., Eugster, O., Lorenzetti, S. (2003). Formation of metal and silicate globules in Gujba: A new Bencubbin-like meteorite fall. *Geochimica Cosmochimica Acta*, **67***(17)*, 3283 – 3298.

Schneider, C.A., Rasband, W.S., Eliceiri, K.W. (2012). NIH image to ImageJ: 25 years of image analysis. *Nature*, Methods **9**, 671-675.

Scott, E. R. D. (1982). Origin of rapidly solidified metal-troilite grains in chondrites and iron meteorites. *Geochimica Cosmochimica Acta,* **45***(5)*, 813-823.

Scott, E. R. D. (2007). Chondrites and the protoplanetary disk. *Annual Review in Earth and Planetary Sciences*, **35**, 577 – 620.

Scott, E. R. D., Krot, A. N. (2003). Chondrites and their components. In Davis A. M. (Ed.) *Meteorites, Comets, and Planets*, *Treatise on Geochemistry,* Vol. 1. Oxford: Elsevier-Pergamon,143–200.

Scott, E. R. D., Krot, A. N. (2005). Chondritic meteorites and the high-temperature nebular origins of their components. *ASP Conference Series,* **341**, 15 – 53.

Shu, F.H., Shang, H., Lee, T. (1996).Toward an astrophysical theory of chondrites. *Science,* **271**, 1545–52.

Sugiura, N. Zashu, S., Weisberg, M. K., and Prinz, M. (1999). H, C, and N isotopic compositions of bencubbinites. *LPSC XXX,* Abst 1329.

Sugiura, N., Zashu, S., Weisberg, M. K. and Prinz, M. (2000) A nitrogen isotope study of bencubbinites. *Meteoritics and Planetary Science*, **35**, 987–996.

Tomkins, A. G. (2009). What metal-troilite textures can tell us about post-impact metamorphism in chondrite meteorites. *Meteoritics and Planetary Science,* **44***(8)*, 1133-1149.

Van Schmus, W. R., Wood J. A. (1967). A chemical-petrologic classification for the chondritic meteorites. *Geochimica Cosmochimica Acta*, **31**, 747-765.

Wai, C. M., and Wasson, J. T. (1977). Nebular condensation of moderately volatile elements and their abundances in ordinary chondrites. *Earth and Planetary Science Letters*, 36, 1-13.

Wasson, J. T. and Kallemeyn, G. W. (1990) Allan Hills 85085: a subchondritic meteorite of mixed nebular and regolithic heritage. *Earth and Planetary Science Letters*, **101**, 148–161.

Weisberg M,. K., Prinz, M., Clayton, R. N., Mayeda, T. K., Grady, M. M., and Pillinger, C. T. (1995). The CR chondrite clan. *Proceedings of the NIPR Symposium on Antarctic Meteorites* 8:11–32.

Weisberg, M. K. and Ebel, D. S. (2009). The Fountain Hills impact-modified CB chondrite and the thermal history of the CB asteroid. *Meteoritics & Planetary Science*, **44**, 201–210.

Weisberg, M. K., Boesenberg, J. S., and Ebel, D. S. (2002). Gujba and origin of the Bencubbinite-like (CB) chondrites. LPSC XXXIII, Abst. #1551.

Weisberg, M. K., Connolly, H.C. Jr, Ebel, D.S. (2004). Petrology and origin of amoeboid olivine aggregates in CR chondrites. *Meteoritics and Planetary Science*, **39**, 1741–1753.

Weisberg, M. K., Kimura, M. (2010). Petrology and Raman spectroscopy of high pressure phases in the Gujba CB chondrite and the shock history of the CB parent body. *Meteoritics and Planetary Science*, **45***(5)*, 873 – 884.

Weisberg, M. K., McCoy, T. J., Krot, A. N. (2006). Systematics and evaluation of meteorite classification. In Lauretta DS, McSween HY Jr. (Eds). *Meteorites and the Early Solar System II*. Tucson: The University of Arizona Press, pp. 19-52.

Weisberg, M. K., Prinz, M., and Nehru, C. E. 1990. The Bencubbin chondrite breccia and its relationship to CR chondrites and the ALH 85085 chondrite. *Meteoritics*, **25**, 269–279.

Weisberg, M. K., Prinz, M., Campbell, A. J., (2000). Origin of metal in the CB (Bencubbin) chondrites. *LPSC XXI,* Abst #1466.

Weisberg, M. K., Prinz, M., Clayton, R. N., and Mayeda, T. K. (1993). The CR (Renazzo-type) carbonaceous chondrite group and its implications. *Geochimica et Cosmochimica Acta*, **57**, 1567–1586.

Weisberg, M. K., Prinz, M., Clayton, R. N., Mayeda, T. K., Sugiura, N., Zashu, S., Ebihara, M. (2001). A new metal-rich chondrite grouplet. *Meteoritics and Planetary Science*, **36**, 401 – 418.

Yao, J. H., Elder, K. R., Guo, H., and Grant, M. (1993). Theory and simulation of Ostwald ripening. *Physical Review B,* **47***(21)*, 110-125.

Zanda, B., Bourot-Denise, M., Perron, C., and Hewins, R. H. 1994. Origin and metamorphic redistribution of silicon, chromium, and phosphorus in the metal of chondrites. *Science,* **265**, 1846–1849.